REDUCED-COMPLEXITY MODELS (RCMs) FOR RIVER DELTA FORMATION WITH CHANNEL DYNAMICS

A DISSERTATION
SUBMITTED TO THE FACULTY OF
UNIVERSITY OF MINNESOTA
BY

MAN LIANG

IN PARTIAL FULFILLMENT OF THE REQUIREMENTS
FOR THE DEGREE OF
DOCTOR OF PHILOSOPHY

VAUGHAN R. VOLLER, CHRIS PAOLA

JUNE 2013

Acknowledgements

I would like to thank my advisers, Vaughan Voller and Chris Paola, for introducing me to the world of reduced complexity modeling in geomorphology, for your encouragement and guidance, and for all the support in this six-year of the PhD journey. I learned so much.

I would like to thank my committee members, Mihai Marasteanu and Michele Guala, and my oral prelim exam committee members, Efi Foufoula-Georgiou and Kimberly Hill, for your support and advises.

National Center for Earth-surface Dynamics (NCED) provided the majority of funding during my PhD research. I have also received support from the Science Museum of Minnesota, ExxonMobil Upstream Research Company, and the Wax Lake Delta research group on the FESD project at University of Texas at Austin.

I would like to thank my colleagues for all the inspiring discussion and collaboration, especially Doug Edmonds and my post-doctoral supervisor Paola Passalacqua with her research group.

I had a great time working at Saint Anthony Falls Lab (SAFL). Thank you, everyone. It's a very unique experience to work in an interdisciplinary place like this.

I would also like to thank my friends. I'm so lucky to have you guys. We had so much fun together, and, your support helped me to go through the difficult times in my life.

Last but not least, thank you, mom and dad. You are the ultimate source of love and strength in my heart. I hope you will be proud of me.

Dedication

This dissertation is dedicated to my family, and also to the explorers in the field of science and technology.

Abstract

River deltas are among the most populated, productive yet vulnerable regions in the world. They are complex systems that involve processes over a wide range of time and space scales. In this situation detailed modeling of every aspect of the system can be extremely expensive which, due to the resulting complexity, may only lead to limited physical insights. The alternative is to develop Reduced-Complexity Models (RCMs) that attempt to retain the key dynamics and phenomena in delta morphodynamics through employing approximate but physically reliable descriptions of the governing transport equations. In this collection of work we develop a series of rule-based cellular models based on a "weighted-random-walk" framework, arriving at a comprehensive delta formation model with the ability to resolve topography, a full range of channel network dynamics and stratigraphy. We also describe three exploratory models that could potentially serve as components for new delta formation RCMs.

Table of Contents

List of Tables

List of Figures

CHAPTER 1

INTRODUCTION

1.1. Overview

Home to hundreds of millions of people, major coastal cities and infrastructure, immensely productive wetlands, and some of the most compelling and diverse landscapes on Earth – yet low-lying and vulnerable to storms and rising sea levels – deltas are emerging as among the most critical environments in a changing world. They are also immensely complex. The science of deltas comprises, in roughly equal parts, geomorphology, ecology, hydrology, organic and microbial geochemistry, and human dynamics. The physical dynamics alone would present a formidable challenge if they were restricted to just turbulent flow interacting with coarse-grained loose sediment (gravel and sand); but most natural deltas involve major additional complications such as fine-grained cohesive sediment (mud) and strong, two-way interactions with biota.

A fundamental debate is developing across the sciences as to the best way to model and understand such complexity (e.g., Murray 2003; Overeem et al., 2005; Paola and Leeder, 2011; Hajek and Wolinsky, 2012). Should we try to capture everything, creating models that simulate the processes in as much detail as current knowledge and computing power allow; or should we simplify, even at the risk of losing connection with reality? Modeling of deltas in recent years has produced excellent examples of both approaches, which we review in Chapter 4. In this collection of work, we present a range of models that reside in the middle ground between detailed simulation and abstract simplification, which we will refer to as "**Reduced-Complexity Models (RCMs)**". RCMs are usually compared to reductionist models or so-called "high-fidelity" models that aim at, in the case of delta modeling, rigorously solving the governing equations of fluid flow and sediment transport. On the contrary, RCMs take intuitive yet quantitative approaches with a goal to abstract processes so as to get the maximum return in emergent system-scale behavior for the minimum investment in computational complexity (Paola et al., 2011). We believe

that the availability of abundant computing power strengthens rather than weakens the case for so-called reduced-complexity models such as the ones we propose in this collection of modeling work. Understanding – as opposed to simulating – complex natural phenomena requires a spectrum of approaches and a clear understanding of the advantages and disadvantages of each.

The main goal of our RCM modeling work is to **resolve delta formation at the scale of channel network dynamics**. Channels are essential for predicting the detailed evolution of the delta surface and its ecosystems (Paola et al. 2011). Through a distributary network of channels, sediment is delivered to the shoreline to build the delta forward (progradation), and through the interaction between channels and the floodplain, sediment is delivered to the entire delta surface to build the delta upward (aggradation). Understanding what controls the dynamics of this network and what role it plays in the entire architecture of the deltaic depositional system is not only an interesting scientific topic but also critical for engineering and ecological purposes such as navigation, agriculture, fishery, habitat restoration, flooding risk analysis, etc. We propose that, a channel-resolving delta model should be able to produce one or more of the self-emergent features from the list below:

- **Channel elongation**: a channel extends into the ocean by building up levees on both sides and the length of the channel grows (e.g., Seybold et al., 2009).

  A field example of channel elongation is the Mississippi "bird's foot" Delta (Figure 1-1).
- **Channel bifurcation**: a channel splits into two smaller channels (or more than two channels in some cases), which is usually the result of flow splitting around mouth bar deposition (e.g., Edmonds & Slingerland, 2007). Repeated bifurcations at different orders produce a "tree-like" distributary network.

  A few field examples of channel bifurcation are the Wax Lake Delta in the US and the Mossy Delta in Canada (Figure 1-2).

- **Channel avulsion**: flow escapes from an existing course and follows a new course. This new course could be an abandoned channel or a newly created channel by erosion (e.g., Jerolmack & Paola, 2007; Reitz et al., 2010).

  A field example of channel avulsion is the Yellow River in China (Figure 1-3).
- **Delta lobe-switching**: by channel bifurcation and avulsion, a delta distributes sediment evenly to all directions to form a semi-circular shape by building and switching between individual lobate complexes of deposition (Frazier 1967).

  A field example of delta lobe switching is the Mississippi River Delta system (Figure 1-4).
- **Channel and floodplain co-evolution**: channels on a delta are not isolated from the surrounding delta surface. For example, the rate of in-channel deposition and floodplain deposition is closely related to channel avulsions (Jerolmack & Paola, 2007). Also, floodplain, especially islands, are the primary region of wetlands and their response to channel dynamics are critical for ecological purposes (Twilley et al., 2007).
- **Channel lateral migration, braiding and meandering**: although these processes are less essential for deltaic environments than for fluvial environments, they represent fundamental hydraulic and sedimentary processes that control the lateral movement of channels (Wickert et al., 2013).

A brief review of channel-resolving delta models can be found in Paola et al. 2011, comparing detailed ("high-fidelity") models represented by Delft3D (Edmonds & Slingerland, 2010; Geleynse et al. 2010) and reduced-complexity models represented by Seybold et al. (2007, 2009). While Delft3D produces more realistic-looking distributary channel networks, its computational cost is still high. In this research, we explore the possibility of building a delta formation model that resolves the channel processes listed above but has a flexible rule-based structure of reduce-complexity models.

Figure 1-1. A satellite image of the modern Mississippi River Delta - the "Bird's Foot" delta which extends hundreds of kilometers into the ocean.

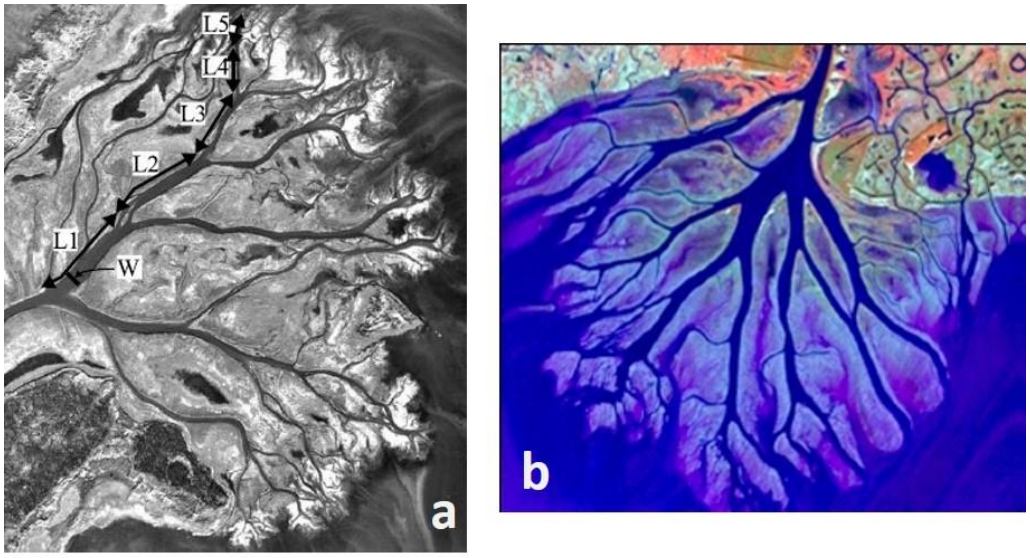

Figure 1-2. (a) An aerial photography of Mossy delta, Saskatchewan, Canada (Information Service Corporation, 1982) labeled by Edmonds and Slingerland, 2007, showing that the bifurcation length (L) and width (W) decrease with each successive bifurcation of the main channel (Edmonds & Slingerland, 2007). (b) An aerial photo of Wax Lake Delta, Louisiana, USA (photo source: National Center for Earth Surface Dynamics).

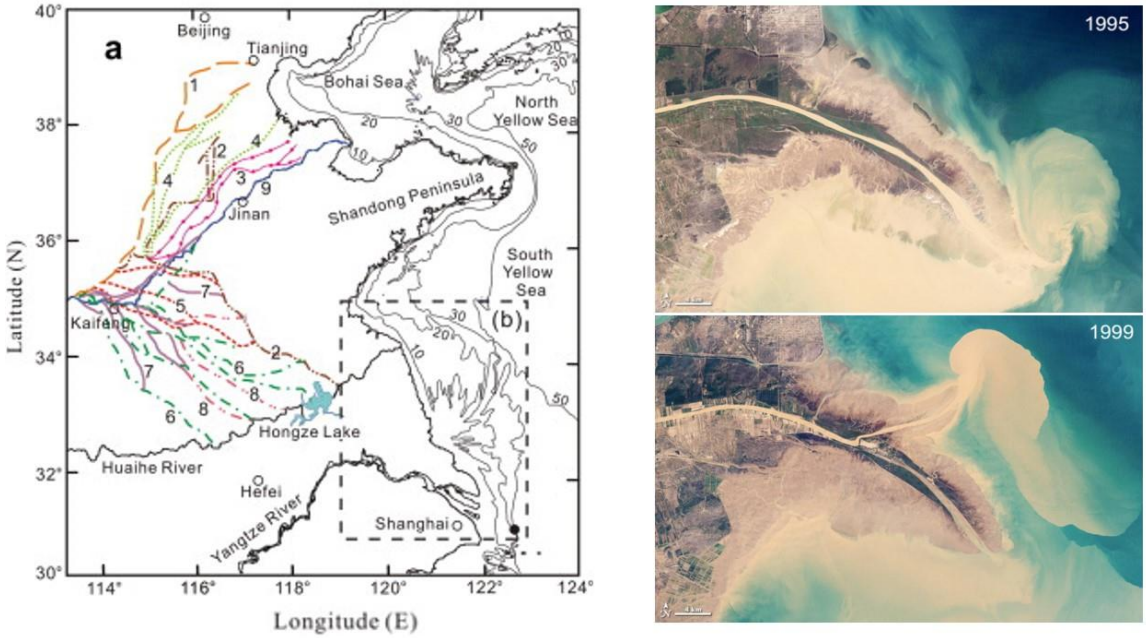

Figure 1-3. (left) changes in the lower course of the Yellow River since 300 BC and shoreline variations in the coastal zone from the Old Yellow River mouth to north of the Yangtze River mouth during AD 1128-2002 (Liu et al., 2010); (right) Yellow River avulsion (engineered) close to the river mouth between year 1995 and 1999 (image source: NASA Earth Observatory).

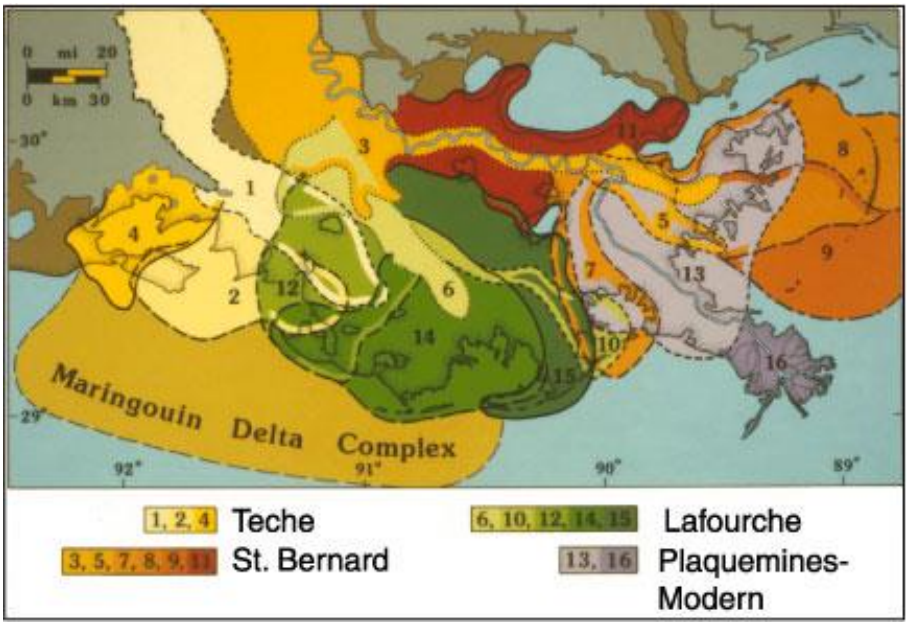

Figure 1-4. Delta Complexes (historic lobes) of Mississippi River Deltaic Plain (Frazier, 1967)

1.2. Dissertation outline

The main body of the dissertation consists of two groups of model types. The first group of models (Chapter 2, Chapter 3 and Chapter 4) are a step-by-step evolution towards a "weighted-random-walk" delta formation model based on a hybrid of simplified physical governing equations and phenomenological rules describing water and sediment transport. The second group (Chapter 5 and Chapter 6) are a collections of exploratory models aiming at innovative building blocks for a full delta formation model and their theoretical basis.

<u>Evolution towards a "weighted-random-walk" delta formation model</u>

In **Chapter 2**, we introduce the idea and basic framework of the "weighted-random-walk" by constructing a plan-form cellular delta formation model. The construction starts with a trivial delta filling model on a lattice grid with parcels representing mass doing a pure random walk. Then we add model complexity by using two types of parcels to

distinguish channel and land. The walking probabilities in different directions are not evenly distributed as in a pure random walk, but are determined by rules taking into account the difference between channel and land – a "weighted" random walk. We show how this simple framework is able to produce reasonable-looking delta and channel network patterns, and more importantly, how it could serve as a platform for future improvements.

In **Chapter 3**, we build on the weighted-random-walk method developed in Chapter 2 by adding two critical pieces to the rules determining the routing weights of the random walk: the first is the concept of a "routing direction" that takes into account physical attributes of the system such as topographical slope and flow inertia, and the second is phenomenological rules for sediment deposition and erosion based on a cellular discharge field calculated from the collective movements of parcels. With these ingredients, we show the model is able to grow plan-form meandering rivers. This modified weighted-random-walk method is the core of the next-level quasi-3D model in Chapter 4.

In **Chapter 4**, we move from a plan-view model to a quasi-3D delta formation model that resolves topography and depth-averaged flow field. The core of this model is still the weighted random walk method developed in Chapter 2 and Chapter 3, but with more details accounting for: (i) a better representation of the mass and momentum balance of fluid motion, (ii) a more physical scheme for sediment deposition and erosion based on resolved flow field. In the results we show (i) different deltas produced with mixtures of coarse and fine grains at different portion ratio, (ii) simulated laboratory fan deltas, (iii) delta behaviors responding to different basin geometry, and (iv) recorded stratigraphy by grain size distribution (sand fraction) and by deposition age distribution. In the end we point out the strength and weakness of the model and direction of future work along this line.

<u>Exploratory models</u>

In **Chapter 5**, we collect some exploratory models from our modeling exploration. These models didn't grow into a full delta formation model but have their own merits in being potential building blocks of future delta formation models. We give a brief description of the key ideas, construction and representative results of three models: (i) an analogical model utilizing the similarity between distributary channel network of river deltas and dendrite crystal growth in undercooled melts (detailed physical and numerical background provided in Chapter 6), (ii) a reduced hydrodynamic solver based on the diffusive-wave form of the shallow water equations under a low-Froude-number flow condition, and its application to flow over a Gaussian-shaped bump mimicking a mouth bar, and (3) a unit-discharge cellular routing scheme aiming at building a mouth bar at the front of a jet flow. In the end we summarize what to be learned from these exploratory models and how they can guide future model development.

In **Chapter 6**, we present a published paper by Liang and Voller (2011), providing detailed description of the physical setup and numerical modeling method of dendrite crystal growth in undercooled melt, which serves as a theoretical base for the analogical model in Chapter 5.

CHAPTER 2

PRELIMINARY DEVELOPMENT IN PARCEL-BASED WEIGHTED RANDOM WALK MODELS FOR DELTA FORMATION

2.1. Introduction

The objective of this chapter is to construct Reduced-Complexity Models (RCMs) for modeling the planforms of deltas and their channel networks with the least set of rules or model constrains. In the first instance we will construct a simple mass balance model that creates a semi-circular planform. Then we will explore ways in which channel networks and kinematics can be accounted for. The models will act in a rectangular domain covered by a lattice of square cells. The core ingredients in the model are the rules that determine the routing of entities (referred to as "parcels") from cell to cell. In these first level models the movement rules take the form of a "weighted random walk", by which we mean a random walk with weighted probabilities in different walking directions. We will show how this simple framework is able to produce reasonable planform deltas with channel networks. In the end we point out the strength and weakness in this simple construction to build a platform for future improvements.

2.2. The concept of "weighted random walk"

To define the concept of weighted random walk, consider a parcel at the center of 8 neighboring cells (*nb* = 1 to 8) (Figure 2-1) on a lattice grid of square cells.

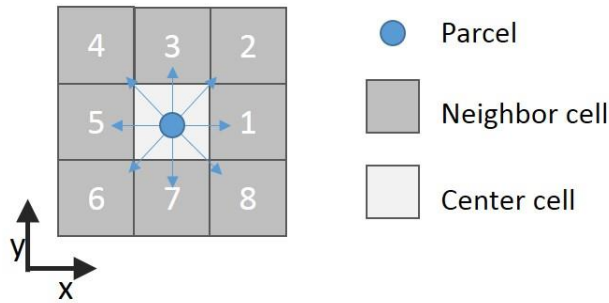

Figure 2-1. A parcel located in the center cell has the option of traveling to eight possible neighboring cells.

In a weighted random walk approach, the routing probability that this parcel moves to a particular neighbor cell $nb = i$ is then given by

$$p_i = \frac{w_i}{\sum_{nb=1}^{8} w_{nb}}, \quad i = 1, 2, \ldots, 8 \tag{2.1}$$

where $w_{nb} \geq 0$ are routing weights. Note that the values of the weights will be assigned by the RCM rules, which are usually derived from the physical conditions of the system. In general the sum of weights $\sum_{nb=1}^{8} w_{nb}$ need not to be unity but through the definition in equation (2.1) the sum of the routing probabilities always will be unity.

Once the routing probabilities are determined, the step movement of the parcel can be calculated by a stochastic process that a random number χ (between 0 and 1) is generated and depending on which accumulated probability interval χ falls into, one cell will be chosen from the eight neighboring cells as the next position of the parcel. Figure 2-2 shows an example of this calculation.

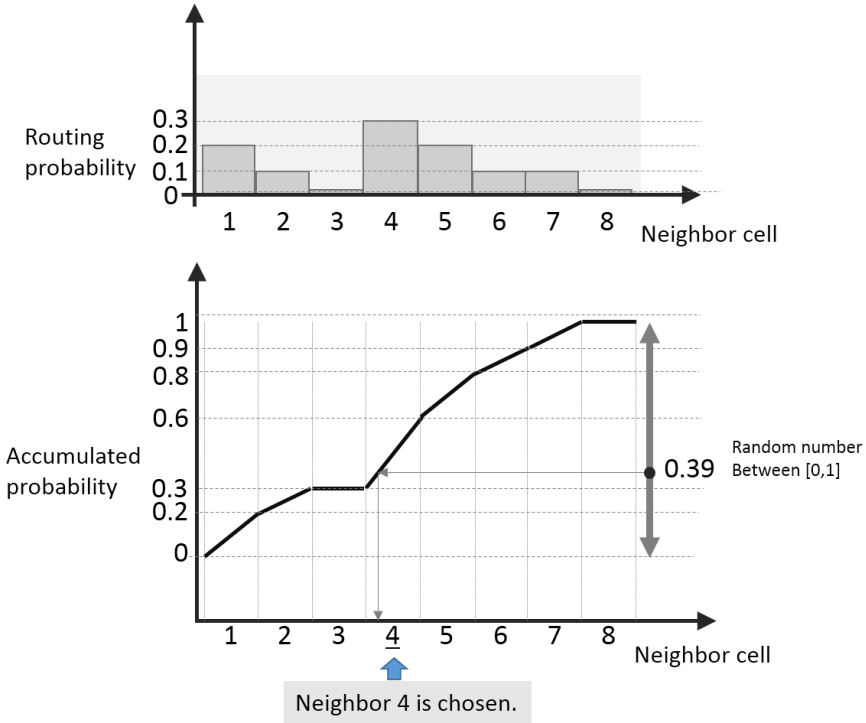

Figure 2-2. An illustration showing a sample stochastic calculation of choosing a parcel step based on the routing probabilities and a generated random number between 0 and 1 (0.39 in this example).

2.3. Single-parcel binary delta filling model

We start our exploration of parcel-based weighted random walk models by constructing a simple basin filling model where the domain is covered with a lattice grid of square cells which can have binary states : 1 – land, and 0 – ocean. The initial condition is a grid of 'ocean' cells only. Sediment input is imposed at a fixed inlet cell on one of the domain boundaries. The input is in the form of "sediment parcels" which travel through the domain looking for a place to settle – to build land in the ocean. These parcels enter the domain one by one. Each parcel moves on the grid in a random-walk fashion according to two rules:

1) On each step of the random walk, a parcel moves from one cell to one of the eight neighbors. In this model all eight neighbors have the same weights so via equation (2.1) the routing weights (and probabilities) are all equal:

$$w_1 = w_2 = ... = w_8 = 1$$
$$p_1 = p_2 = ... = p_8 = \frac{1}{8} \tag{2.2}$$

2) Whenever a parcel arrives at an 'ocean' cell, its random walk stops there and the 'ocean' cell is turned into a 'land' cell.

This simple random walk model, which is similar in spirit to the Monte-Carlo scheme previously used to model the polymer filling of complex mold geometries (Voller 2004), results in a semi-circle land growth pattern which resembles the expected planform shape of a delta (Figure 2-3), and the average shoreline radius grows proportionally to the square root of time.

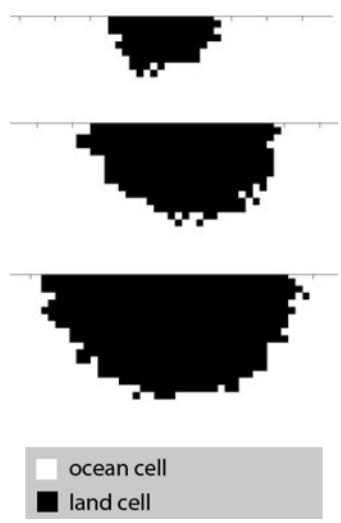

Figure 2-3. A delta formed by the single-parcel filling model. From top to bottom are three snap shots at different calculation steps of one model run.

2.4 Dual-parcel delta formation model with channel patterns

We can significantly add to the utility of the almost trivial single-parcel binary model by developing a random walk process that can distinguish between channel and floodplain in the planform, a step towards building a realistic distributary network. The key is to introduce, at the inlet, two types of parcels: 'sediment parcel' and 'water parcel'. Both parcels can be deposited in a given ocean state cell, the sediment parcels forming land (floodplain) and the water particles forming channels. Accordingly, cells in this model have three states: '0 - ocean', '1 - channel' and '2 - floodplain'. Parcels are routed in the same "weighted random-walk" fashion used in the single-parcel model. However, we add a few constrains to mimic the different transport properties of sediment and water. Detailed rules are as follows:

1) A calculation step of the model is defined by the consecutive release of a number (N_w) of water parcels followed by the consecutive release of a number (N_s) of sediment parcels. In a calculation step the ratio of sediment parcels to water parcels is a model parameter, $\mu = N_w / N_s$;

2) Water parcels cannot move through 'floodplain' cells, i.e., when routing water parcels, the routing weights and thereby the routing probabilities of 'floodplain' cells are equal to zero;

3) Sediment parcels can move through both 'channel' and 'floodplain' cells, but, with a smaller probability to choose 'floodplain' cells. This is to mimic the physical process that sediment fluxes generally follow channels only escaping to deposit onto the floodplain during flooding events. This rule is imposed by selection of the routing weights in equation (2.1) as

$$w_{nb} = \gamma, \quad \text{if neighbor cell is 'floodplain'},$$

$$w_{nb} = 1, \quad \text{if neighbor cell is 'channel'};$$

where γ is a model parameter referred to as the probability contrast between floodplain and channel cells. Typically γ is much less than 1, e.g. $\gamma = 0.2$.

4) When a water parcel arrives at an 'ocean' cell, its random walk stops there, and the 'ocean' cell is turned into a 'channel' cell;

5) When a sediment parcel arrives at an ‘ocean’ cell, its random walk stops there, and the ‘ocean’ cell is turned into a ‘floodplain’ cell.

All the runs start with a small delta that has a radius of 5 floodplain cells and a straight channel in the center that is 3 cells wide (Figure 2-4).

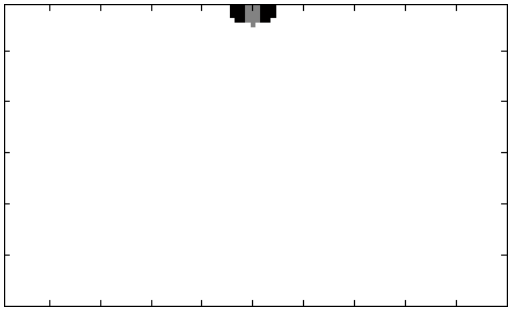

Figure 2-4. Domain and initial conditions of the dual-parcel delta model. In the upper center is the small delta with a channel as a start.

In Figure 2-5 we show planforms predicted by the model after 500 calculation steps, with six combinations of parameter values, the ratio of sediment parcels to water parcels (μ) and the probability contrast for sediment movement between floodplain and channels cells (γ). From these results we first note that this simple dual-parcel random walk method has the ability to produce a dendritic network of channels, with a fundamental resemblance with natural deltaic systems (Figure 2-5). This network is created by the fact that sediment parcels deposited at channel mouth force channels to bifurcate and sediment parcels deposited along channel sides help channels to elongate. An important emergent feature is lobe extension associated with channel elongation. The shoreline advances faster around active channels mouths, due to the higher probability of receiving sediment parcels from the channel, compared to the relatively smaller amount of sediment parcels transported through the floodplain. We also note that by varying controlling parameters, μ and γ, i.e. the ratio of sediment parcels to water parcels, and the probability contrast between floodplain cells and channel cells, different channel network patterns can be obtained. Although the physical meaning of these two

parameters are still highly abstract, here we give an interpretation of how they might be related to natural processes:

A higher value of μ gives a higher ratio of sediment parcels to water parcels, therefore channels are more sparse (see the transition from the bottom row to the top) as a result of 1) sediment parcels occupy the majority of delta surface and, 2) channels are more likely to be "choked" by the excessive deposit at the mouth.

A higher value of γ gives a higher "flooding rate", i.e. sediment parcels are more likely to escape from channels, and delta grows more evenly in all radial directions (see the comparison between the left and right column in Figure 2-5). With $\gamma = 0.5$, channel and floodplain cells have equal weights and the resultant delta has a semi-circle shape, while with $\gamma = 0.05$, the weights of floodplain cells are one magnitude smaller than the ones of channel cells, and delta grows much faster along channels and form very distinct lobes. The effect is even stronger with fewer channels (a smaller value of μ).

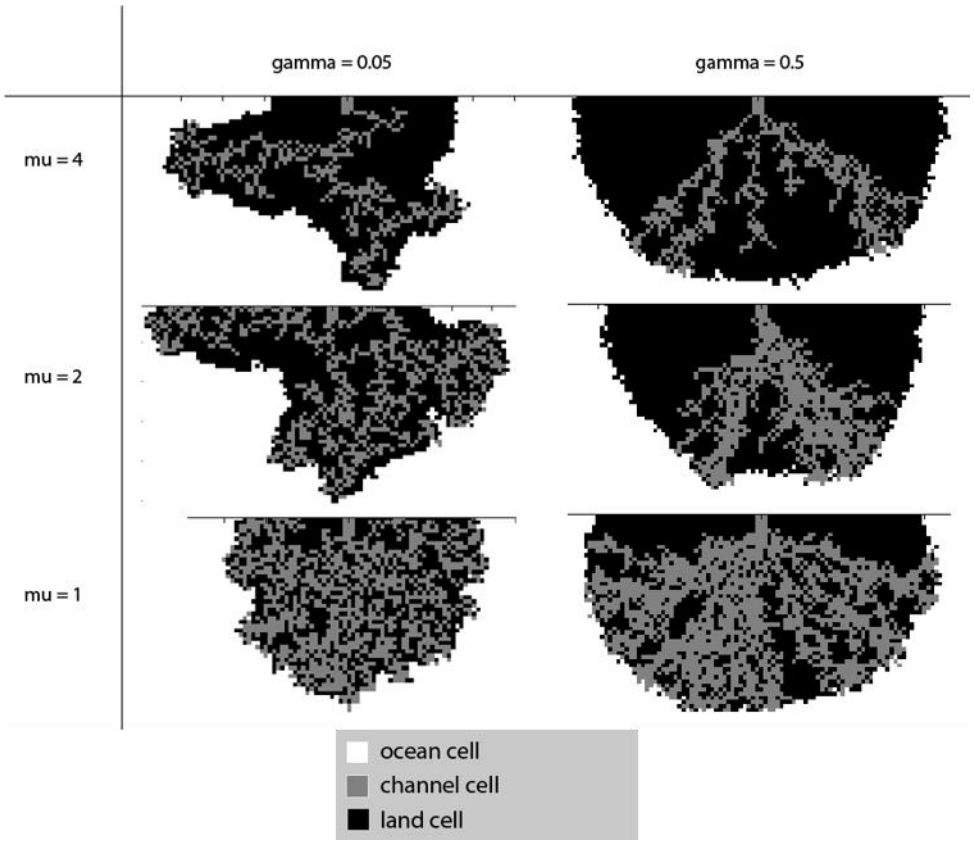

Figure 2-5. Sample results from the dual-parcel delta model. Different delta shapes and channel network patterns are produced from six combinations of μ and γ values.

Despite the relative success of the simple dual-parcel calculation we do note, an important unrealistic feature that, channels "choked" by excessive sediment deposition at the mouth become abandoned and form dead-ends dis-connected from the ocean. To our knowledge such features are not commonly observed in natural systems. In the following we make a few modifications to correct this. This correction is based on identifying the "dead-end channels" and then following the natural process, allowing them to become filled in with sediment. The device for identifying dead-ends is via a "pseudo flow field". Once identified the dead-end channel cells are converted to floodplain cells. To better conserve mass, instead of converting them right after being identified, the cells are at a "standby" state waiting for sediment parcels to occupy them. These "standby" cells are labeled with the additional state named "abandoned channel" cell.

In detail, if we assume that each parcel has a unit mass, each parcel step forms a unit vector with a specified direction. In the most general case where all eight neighbors can be accessed these vectors are:

$$(1,0),\left(\tfrac{1}{\sqrt{2}},\tfrac{1}{\sqrt{2}}\right),(0,1),\left(-\tfrac{1}{\sqrt{2}},\tfrac{1}{\sqrt{2}}\right),(-1,0),\left(-\tfrac{1}{\sqrt{2}},-\tfrac{1}{\sqrt{2}}\right),(0,-1),\left(\tfrac{1}{\sqrt{2}},-\tfrac{1}{\sqrt{2}}\right).$$

We will refer to these vectors as "step vectors". A measure of the contribution to the discharge magnitude of a given parcel visiting a given cell can be determined by averaging the input and output step vectors. In this way, the resulting average vectors can have a number of possible directions and magnitudes anywhere from zero (in the case where the input and output is from and too the same neighboring cell) to unity; examples of the construction of these average vectors for three visiting parcels is shown in Figure 2-6. Following the calculation step, the average vectors associated for all visiting parcels to a cell can be summed to form a pseudo discharge vector. Note in the vicinity of dead end-channel locations, since parcels are continuously reversing direction, we would expect the summed pseudo discharge vector to have a close to zero magnitude, even though the magnitudes of its contributors are all non-zero.

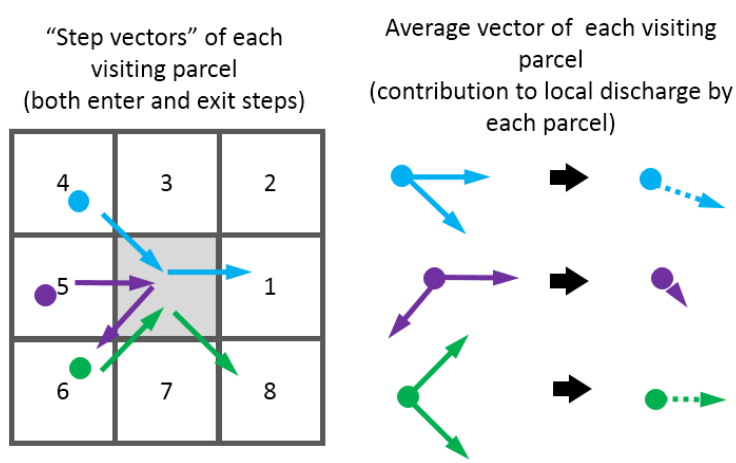

Figure 2-6. Illustration of the step vectors of individual visiting parcels and the averaged vectors the contribution to the local discharge by each visiting parcel.

To keep track of the development of the pseudo discharge we first normalize by the magnitude of the total inlet discharge and then form a moving average over a number

(typically 30) of model calculation steps. An example snap shot of this vector field is shown in Figure 2-7.

As noted with this construction it is to be expected that channel cells in the vicinity of a dead end will have pseudo discharge vectors of small magnitude. Hence, a simple threshold value on the magnitude of the pseudo discharge vector in each cell can be used to determine when a channel cell needs to be erased, typical values for this critical pseudo discharge Q_c are in the range of $0.01 < Q_c < 0.1$, i.e., one or two order of magnitude below the inlet discharge. If at the end of a calculation step a channel cell fails this criterion it is relabeled as an "abandoned channel"

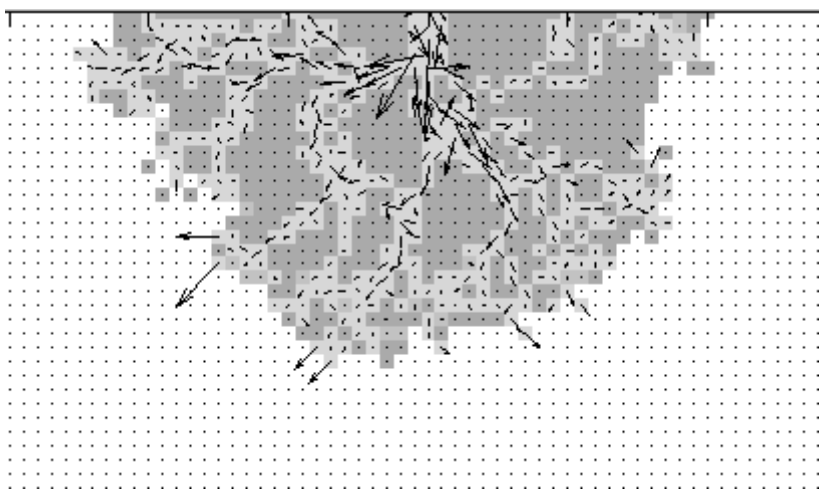

Figure 2-7. A sample pseudo flow field. Note the magnitude distribution of the vectors. The weak channels are potentially to be abandoned soon.

In subsequent calculation steps when a sediment parcel arrives at an 'abandoned channel' cell, its random walk stops there, and the 'abandoned channel' cell is turned into a 'floodplain' cell.

In Figure 2-8, we show the effects of choosing different values of the critical pseudo discharge, Q_c, with two sets of results. Naturally with a higher critical value channels are abandoned more frequently so that the number of active branches reduces quickly as

delta grows bigger and channel network grows into more orders of bifurcation (left column of Figure 2-8).

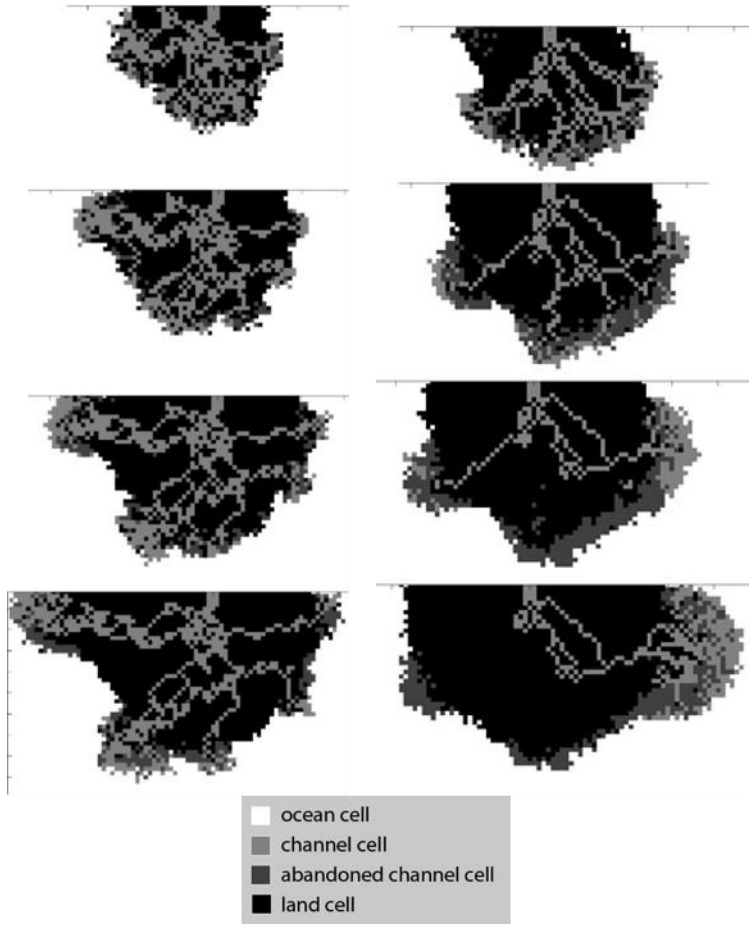

Figure 2-8. Sample results produced by the dual-parcel delta model with channel patterns. The left column has the critical pseudo discharge $Q_c = 0.05$. The right column has the critical pseudo discharge $Q_c = 0.033$. Both runs have the same values of the ratio of water/sediment parcels, $\mu = 1$, and floodplain/channel probability contrast, $\gamma = 0.2$.

Comparing Figure 2-8 with Figure 2-5, we can see that after adding the erasing process, the dendritic channel network looks more realistic. However, channel network doesn't exhibit strong characteristics of self-similarity as higher order bifurcations are not stable and disappear rapidly. The reason is, as channels split into more and more branches, the

successful rate of each branch to receive a stable supply of water parcels to remain above the critical pseudo discharge decreases. Therefore, it is 'unfair' to give the same critical pseudo discharge value for all orders of bifurcation. Theoretically, as the branches get smaller, they can be at a stable equilibrium state with much less flow discharge compared to main trunks as they are shallower, narrower, and have less sediment flux to transport (Edmonds and Slingerland, 2007). In light of this, we modify the parameter Q_c to take into account the order of bifurcation. To start simple, we make this value as a function of radius:

$$Q_c(R) = Q_{c0} \frac{R_0 - R}{R_0} \tag{2.3}$$

R_0 is a reference radius, currently set to 50 cells, which is the maximum size of the modeled delta;

R is the radius of any given cell in the domain;

Q_{c0} is a reference critical pseudo discharge, typically 0.01~0.1.

In Figure 2-9 we show the results from two sample runs with different values of reference critical flow rate, Q_{c0}. Compared to Figure 2-8, bifurcations are stable at different orders. Other than this, the response of the number of active channels to changes in the reference critical pseudo discharge is essentially the same as Figure 2-8.

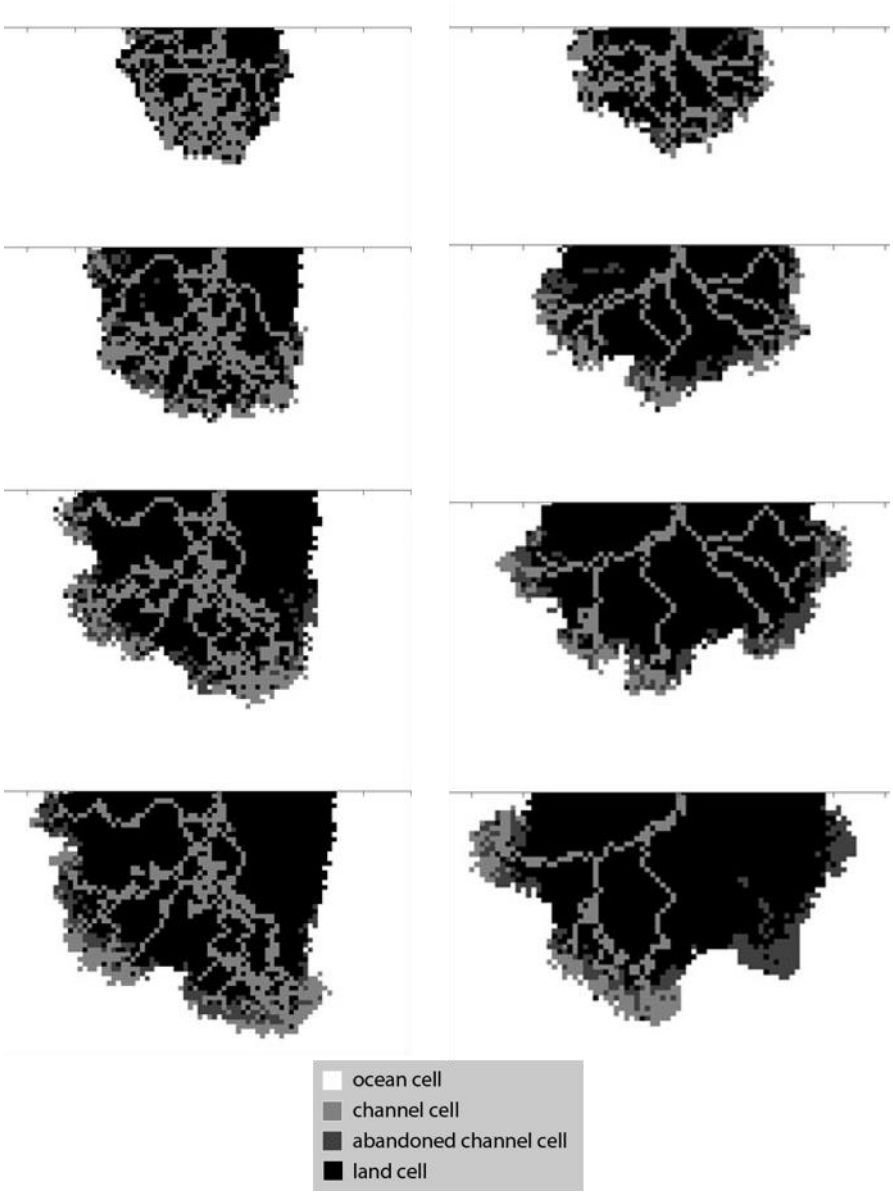

Figure 2-9. Sample results produced by the due-parcel delta model with critical pseudo discharge Q_c as a function of radius R. Left column, reference value $Q_{c0} = 0.1$; right column, reference value $Q_{c0} = 0.05$. Both runs have reference radius $R_0 = 50$, $\mu = 1$ and $\gamma = 0.2$.

2.5 Discussion

So in summary the planform RCM is able to provide a reasonable description of a delta growth. In particular, as noted above, it is able to capture key channel kinematics such as

bifurcation and lobe abandonment. The model, however, is not able to predict other key channel kinematics such as reoccupation and migration. Two potential weaknesses, which might account for this inability is that in the current RCM (1) the direction of a parcel random walk is essentially arbitrary and (2) the sediment parcel behavior does not include any facility to account for realistic sediment transport behaviors such as deposition and erosion.

We suggest that there will be significant benefit to the ability of our model if devices can be constructed that overcome these deficiencies. Toward this end in the next chapter we build further on the concept of a weighted random walk to allow for the tuning of a preferred parcel routing direction. Following in chapter 4 we couple with additional sediment parcel transport rules to dramatically extend our delta RCM to a point where it can realistically capture topography evolution and a complete description of critical channel kinematics.

CHAPTER 3

A WEIGHTED RANDOM WALK MODEL FOR PLANFORM MEANDERING RIVERS

3.1. Introduction

In Chapter 2, we showed how a simple parcel-based weighted random walk model can produce complex channel patterns in the formation of planform river deltas. Here we expand and modify these ideas in an attempt to build an RCM for modeling plan-form meander migration. Our expectation is that the lessons and techniques learned in this endeavor will provide critical information for the construction of more realistic RCMs of deltaic channel processes.

3.2 Model

<u>Initial and boundary conditions</u>

We look at a section of the plan-form of a fluvial channel and its surrounding floodplain. This reach of channel is supposed to be at equilibrium state, meaning that the channel has normal flow condition and there isn't any net deposition or erosion. The model domain is a rectangular lattice grid of 80 by 200 square cells. Cells have binary states: 0 – channel, 1 – land. Initially there is a straight channel in the center of the domain from the left to the right (Figure 3-1), with a fixed discharge Q_{in} and width W =5-10 cells. Inlet cells are located on the left boundary.

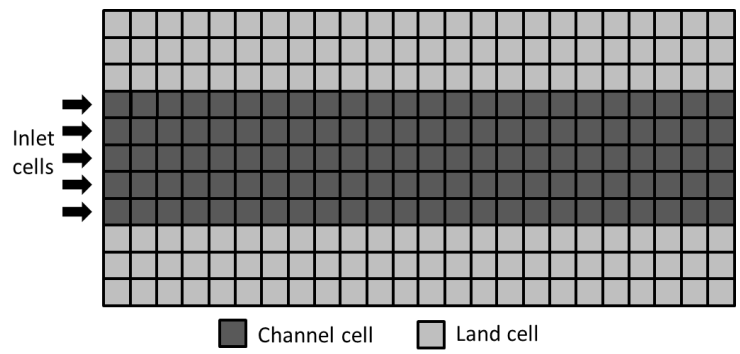

Figure 3-1. Illustration of the domain and initial cell-type arrangement (not plotting the whole domain)

Unlike our previous model that used two parcel types (water and sediment) here we route water parcels alone. In each calculation step we successively introduce N_p water parcels and route through the cells until they reach the exiting boundary on the right side of the domain. A given parcel is introduced to the domain by randomly coming into one of the W inlet cells. Further each water parcel is assumed to carry a discharge of value

$$Q_p = \frac{Q_{in}}{N_p}. \tag{3.1}$$

In this way, in a calculation step, each input cell receives on average a discharge of

$$Q_0 = Q_{in}/W, \tag{3.2}$$

a value that will be used as a "reference cell discharge".

The routing of the water parcels is via the weighted random walk process introduced in Chapter 2, where a set of routing weights and associated parcel routing probabilities are calculated for each cell. Here the key difference is to construct the weights in such a way to impose a preferred direction of travel. To demonstrate the operation of this model we build it in an incremental fashion, adding new and modified rules at each step.

<u>Basic routing: parcel random walk in a fixed downstream direction</u>

In a channel where a fixed downstream direction is specified, the first and most basic realization of the model is to assign the routing weights evenly among the immediate downstream channel neighbors (as shown in Figure 3-2). This results in a probability field that trivially directs the water parcels down the channel. At the end of each calculation step (the release and tracking of N_p water parcels), the nature of this flow is captured by calculating a "cell discharge vector field". Similar to the previous chapter our starting point is to construct, for each visiting parcel, an average vector of the input and output vectors, see Figure 2-6. So the result is, for each channel cell, a set (size N_{visit}) of vectors each expressing the average path of a visiting parcel through that cell. A summation of this set of vectors provides, after appropriate normalization, a representative direction for water parcels through the cell. In this way, a vector with this direction and a magnitude

$$Q_{cell} = N_{visit} Q_p \,. \tag{3.3}$$

Q_{cell} can be regarded as a discharge vector for the cell, which we will refer to as the "cell discharge vector" (see Figure 3-3).

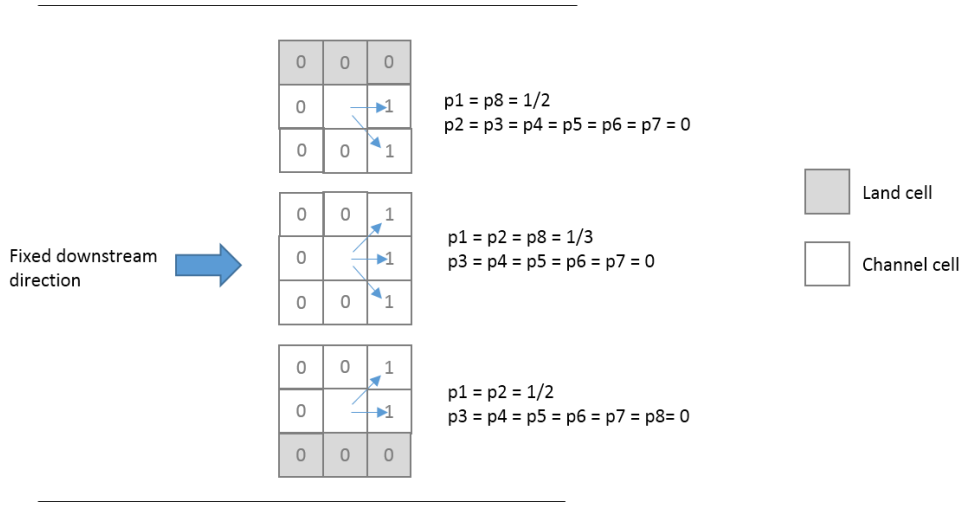

Figure 3-2. Basic routing scheme: random walk in a fixed downstream direction. Weights are evenly distributed among immediate downstream neighbor cells (channel cells only).

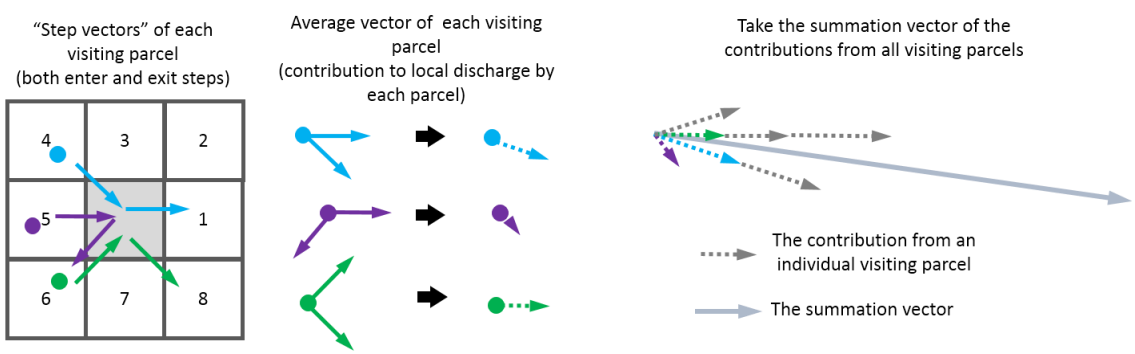

Figure 3-3. Calculation of the direction of the cell discharge vector. The cell discharge vector will take the direction of the summation vector of all contributions from each visiting water parcel, and for N_{visit} visiting parcels its magnitude will be $Q_{cell} = N_{visit} Q_p$.

In Figure 3-4 we plot example outputs of the cell discharge vectors after calculation steps 1 and 10. Plots only take a portion of the channel of 50 cells long to show more details. Note although, as might be expected a close to uniform field is obtained, a perfectly

uniform flow field is never achieved due to the stochastic nature of the random walk. Essentially our result here is dynamically equivalent to a uniform flow field plus a random oscillating disturbance. Later in this chapter we will show this small disturbance plays an important role in the emergent behaviors of channel meander migration.

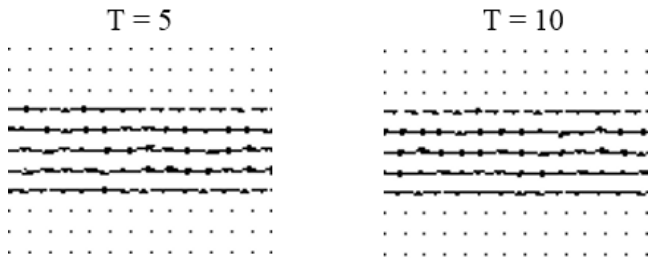

Figure 3-4. Sample vector field (cropped into a 11*14 sub-area of the domain) of the calculated cell discharge vectors at different calculation steps (T=5 and T=10). Note the oscillations caused by the stochastic nature of the random walk.

3.2.1. Deposition and erosion process

So far we have not introduced the conversion between channel and land cells, i.e., rules for deposition and erosion. In the following we build these rules based on the calculated r cell discharge vectors. This is the same idea as the erasing process in Chapter 2 where abandoned channel cells are selected according to the pseudo discharge magnitude, only that in this model the discharge vectors are more realistic and we include the conversion from a land cell to a channel cell as well.

To simplify the problem, we assume that the overall deposition and erosion in the domain is at equilibrium that there isn't any net gain or loss of mass in the system. By doing this, we are assuming that wherever the flow condition is favorable for deposition, there's always enough sediment in the flow to fill that spot, also wherever the flow condition is favorable for erosion, the sediment will be removed and carried away by the water flow

immediately. As noted above, there are no sediment parcels routed through the domain. Instead, during each calculation step, after the routing of water parcels and the calculation of cell discharge vectors, we do a sweep through the channel cells in the domain and change the state of cells from channel to land or from land to channel according to the relative magnitude of the cell discharge Q_{cell} to the reference value Q_0 (Eq. (3.2)). Two rules are used for this step:

- Deposition rule (converting a channel cell to a land cell)

Whenever the magnitude of the calculated discharge vector is less than a factor of the reference discharge, i.e.

$$Q_{cell} < Q_{dep} = k_{dep} Q_0, \quad 0.5 \le k_{dep} \le 0.9, \tag{3.4}$$

the cell is converted to a land cell; a process that could mimic the formation of channel bars.

- Erosion rule (converting a land cell to a channel cell)

Whenever the magnitude of the calculated discharge vector is greater than a factor of the reference discharge, i.e.

$$Q_{cell} > Q_{ero} = k_{ero} Q_0, \quad 1.1 \le k_{ero} \le 2.0, \tag{3.5}$$

all land cells adjacent to (neighboring on) the channel cell of interest are converted to channel cells, a process regarded as mimicking bank erosion. Note following such a step all the switched cells are assigned the reference cell discharge value, Q_0.

The deposition routine converts channel cells with smaller discharge into land cells and narrows down part of the channel by leaving fewer channel cells across the stream. This process cannot go endlessly because the narrower parts consequently have higher discharge per cell and are unlikely to continue the narrowing process. The erosion routine expands the channel width by converting land cells immediately neighboring to the channel cells with high discharge into channel cells and behaves like bank erosion which tends to expand channel width. Similar to the deposition process, the expanding process

is limited since wider channel tends to have smaller discharge per cell. These two processes are demonstrated in Figure 3-5. For these simple runs we use a domain size of 50 cells long and 40 cells wide. In the plot we only crop out the channel portion to display.

Figure 3-5. Three series of channel evolution with selective erosion and deposition processes: (a) Channel narrows down by deposition process only (k_{dep} = 0.8, k_{ero} is a large value to eliminate the possibility of erosion); (b) Channel expands by erosion process only (k_{dep} is zero to eliminate the possibility of deposition, k_{ero} = 1.2); (c)

Channel maintains an equilibrium width with both erosion and deposition processes working (k_{dep} = 0.8, k_{ero} = 1.2).

Despite the simplicity, these two competing processes work together to maintain an equilibrium channel width as the main channel belt moves around, which crudely agrees with the framework for modeling the migration of meandering rivers by Parker et al. (2011). Essentially there are separate relations for the migration of the eroding bank and the depositing bank, instead of treating the depositing bank as moving passively in response to the retreat of the eroding bank.

3.2.2. Refinement of the weighted random walk

In the basic setting, the weighted random walk of a parcel is limited to three immediate downstream neighbors – assuming flow is going from left to right. In order to accommodate a migrating channel belt, the definition of downstream direction should be spatially and temporally variable. As a result, the choice of neighbors when routing parcels should take into account a changing downstream direction. Here we design a few simple rules to estimate a "routing direction" at each channel cell in the domain.

The challenge is how to find a reasonable "downstream" direction in a cellular framework, which is different from directly solving the partial differential equations governing the flow field, where both flow direction and magnitude are solved in an iterative way. This difficulty varies with different geomorphologic environments. Here are some examples where it is relatively easy to define a downstream direction:

- Erosional landscapes and alluvial fans: the transport of water and sediment is predominately controlled by the slope of topography, therefore the best definition of downstream direction naturally follows the steepest descent;
- Flow in a relatively straight channel: downstream direction is the reach-averaged flow direction.

However, the definition of 'downstream' gets ambiguous when dealing with environments like meandering rivers and a river delta with complex channel networks. First, a uniform direction cannot work for the whole domain as flow direction changes spatially; second, even at a fixed location the directions changes significantly over time; third, topographical influence are not as dominant as in environments like erosional landscapes which is dominated by hill slope transport. A further discussion on this issue will be provided in the next chapter.

To move forward at this point, we consider two physical processes dictating the flow direction, (i) at an instant in time flow has a tendency to continue in the same direction as the direction at the previous instant – a process we call inertia, (ii) in the absence of any other drivers the flow will go down slope – the effect of gravity. We explain in detail below how to combine these two processes and obtain a single vector at each cell in the domain as the local "routing direction". Please note that the model remains as a two-dimensional plan-view model where "going down slope" is globally speaking and we do not intend to resolve either topography or water pressure gradient. The "high" and "low" places are pre-defined for the whole domain as a constant slope, $\vec{S} = (1,0)$, which is a unit vector pointing from left to right.

With the cell discharge vector calculated from the previous calculation step, $\vec{Q}_{cell}^{\,old}$, we can define a unit vector which represents the routing direction of inertia alone as

$$\vec{F}_{inertia} = \frac{\vec{Q}_{cell}^{\,old}}{\left|\vec{Q}_{cell}^{\,old}\right|}, \tag{3.6}$$

and a similar unit vector to represent the routing direction of the slope alone as

$$\vec{F}_{slope} = \frac{\vec{S}}{\left|\vec{S}\right|}. \tag{3.7}$$

In equation (3.6) we use flow information from the previous calculation step for the estimation of inertia in the new step. This has been shown in Bates et al. (2010) to improve flow routing.

A combined routing direction $\vec{F}$ is obtained by taking a weighted summation of $\vec{F}_{inertia}$ and $\vec{F}_{slope}$ and normalizing the resultant vector to a unit vector:

$$\vec{F}^* = (1-\gamma)\vec{F}_{inertia} + \gamma\vec{F}_{slope}$$
$$\vec{F} = \frac{\vec{F}^*}{\left|\vec{F}^*\right|} \tag{3.8}$$

The partitioning coefficient γ is typically a small number, in the range of 0 to 0.1. Essentially γ measures the overall "steepness" of the domain. With a γ value larger than 0.1, the behavior of the resultant channel planform is very close to the basic case, where water is routed strictly from left to right (Figure 3-3, Figure 3-4, and Figure 3-5). In the discussion section, we will explain in more detail the limitation and potential improvement of the current combination scheme.

The routing weights of the neighbors for a given cell are calculated through the vector dot product:

$$w_i = \frac{\max\left(0, \vec{F} \cdot \vec{d}_i\right)}{\Delta_i} \quad \text{if neighbor } i \text{ is "channel"}$$
$$w_i = 0 \quad \text{if neighbor } i \text{ is "land"} \tag{3.9}$$

Where $\vec{d}_i$ (the cellular direction) is a unit vector pointing to neighbor *i* from the given cell. And Δ_i (the cellular distance) takes a value of 1 for cells in main compass directions and a value of $\sqrt{2}$ for corner cells. Examples are shown in Figure 3-6:

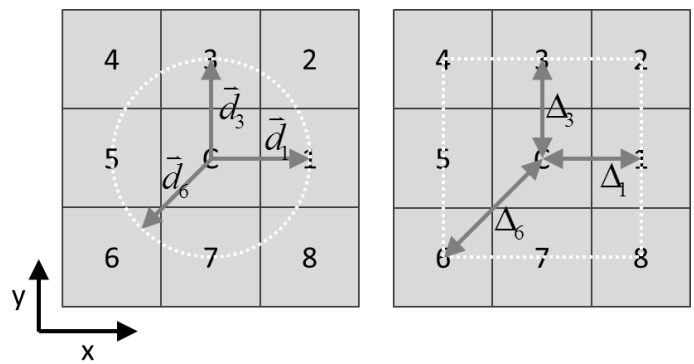

Figure 3-6. Definition of cellular direction $\vec{d}_i$, cellular distance Δ_i. For example, $\vec{d}_1 = (1,0)$, $\vec{d}_6 = \left(-\frac{1}{\sqrt{2}}, -\frac{1}{\sqrt{2}}\right)$, $\Delta_1 = 1$, $\Delta_6 = \sqrt{2}$.

The effect of using the dot product in Eq. (3.9) is to give the highest weights to the neighbor cell that is most aligned with the routing direction $\vec{F}$, which in spirit is close to the "D-infinity" hill slope flow routing scheme developed by Tarboton (1997). We can then use the weighted random walk equation (2.1)

$$p_j = \frac{w_j}{\sum_{nb=1}^{8} w_{nb}}, \; j = 1,2..8,$$

to calculate routing probabilities p_j. Small modification of the probabilities are required to mitigate for rare events. If all the routing weights are zero, we set the routing probability of moving to the right (east) neighbor as unity and all the other routing probabilities as zero. If the target cell to the right cell is a land cell it is also converted to a channel cell. This correction will allow for chute type cut-offs, which are often observed in natural meandering rivers.

In summary the input parameters of the current model are:

(1) The coefficients of threshold discharge for erosion and deposition, k_{ero}, k_{dep};

(2) The partitioning coefficient between the contribution to the routing direction by inertia and by slope, γ.

Our interpretation for the physical meaning of the parameters are: the value of k_{ero} represents bank strength, a larger value meaning stronger bank; the value of γ represents valley slope, a larger value meaning steeper slope. However, the physical meaning of k_{dep} is still unclear. Previously Figure 3-5 shows that k_{ero} and k_{dep} together control the migration rate of the channel. In the results section, we fix k_{dep} at a constant value ($k_{dep} = 0.8$) and investigate the effects of k_{ero} and γ.

3.3. Results and analysis

All the results reported below are constructed on the same domain size (200 cells long and 80 cells wide) and initial channel dimension (5 cells wide), if not specified otherwise.

Table 3-2. List of meander river model runs and parameter values.

Run number #	k_{dep}	k_{ero}	γ
1	0.8	1.5	0
2	0.8	1.2	0.01
3	0.8	1.5	0.01
4	0.8	2.0	0.01
5	0.8	1.5	0.02

3.3.1 Development of meander bends (run #1)

In first run, the routing direction is contributed by inertia alone. As mentioned before (Figure 3-4), the weight random walk method gives a supposedly uniform flow field oscillations. These small oscillations introduce irregularity to the bank, which causes the channel to turn. Wherever channel turns direction, the effects of inertia will force discharge to concentrate towards the outer bank (Figure 3-7). As a result, channels are more likely to erode the outer bank while the weak discharge next to inner bank causes deposition, and the channel belt moves outward. This captures the one of the basic mechanics of the formation of a meander bend.

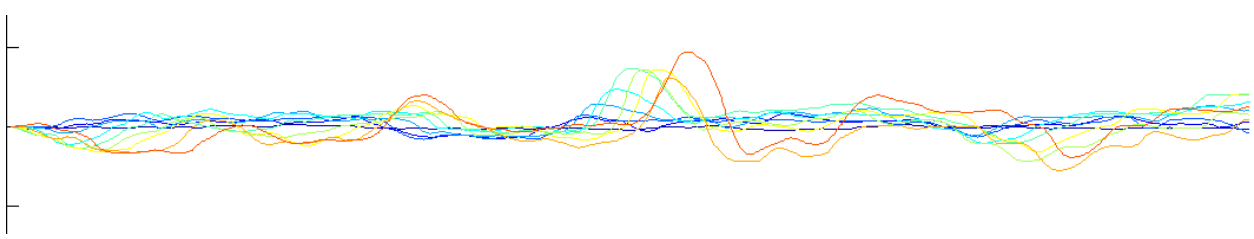

Figure 3-7. Initial development of meander bends from a straight channel (vertical axis is 4 times exaggerated).

The complexity of the meander channel can be measured with sinuosity *S*, which is defined as the ratio of curvilinear length of the river to the valley length. The meander bends grow and increase the sinuosity of resolved channel planform. In the following we

show that this simple model is able to capture a wide range of meander river behaviors, such as translation, extension, rotation, single and compound bends (Figure 3-7).

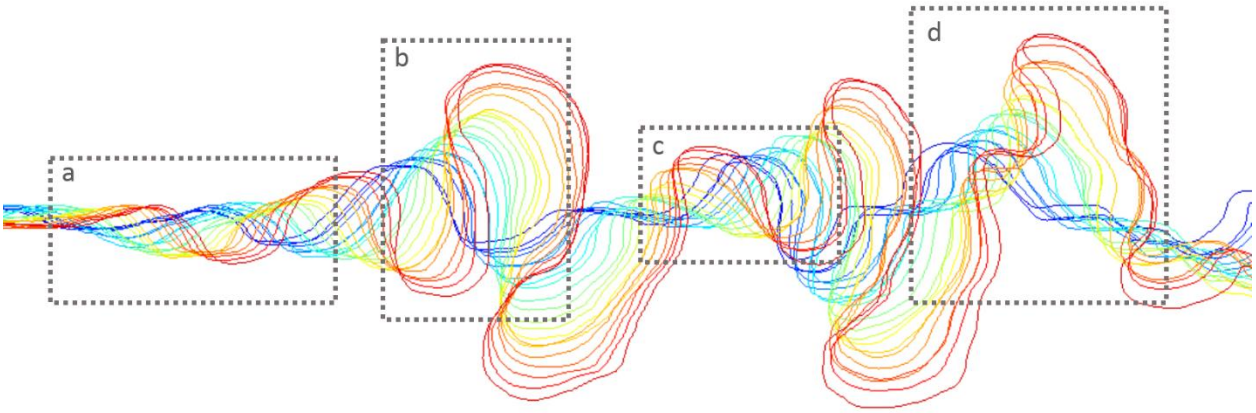

Figure 3-8. Meander behaviors captured in the model results. (a) Translation; (b) Extension; (c) Rotation; (d) Conversion to a compound loop.

Another feature to be noted is the upstream skewness of the meander bends (Figure 3-8). As explained by the cumulative influences from curvature on migration rate, a slow decay in the upstream curvature influence caused by a low flow resistance leads to an increase in the downstream translation and upstream skewness of meander bends (Güneralp and Rhoads, 2009b).

In the real world, as the bends grow and rotate in a limited space, the channel shortens by making two types of cutoffs: (1) a neck cutoff by joining the two ends of a bend (Figure 3-9a) and, (2) a chute cutoff by water escaping the channel and eroding the land to form a new path, which usually rejoins the original channel somewhere downstream (Figure 3-9b). Usually these shorter paths are preferred water flow paths as they have a higher slope due to shortened distance. In our model we don't resolve detailed topography to measure local slope, but results show realistic cutoff patterns (Figure 3-9). We do not view these as a physical representation of the real cutoff processes, only to emphasize the model's ability to "cure" infinite growth of meander bends in a way that's mimicking nature.

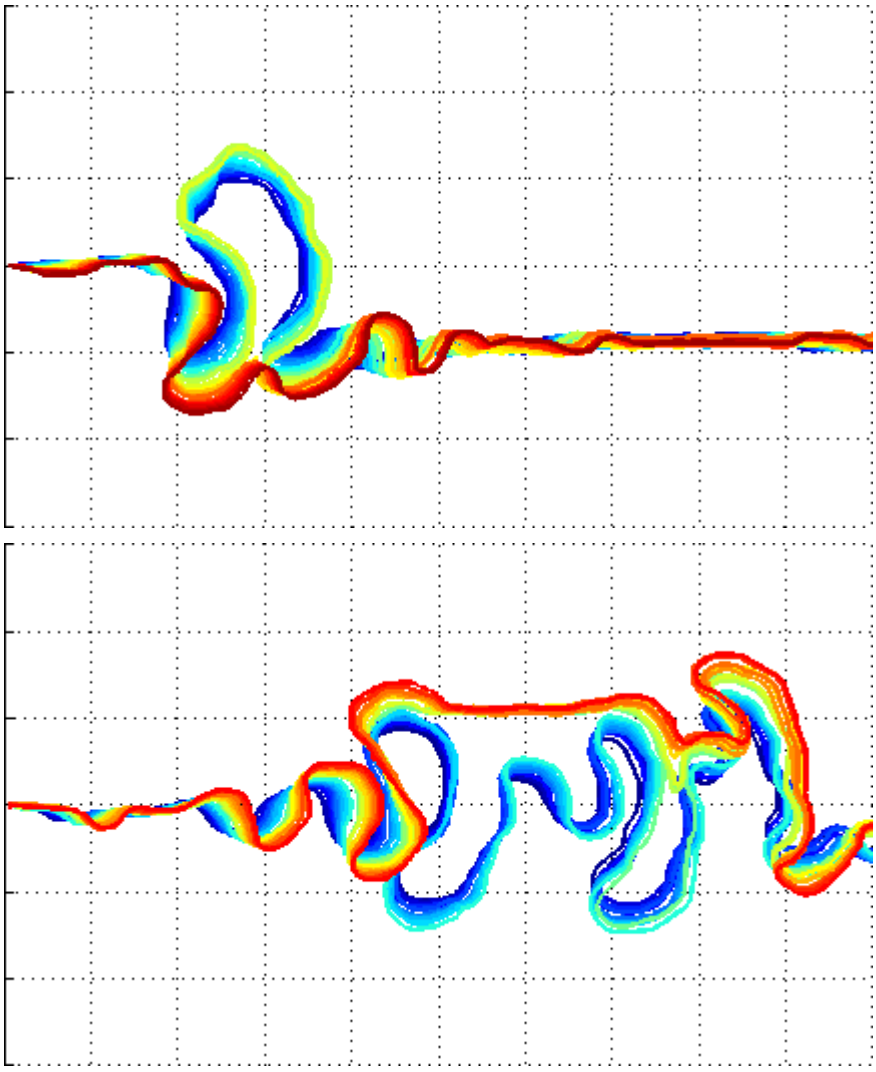

Figure 3-9. Cutoffs in the model results. Upper plot: a neck cutoff. Lower plot: a chute cutoff.

The dynamic balance between the growth of meander bends and cutoffs can be observed from the time series of sinuosity *S* as a function of calculation steps (Figure 3-10). Note the exponential increase before a major cutoff.

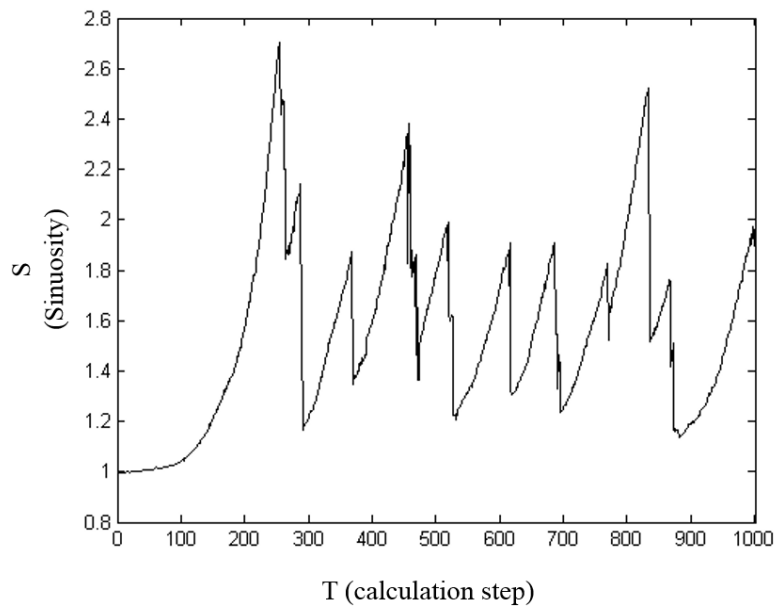

Figure 3-10. Sinuosity (S) as a function of calculation step (T); note the exponential-like growth before any major cut-off.

3.3.2 The effect of bank strength (run #2, #3, and #4)

Overall, as k_{ero} increases from the minimum possible value, $k_{ero} = 1$, to a considerably large value, $k_{ero} = 2.0$ (note that with a value larger than 2 it's hard to produce lateral migration) the sinuosity starts from a little more than 1 (meaning a straight channel), then increases to almost 3, and then decreases. The hypothesis is that a moderate cohesiveness of the bank helps the formation of meanders while if the cohesion is too strong (e.g. with a k_{ero} value larger than 2), it is difficult for the river to migrate horizontally.

Note that erosion doesn't work alone to create lateral migration and meanders. Without deposition at the inner bank the channel belt will expand and the ability to erode also decreases as the discharge per unit width decreases. Therefore a larger value of k_{dep} also participates in the model by "pushing" the channel belt in the direction that it's eroding into.

According to Schumm (Schumm, 1967), rivers with coarser sediment have greater meander wavelengths. From Figure 3-11, it's clear that channel meander wavelength decreases from top to bottom (bank strength from weak to strong). We plot the sinuosity of the three runs as a function of calculation step in Figure 3-12.

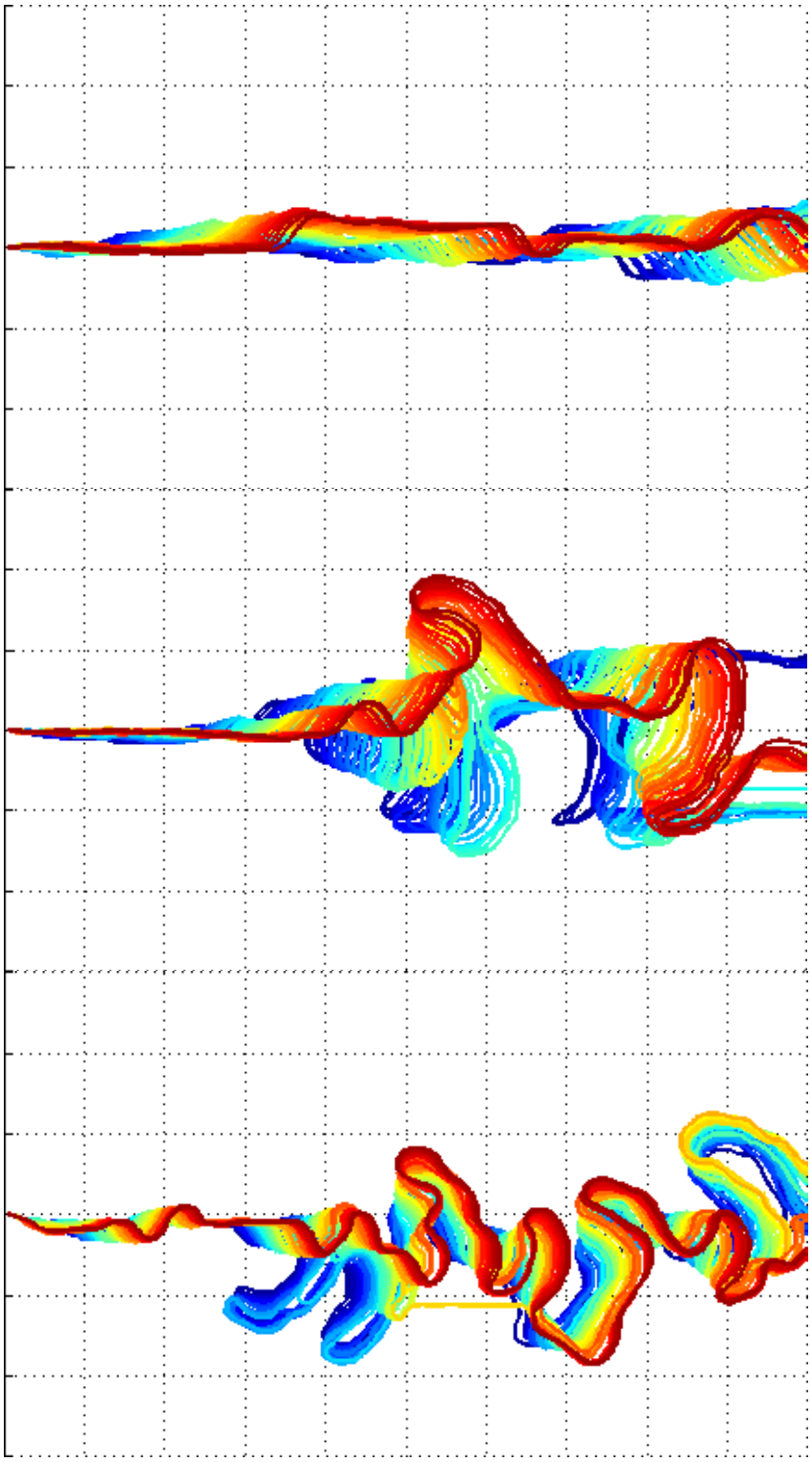

Figure 3-11. Different channel planform by varying bank strength (the value of k_{ero}). From top to bottom: k_{ero} = 1.2; 1.5; 2.0. All runs have k_{dep} = 0.8 and slope, γ = 0.01.

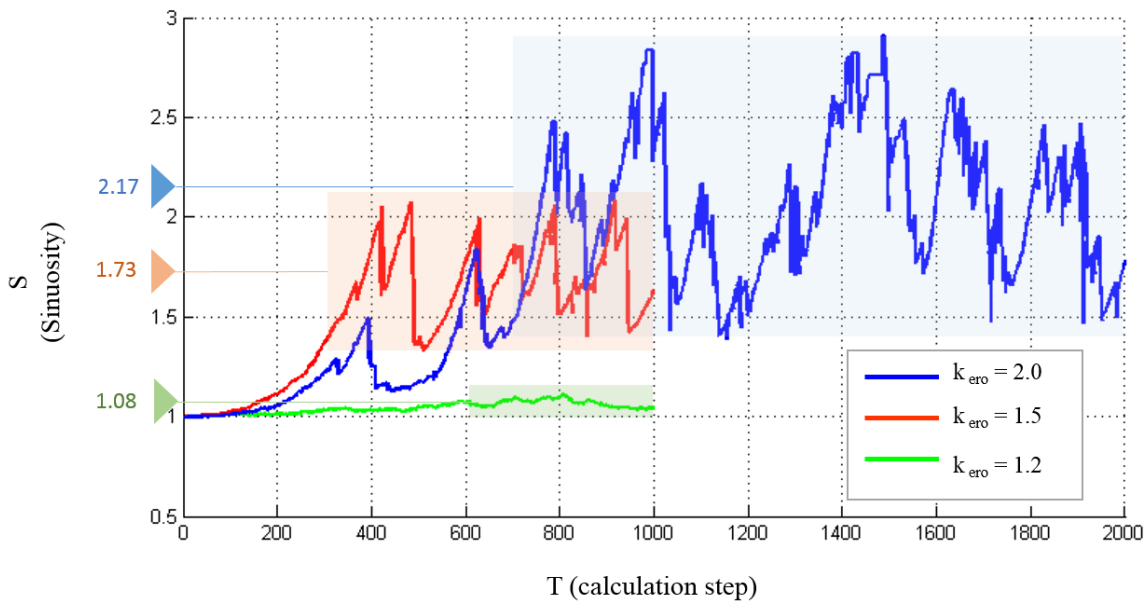

Figure 3-12. Sinuosity time series and average value from model run #2 ($k_{ero} = 1.2$), #3 ($k_{ero} = 1.5$) and #4 ($k_{ero} = 2.0$). A stronger bank (higher value of k_{ero}) produces more meanders.

3.3.3 The effect of channel slope (run #1, #4, #5)

Here channel slope refers to the global slope of the whole reach, which is the valley slope. In this model this slope is measured by the value of parameter γ, the partitioning coefficient between the contribution to routing direction from inertia and from slope. Figure 3-12 shows the results with different γ values while other parameters kept constant. It's clear that with a larger value of γ, the sinuosity of the channel is greatly reduced.

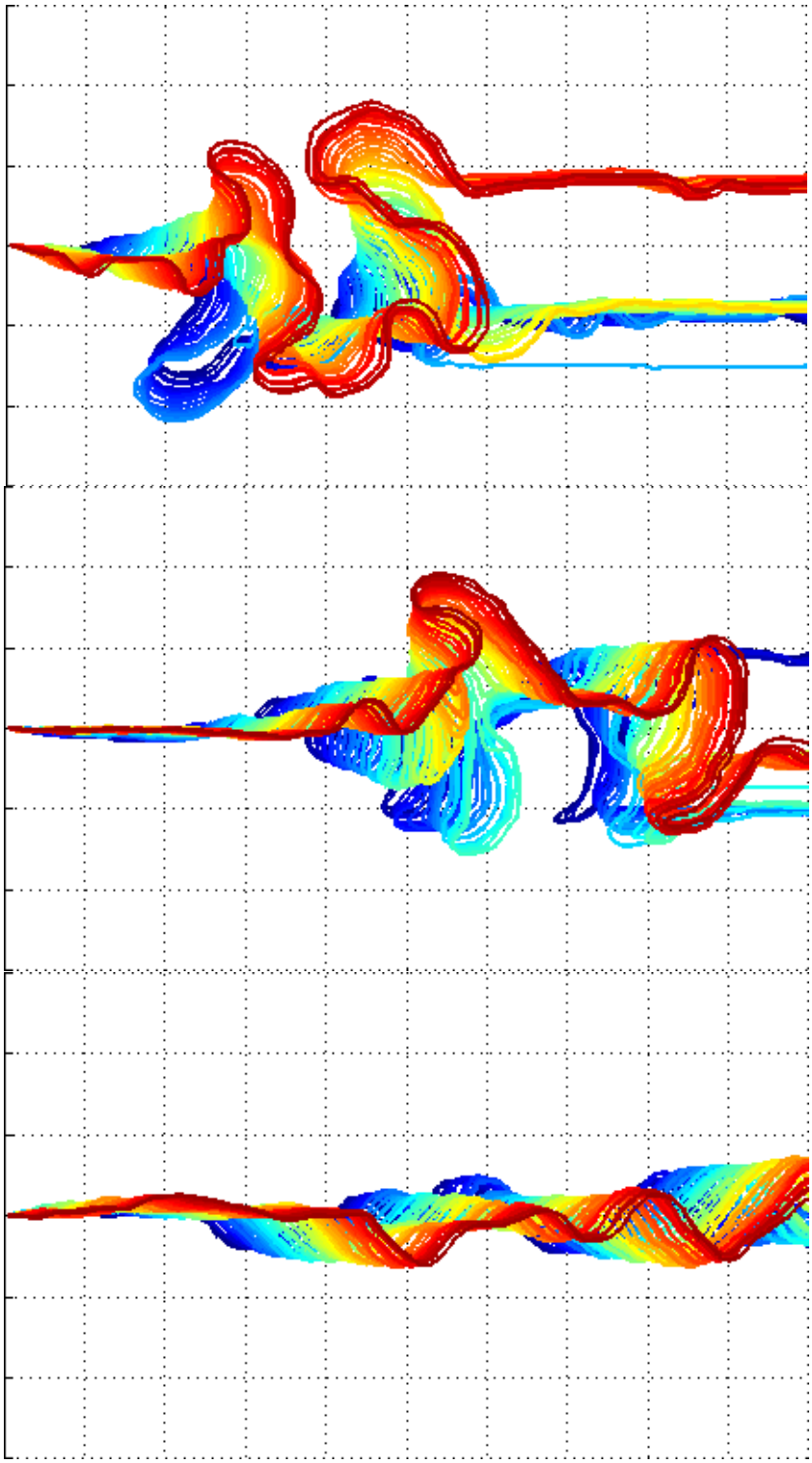

Figure 3-13. Different channel planform by varying slope (the value of γ). From top to bottom: γ = 0, 0.01, 0.02. All runs have k_{dep} = 0.8 and slope, k_{ero} = 1.5.

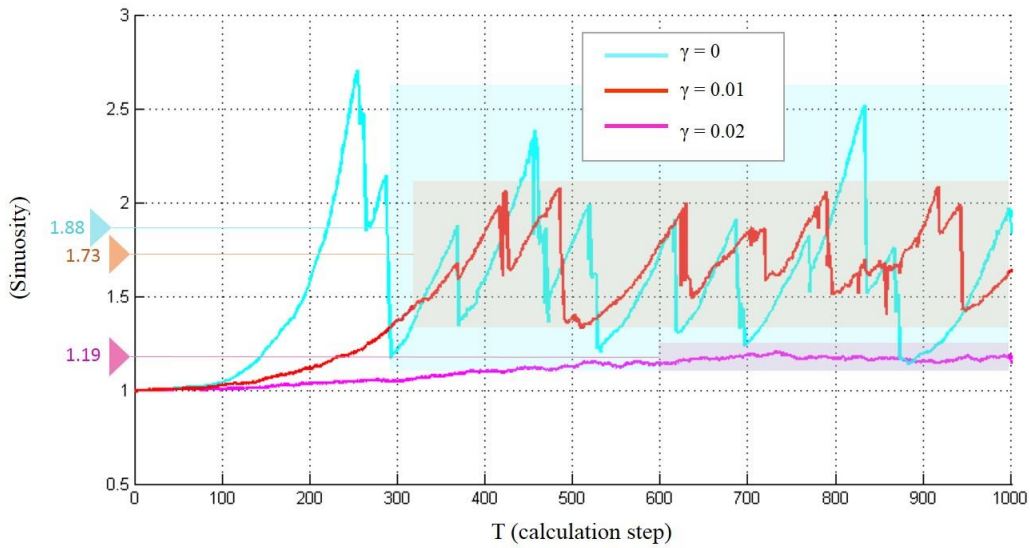

Figure 3-14. Sinuosity time series and average value from model run #1 ($\gamma = 0$), #4 ($\gamma = 0.01$) and #5 ($\gamma = 0.02$). Milder slope (lower value of γ) produces more meanders.

3.4. Discussion

<u>Curvature-driven vs. topography-driven</u>

Two flow mechanisms control river meandering (Dietrich and Smith, 1983). The first is curvature-driven and the second is topography-driven. Curvature introduces a redistribution of flow momentum that causes a decrease in the bed-shear stress along the inner bank and an increase in the bead shear stress along the outer bank (also called cutbank). Topography steers water flow in the way that point bar deflects water towards the outer bank.

In this model we only capture curvature-driven meandering, although a more quantitative analysis is required to compare to the convolution model from Howard et al. (1984), in which the effects of local curvature decreases in the downstream direction and the migration rate at any given location is the cumulative effects from upstream curvatures.

To capture topography-driven meandering, a detailed model that resolves bed topography is required. In Chapter 4 we show an extension of this planform model that resolves topography and routes water and sediment accordingly.

Connection to existing bank erosion models

In our model we use parameter k_{ero} to control the strength of the bank, which basically use a threshold cell discharge to determine whether to convert a land cell on the bank to channel cell. This matches well with the empirical bank-erosion model from Ikeda et al. (1981), a linear relationship between excess near-bank velocity and bank erosion rate:

$$\zeta(s) = E_0 u_b(s)$$

Where E_0 is bank-erosion coefficient, which depends on the soil-mechanical properties of the material along the bank (Parker and Andrews, 1986); u_b is the excess near-bank velocity; ζ is migration rate along the channel axis *s*.

One possible future improvement is that oxbow lakes (remnant channel loops after cutoff) are usually filled with fine sediment and become sediment plugs. In this planform model it is possible to incorporate this process by introducing a different threshold cell discharge coefficient (k_{ero}).

Meandering vs. braiding

Despite the success in producing realistic meander bends, we realize that this simple plan-form weighted random walk model has not produced channel braiding. Our hypothesis is that what's missing in this model framework is a flow routing based on local topographical slope, like the one in the work by Murray and Paola (1994), in which realistic braided rivers are generated from a row-by-row cellular model that routes flow proportional to slopes.

3.5. Conclusion

In this chapter we extended the concept of weighted random walk to create realistic channel meander migration patterns. The concept of calculating a local combined routing direction based on flow inertia and topographical slope is essential for later constructions of our models. We are aware that the simple sediment erosion and deposition rules we used are purely phenomenological and not based on realistic sediment transport formulas. In the next chapter we take this model framework even further to resolve topography with a refined flow routing scheme and more realistic sediment transport rules.

CHAPTER 4

A NEW REDUCED-COMPLEXITY MODEL FOR DELTA FORMATION WITH CHANNEL DYNAMICS

4.1. Introduction

In this Chapter, we modify the weighted-random-walk method developed in Chapter 2 and Chapter 3 to build a quasi-3D model for delta formation that resolves topography and depth-averaged flow field. In detail we apply weighted random walks of separate water and sediment components, where the walking probabilities are constrained by rules based on a hybrid of simplified governing equations for fluid motion and phenomenological representation of sediment transport processes. With suitable rules the model is able to produce delta morphologies that compare well with those produced by much larger and more detailed models (e.g., Delft3D) and with the morphology of deltas in the field. In the results we show (i) different deltas produced with mixtures of coarse and fine grains at different portion ratio, (ii) simulated laboratory fan deltas, (iii) delta shapes responding to different basin geometry, and (iv) recorded stratigraphy by grain size (sand fraction) and by deposition age.

In the model we develop here, the physical basis for rules or parameter values that give good results is not always clear. Rather than papering over these problematic areas, we highlight them as a step towards a better understanding of the intricacies of delta modeling and of what is involved in simplifying them. In the end we point out the strength and weakness of the model and direction of future work along this line.

4.2. Modeling delta formation

The same as models for any natural systems, the most direct delta formation model would solve the governing equations for water flow and sediment particles based on first principles, i.e., the conservation of mass, momentum and energy, given all the necessary

initial and boundary conditions. However, this is still not applicable not only because the limit of computational power but also the potential error accumulation in such complex "full physics" models (Hajek and Wolinsky, 2012). Existing models for delta formation cover a wide range of scales and complexity (Fagherazzi & Overeem 2007, Paola et al. 2011). The spectrum of these models expands from trying to capture everything, creating models that simulate the processes in as much details as current knowledge and computing power allow, to simplifying, even at the risk of losing connection with reality. Depending on the purpose and the processes of interest, models from both sides have given successful examples.

On the simplification side of model complexity, models based on spatially averaged delta surface topography assuming a one-dimensional longitudinal profile have proved to be able to predict average delta dynamics, such as surface profile, the position of shoreline and the position of alluvial-bedrock transition (Parker et al. 2008, Kim et al. 2009, Lorenzo-Trueba et al. 2013). These models, however, cannot provide the detailed structures of deltas, such as topography and channel networks. On the complexity side, to date the most inclusive physics-based delta formation model is Delft3D, which solves a depth-integrated version of the Reynolds-averaged Navier-Stokes equations (shallow water equations) with a turbulence closure term for horizontal Reynolds stresses, and coupled with empirical sediment transport formula based on bed shear stress. Delft3D can resolve deltaic processes from smaller, engineering scales such as river moth bar formation and bifurcation (Edmonds & Slingerland, 2007) to larger, geological scales such as the whole delta morphodynamics controlled by sediment cohesion (Edmonds & Slingerland, 2009), wave, tides and antecedent stratigraphy (Geleynse et al. 2010). Although there's still open debate on the weakness of Delft3D, such as its inability to properly treat bank erosion, there are two obstacles in applying it for intensive hypothesis testing and exploratory coupling with processes beyond hydrodynamics and geomorphodyanmics: the computational cost and the relatively rigid and complicated structure for people without special training to handle. We would like to emphasize that the computational cost is not the only concern. Actually in many cases, especially for the formation of deltas, the flexibility of a model to allow explorations directly based on

interpretations of the physical processes controlling the behaviors of the system rather than the detailed solution of the governing equations is of greater importance – one of the fundamental philosophies of the so called "Reduced Complexity Models (RCMs)". RCMs reside in the middle ground of the model complexity spectrum. Sometimes they are referred to as "process-based" or "rule-based" models by their descriptive constructions and intuitive simplification over a hierarchical natural processes. A representative form of RCM is cellular geomorphodynamic models such as the pioneer work on braided rivers by Murray and Paola (1994). Another example of RCM is the delta formation model by Seybold et al. (2007, 2009), which calculates water flux field with a set of simplified hydrodynamic equations which is equivalent to a diffusive-wave form of the shallow water equations with a constant diffusivity. Other RCM examples include an avulsion delta building model by Sun et al. (2002) and a channel-floodplain co-evolution delta building model, "AquaTellUS" by Overeem et al. (2005).

The difficulties of building a RCM for delta formation lie in the following aspects: (i) the mild slope of the majority of river deltas (10^{-4}~10^{-5}) doesn't provide an easy guide for typical cellular flow routing – one of the most common form of RCM (ii) the mild slope together with relatively deep, slow channel flow create a low-Froude-number environment that flow senses information from both upstream and downstream directions, making it difficult to design localized rules which are essential for RCMs, (iii) the self-emergent distributary channel network also poses uncertainties which do not exists in other environments such as tributary channels in erosional landscapes, (iv) most river deltas have suspended load and wash load as the primary sediment input component, which is more difficult to model than bed load. Here we would also like to point out that the low-Froude-number flow condition also offers a feature called "rigid-lid water surface", that the elevation of water free surface is almost decoupled from the topography of the bed, a feature providing computational advantages. In this work, we try to tackle the above difficulties with the "weighted random walk" method. Detailed model construction is given in the next section.

4.3 Model construction

The model framework is along the line of Chapter 2 and 3, which use a grid of cells and weighted random walk of parcels to calculate water flow and sediment transport. Different from previous two chapters, this new model not only produces plan-form delta formation with channels but also resolves topography.

4.3.1 Model setup

The basic physical setting is a rectangular basin of a constant depth of water (Figure 4-1). One boundary is a wall boundary with a short channel inlet at the center. The other three boundaries are ocean boundaries with a fixed sea level, H_{SL}. The channel inlet has a water depth of h_0, which we will use as a 'reference flow depth', and flow velocity U_0, which we will use as a 'reference flow velocity'. The basin has a water depth of h_B. To be simple, we assume a constant water input discharge Q_{w0} (m^3/sec) and a constant sediment input Q_{s0} (m^3/sec) coming in to the basic from the channel inlet.

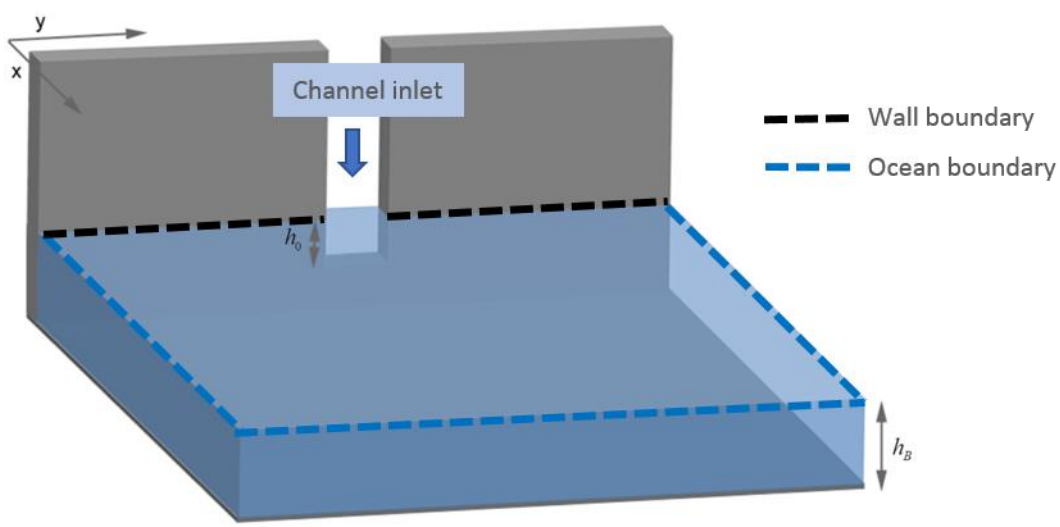

Figure 4-1. Illustration of the basin, boundaries and inlet channel.

The same as the parcel-based weighted random walk model we introduced in previous chapters, the domain is discretized into a lattice grid of square cells (Figure 4-2). Cell size is δ_c, which value depends on the scale of the model run, e.g. 50 meters for a field scale delta and 2 centimeters for a laboratory scale fan. The total number of cells along the dip direction (from the inlet, into the basin) is N_X and the number of cells along the strike direction (perpendicular to the inlet, across the basin) is N_Y. Typically N_X and N_Y are both on the order of a hundred, with N_Y being roughly twice as larger and N_X to allow a semi-circular growth. The inlet has a width of N_0 cells. Typically N_0 is around 5. The primary quantities associated with each cell include: (i) water unit discharge vector $\vec{q}_w = (q_x, q_y)$, (ii) water surface elevation H, (iii) bed elevation η. The model goes forward with time steps and the primary quantities are updated at each time step. Other useful quantities such as velocity vector $\vec{u} = (u_x, u_y)$ and water depth h can be easily calculated from the primary quantities by: $h = H - \eta$ and $\vec{u} = \frac{\vec{q}_w}{h}$.

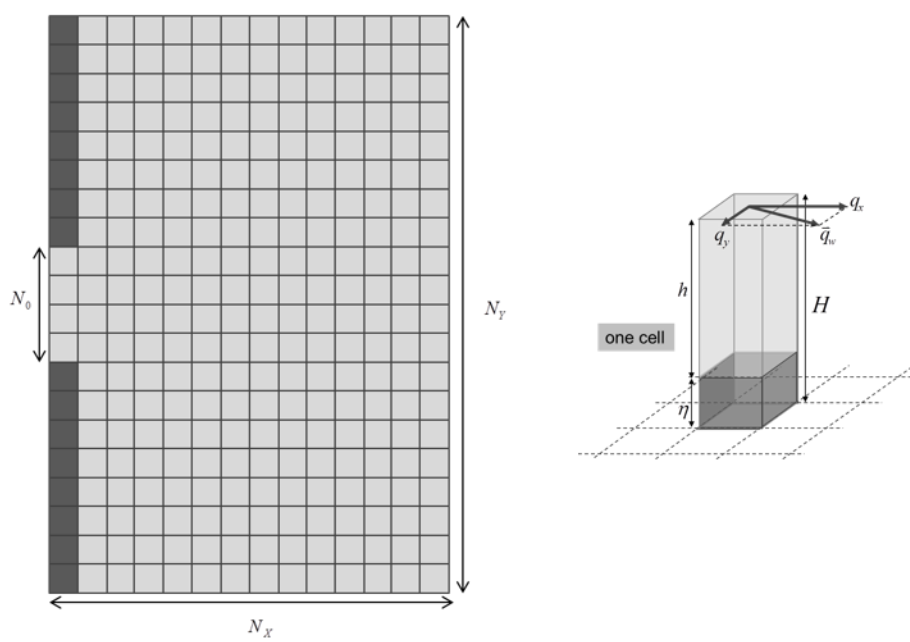

Figure 4-2. Cartoon of the lattice grid and the primary quantities at each cell (water unit discharge, water surface elevation and bed elevation). Note that the total number of cells are reduced for the illustration.

Two types of parcels that carry a water or sediment attribute are routed through the domain. A time step is defined by the addition of n_w water parcels and n_s sediment parcels. This is made through a sequence of water parcels carrying an equal fraction of the total input water discharge during a time step followed by sediment parcels carrying an equal fraction of the total input sediment discharge during a time step.

Within each model run, the size of the time step Δt is constant. The choice of Δt is a balance between computation efficiency and model stability. In each time step, the total amount of sediment added to the domain is measured by $\Delta V_s = Q_{s0}\Delta t$. A smaller ΔV_s means less changes to the topography, and allows the cellular routing scheme to perform better with a more consistent terrain, but obviously it will take more CPU time to build the delta to a certain size. Here we introduce a reference volume,

$$V_0 = h_0 \delta_c^2 , \tag{4.1}$$

which is the volume of a channel inlet cell from the bed to water surface. If we assume that channels on the formed delta self-organizes in scale with the graded inlet channel, this reference volume gives a good measurement of the topographical change on the growing delta. Currently we set the time step size so that the sediment volume added in each time step satisfies:

$$\Delta V_s = 0.1 * N_0^2 * V_0 . \tag{4.2}$$

Therefore time step size is given by:

$$\Delta t = \frac{0.1 * N_0^2 * V_0}{Q_{s0}} . \tag{4.3}$$

4.3.2 Model operation

The operations can best be understood by describing the process of a time step. There are four distinct phases: (1) the addition and routing of the water, (2) updating of the water surface elevation, (3) routing the sediment parcels and updating the bed elevation through deposition and erosion, (4) updating of the "routing direction", a vector field that determines the direction of flow through each cell in the domain. Each of these phases is described in turn.

To prepare, we divide the upstream water discharge (Q_{w0}) and the total sediment input volume during a time step (ΔV_s) into parcels. Typically, we use n_w = 2000 water parcels and each water parcel carries equal amount of discharge:

$$Q_{p\_water} = \frac{Q_{w0}}{n_w}, \tag{4.4}$$

And we use n_s = 2000 sediment parcels and each sediment parcel carries equal amount of sediment volume:

$$V_{p\_sed} = \frac{\Delta V_s}{n_s}. \tag{4.5}$$

Phase 1: water routing

At start of a time step we assume that we have built a delta with known shape and topography, i.e. at each cell we have a value of the water surface elevation H, bed elevation η, and water depth (difference between the water surface elevation and the bed elevation) h. We also have, at each cell, a unit vector $\vec{F}$, referred to as the "routing direction", which in essence is an indicator of the downstream direction of flow through that cell.

For the purpose of routing water, we define a binary cell state: 0 – dry, 1 – wet. This is done by doing a sweep through the domain and mark cells with a water depth larger than a threshold value h_{dry} as wet cells.

The process in the first part of the time step requires us to route, in turn, each of the water parcels through the domain. When the parcel is at a given cell, this requires making a choice of which of the 8 neighbor cells it will move to. We achieve this by using a so called "weighted random walk" where the movement is dictated by a predefined probability distribution between the 8 neighbor cells. The specification of the probability distribution is as follows:

At a given center cell, first we calculate the routing weights for the 8 neighbor cells. With the local routing direction $\vec{F}$ specified, the routing weights are determined by two factors: (i) the angle between the relative direction of neighbor cell *i* to the center cell to the routing direction, which we will estimate using the same dot product method as in Chapter 3, and (ii) the resistance to the flow from each cell *i*. The second factor is an addition to the previous meander model in Chapter 3 where the simple planform model doesn't resolve details to give local resistance to the flow. In this model we calculate the routing weight of neighbor cell *i* as:

$$w_i = \frac{\frac{1}{R_i}\max\left(0, \vec{F}\cdot\vec{d}_i\right)}{\Delta_i}$$
$$w_i = \frac{h_i \max\left(0, \vec{F}\cdot\vec{d}_i\right)}{\Delta_i} \tag{4.6}$$

Where resistance R_i is estimated as a function of local water depth h_i:

$$R_i = \frac{1}{h_i^{\theta}}. \tag{4.7}$$

Currently the exponent θ is set to 1.

As defined in Chapter 3, $\vec{d}_i$ (the cellular direction) is a unit vector pointing to neighbor *i* from the given cell. And Δ_i is the cellular distance (taking a value of 1 for cells in main

compass directions and a value of $\sqrt{2}$ for corner cells. Examples can be found in Figure 3-5.

The weights above are only calculated for "wet" neighbor cells of the given channel cell. All "dry" neighbor cells take a default weight value of 0. At each channel cell we can then use the weighted random walk equation (2.1), $p_i = \frac{w_i}{\sum_{nb=1}^{8} w_{nb}}, i = 1,2..8$, to calculate routing probabilities p_i.

To obtain a discharge vector at each cell based on the motion of visiting water parcels, similar to the previous chapter our starting point is to construct, for each visiting parcel, an average vector of the input and output vectors, see Figure 2-6. So the result is, for each channel cell, a set (size N_{visit}) of vectors each expressing the average path of a visiting parcel through that cell. A summation of this set of vectors provides, after appropriate normalization, a representative direction for water parcels through the cell. In this way, a vector with this direction and a magnitude

$$Q_{cell} = N_{visit} Q_{p\_water} \tag{4.8}$$

can be regarded as a discharge vector for the cell (Figure 4-3) (the same as Figure 3-3).

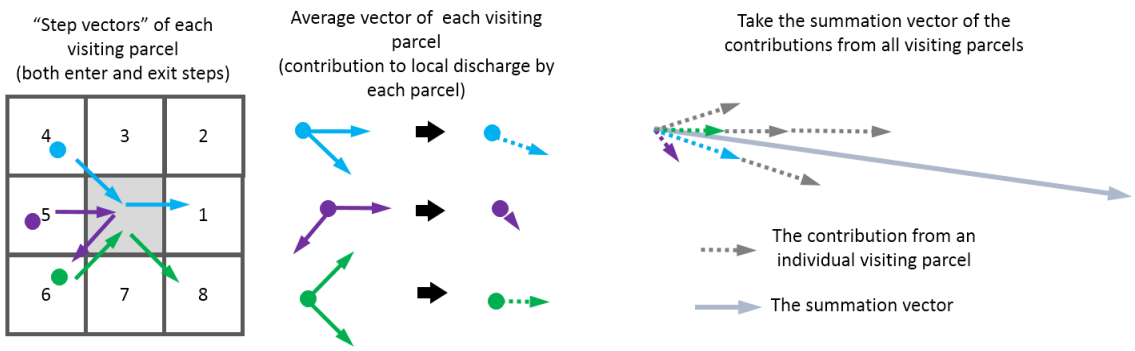

Figure 4-3. Calculation of the direction of the cell representative discharge vector. The representative discharge vector will take the direction of the summation vector of all contributions from each visiting water parcel, and for N_{visit} visiting parcels its magnitude will be $Q_{cell} = N_{visit} Q_{p\_water}$.

Then for the purpose of sediment transport later, we need to estimate local flow unit discharge and velocity. To do this we take the cell discharge vector (m^3/s) and divide it by the cell size δ_c to obtain a unit discharge vector (m^2/s):

$$\vec{q}_w = \frac{\vec{Q}_{cell}}{\delta_c} \tag{4.9}$$

The subscript "w" is to distinguish from the sediment flux calculation later.

Phase 2: water surface calculation

Water surface profile is essential in this model not only that it participates in the calculation of flow depth but also, or even more importantly, the gradient of water surface plays an important role in determine the routing probabilities of water parcels.

In this reduced-complexity model, our goal is to obtain a reasonable surface profile without solving the 2-D hydrodynamic equation. We propose a method that uses a finite difference scheme along the walking path of individual water parcels, which is analogous

to the simplified surface solver developed by Rinaldo and colleagues (Rinaldo et al., 1999).

We assume that on top of the delta, water surface has a constant slope S_0, which is one of the model input parameters and will be referred to as the "reference slope". The value of S_0 is estimated based on the conditions of the system such as sediment properties, sediment and water input and basin geometry. For example, in the simulations we use $S_0 = 0.01$ for laboratory fan delta experiments and $S_0 = 0.00005 \sim 0.0005$ for a field scale river delta. With the constant slope assumption and the downstream water surface boundary condition $H = H_{SL}$, ideally along any streamline we can calculate water surface profile going from downstream to upstream by integrating with the constant slope. In the model, however, instead of tracing flow streamlines, we take advantage of the walking path of water parcels, which can be considered as an approximation form of flow streamlines.

To illustrate the difference between water parcels paths (the "zigzag" version of streamlines) and the real flow streamline, we draw a cartoon in Figure 4-4. In the following we explain how to construct water surface profile along a water parcel path with a given reference slope S_0.

First, we need to locate the part of the path that is on the delta surface, as the part in ocean is considered flat. In general, a water parcel path starts at one of the inlet cells, move from one cell to an adjacent cell, and ends at one of the downstream ocean boundary cells. We distinguish the cells along the path on the formed delta surface and the cells in the open ocean by checking two values at each cell:

- A cell is in the ocean if both of the following criteria are met:
    1) Local bed elevation η is lower than a threshold value η_{shore} (currently set to $\eta_{shore} = H_{SL} - 0.9h_0$)

2) Local flow speed $|\vec{u}|$ is smaller than a threshold value U_{shore} (currently set to $U_{shore} = 0.5U_0$)

- A cell is on the delta if it doesn't meet both criteria for being in the ocean.

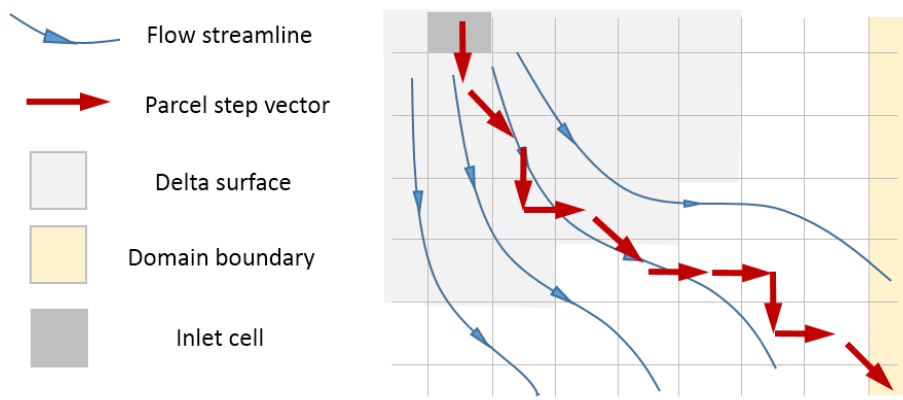

Figure 4-4. A cartoon showing the path of one individual water parcel compared to smooth flow streamlines.

With a given path of a water parcel, the calculation starts from the end of the path and goes backward towards the inlet. For the *k*th cell in the direction of calculation,

- If cell *k* is in the ocean, $H|_k = H_{SL}$;
- If cell *k* is on the delta, $H|_k = H|_{k-1} - \Delta\delta_c \left(\frac{\vec{q}_w}{|\vec{q}_w|} \cdot \vec{d}|_k \right) S_0$, where

  Δ is the cellular distance between the *k*th and (*k-1*)th cell, δ_c is cell size, and $\vec{d}|_k$ is the parcel step vector from cell *k* to cell *k-1*.

  The purpose of the term $\left(\frac{\vec{q}_w}{|\vec{q}_w|} \cdot \vec{d}|_k \right)$ is to take into account the angle between the parcel path and the streamline.

This calculation gives the surface profile along the path of an individual water parcel and is repeated for all water parcel paths. There are two extra situations to be taken care of:

(1) If a cell is visited by multiple water parcels, all the values from each visiting path will be recorded and an average value will be taken among these stored values in the end to obtain a single value for water surface elevation at each cell.

(2) If a cell is not visited by any water parcels, its water surface elevation will remain the old value (from previous time step).

This newly calculated surface profile is recorded as H^{temp}. We then apply a diffuser to smoothen the calculated surface profile which is inherently bumpy due to the 1-D fashion of calculation:

$$H^{smooth} = (1-\varepsilon)H^{temp} + 0.125\varepsilon \sum_{nb=1}^{8} H_{nb} \tag{4.10}$$

Currently the diffusivity ε is set to 0.1 and we apply the smoothing calculation in equation (4.10) for 10 times in each time step.

In the end, the water surface elevation is updated with an under-relaxation for numerical stability:

$$H^{new} = (1-\varpi)H^{old} + \varpi H^{smooth} \tag{4.11}$$

ϖ is currently set to 0.1, which allow the surface profile to transit very slowly and smoothly from one time step to another.

Phase 3: sediment transport and topography update

Now both flow field, $\vec{q}_w$, and water surface elevation, H, are updated. These two variables will remain constant until the next time step. In order to calculate the changes to the topography in a time step, two sets of rules are designed for the transport, deposition and erosion of sediment. The first set describes the routing of the sediment parcels, and the second set describe the rate of deposition and erosion as the exchange of sediment volume between sediment parcels and the bed. Rules are phenomenological and the goal is to build them with our interpretation of the "behaviors" of the sediment rather than

detailed physical interaction between fluid, sediment and the bed. To this end, we distinguish two types of sediment that have different behaviors in the model:

- Type I sediment will be referred to as "**sand**", which is coarse grain, none cohesive, and transported in the form of bed load;
- Type II sediment will be referred to as "**mud**", which is fine grain, cohesive, and transported in the form of suspended load.

A sediment parcel is either a "sand" parcel or a "mud" parcel. At the beginning of each run, an input parameter f_{sand} will give the portion of sand in the total upstream sediment input. Therefore a total number of $f_{sand} n_s$ parcels are designated as sand parcels and a total number of $(1-f_{sand})n_s$ parcels are designated as sand parcels for each time step.

<u>Routing of the sediment parcels:</u>

For routing sediment parcels we use the same weighted random walk method as the routing of water parcels, with two modifications:

1) Routing direction $\vec{F}$ in equation (4.6) is replaced with the newly calculated water discharge vector $\vec{q}_w$ at the given cell, considering sediment parcels move passively with water flow;
2) Transport resistance for sediment keeps the inverse function of flow depth but has different exponents. The idea is that sediment flux tends to concentrate at the lower portion of the water column and is more likely to follow topographic low areas. For now we use exponent $\theta = 2$ for sand parcels (bed load), and $\theta = 1$ for mud parcels (suspended load). So that the routing weights are:

$$w_i = \frac{\frac{1}{h_i}\max\left(0, \vec{q}_w \cdot \vec{d}_i\right)}{\Delta_i} \text{ for sand parcel}$$
$$w_i = \frac{\frac{1}{h_i^2}\max\left(0, \vec{q}_w \cdot \vec{d}_i\right)}{\Delta_i} \text{ for mud parcel} \tag{4.12}$$

And routing probabilities are:

$$p_i = \frac{w_i}{\sum_{nb=1}^{8} w_{nb}}, i = 1,2..8 \tag{4.13}$$

<u>The rate of deposition and erosion:</u>

Sediment parcels are routed sequentially in a weighted random walk fashion according to the probabilities calculated with equation (4.12) and (4.13). The change to the bed topography is obtained by the exchange of sediment volume between the walking parcel and local bed at each cell along the path – during deposition a sediment parcel loses part of its volume and this volume is added to the bed, during erosion it's the opposite. We use simple phenomenological rules to decide (i) where deposition or erosion happens and (ii) how much volume should be exchanged between the sediment parcel and the bed. The rules for sand and mud parcels are different.

For the convenience of description, we refer to the initial volume of each sediment parcel V_{p_sed} as the "reference sediment parcel volume", and the remaining volume during the walking process of a sediment parcel as the "residual sediment parcel volume", V_{p_res}. The amount of deposition at each cell by an individual parcel is referred to as V_{p_dep}. The amount of erosion at each cell by an individual parcel is referred to as V_{p_ero}. Detailed rules are as following:

For the deposition from a sand parcel we do the following:

- At each cell in the domain, we calculate a "transport capacity" for sand flux (which can be seen as bed load flux), q_{s_cap}, as the maximum flux per unit width, which is a non-linear function of local flow velocity U_{loc}:

$$q_{s\_cap} = q_{s0} * \frac{U_{loc}^3}{U_0^3} \tag{4.14}$$

where q_{s0} is calculated by dividing the upstream sand flux input with inlet channel width:

$$q_{s0} = \frac{f_{sand} Q_{s0}}{N_0 \, \delta_c} \tag{4.15}$$

- Similar to the calculation of water discharge, as the sand parcels are routed sequentially, we track the accumulated total sand flux, q_{s_loc}, which increases with each visiting bed load parcel:

$$q'_{s\_loc} = q_{s\_loc} + \frac{V_{p\_res}}{\delta_c \Delta t} \tag{4.16}$$

- Deposition happens if a sand parcel visits a cell that has an accumulated local sand flux exceeding the transport capacity:

$$\begin{aligned} V_{p\_dep} &= V_{p\_res} \text{ if } q_{s\_loc} > q_{s\_cap} \\ V_{p\_dep} &= 0 \text{ if } q_{s\_loc} \le q_{s\_cap} \end{aligned} \tag{4.17}$$

For the deposition from a mud parcel we do the following:

- Deposition happens if a mud parcel visits a cell that has a local flow velocity U_{loc} smaller than a threshold velocity, U_{dep}. The amount of deposition is proportional to the residual sediment volume of the mud parcel as well as the relative difference between the squares of U_{loc} and U_{dep}:

$$\begin{aligned} V_{p\_dep} &= \lambda V_{p\_res} \frac{U_{dep}^2 - U_{loc}^2}{U_{dep}^2} \text{ if } U_{loc} < U_{dep} \\ V_{p\_dep} &= 0 \text{ if } U_{loc} \ge U_{dep} \end{aligned} \tag{4.17}$$

- λ is a “lag” coefficient that is set to 0.5 by default.
- U_{dep} is currently set to $U_{dep} = 0.3U_0$. The idea is that the finer grain size, the slower flow it requires to settle out.

For the erosion of both sediment parcels, we do the following:

- Erosion happens if local flow velocity magnitude is larger than a threshold value, U_{ero}, that differs for sand and mud parcels:

$$V_{p\_ero} = V_{p\_sed} \frac{U_{loc}^2 - U_{ero}^2}{U_{ero}^2} \quad \text{if} \quad U_{loc} > U_{ero}$$
$$V_{p\_ero} = 0 \quad \text{if} \quad U_{loc} \le U_{ero} \tag{4.18}$$

- For a sand parcel, $U_{ero} = 1.05U_0$.
- For a mud parcel, $U_{ero} = 1.5U_0$.

For volume exchange between sediment parcel and the bed:

- At each step, the volume of the sediment parcel will be updated as:

$$V'_{p\_res} = V_{p\_res} - V_{p\_dep} + V_{p\_ero} \tag{4.19}$$

- The elevation of the local bed will be updated as:

$$\eta' = \eta + \frac{V_{p\_dep}}{\delta_c^2} - \frac{V_{p\_ero}}{\delta_c^2} \tag{4.20}$$

- The local flow velocity and flow depth is updated accordingly with each event of deposition or erosion: $h' = H - \eta'$ and $\vec{u}' = \frac{\vec{q}_w}{h}$.

The reason for updating local flow depth and velocity immediately after each event of deposition and erosion is to avoid excess changes to the bed. Similarly we add an extra rule to control the rate of change to the bed by limiting the amount of deposition and erosion by a sediment parcel so that the change to local velocity magnitude is less than 25%. For example, if local flow depth is 4 meters, then the maximum deposition or erosion by a single sediment parcel is limited to 1 meter change to the bed.

After all sediment parcels finish their random walk, to take into account sediment flux that is diverted by topographical slope, we apply a topographic diffuser that assumes the diffusive flux is proportional to local sand (bed-load) flux and topographical slope:

$$q_{s\_diff} = \alpha |\nabla \eta| q_{s\_loc} \tag{4.21}$$

where α is a scaling coefficient, by default set to 0.1; $|\nabla \eta|$ is bed slope. The total change to the bed elevation by the topographic diffuser can be obtained by doing a flux balance at each cell over the time period of Δt.

Phase 4: update "routing direction"

Before moving to the next time step, we need to update the routing direction, a unit vector at each cell indicating the downstream direction for routing water parcels. At this last phase of the time step, at each cell we have the updated value of water unit discharge vector q, water surface elevation H, bed elevation η, water depth h, etc.

The same as Chapter 3, we consider two physical processes dictating the flow direction, (i) at an instant in time flow has a tendency to continue in the same direction as the direction at the previous instant – a process we call inertia, (ii) in the absence of any other drivers the flow will go down slope. Different from Chapter 3, where a global slope is applied for the specific planform model, in this model which has elevation as a variable in the vertical direction, we use an estimation of a local slope from the water surface gradient. We explain in detail below how to combine these two process and obtain a single vector as the local "routing direction".

First, we calculate a unit vector from the downstream direction based on the previous time step:

$$\vec{F}_{\text{int}} = \frac{\vec{q}_{w,old}}{|\vec{q}_{w,old}|} \tag{4.22}$$

Then, we calculate a unit vector from the water surface gradient (of previous time step):

$$\vec{F}_{sfc} = \frac{\nabla H_{old}}{|\nabla H_{old}|} \tag{4.23}$$

The same as in Chapter 3, we take a linear combination of the two vectors with a partitioning coefficient γ:

$$\vec{F}^* = \gamma\vec{F}_{sfc} + (1-\gamma)\vec{F}_{\text{int}}$$
$$\vec{F} = \frac{\vec{F}^*}{\left|\vec{F}^*\right|} \tag{4.24}$$

To arrive at a proper value of the partitioning coefficient γ, we adopt a Lagrangian view of flow movements that the downstream direction in the new time step is based on the downstream direction from the previous time step plus a correction due to gravity (in the form of water surface slope). Based on the 2-D shallow water momentum equation:

$$h\vec{u}\cdot\nabla\vec{u} = -gh\nabla H - C_f\vec{u}\left|\vec{u}\right| \tag{4.25}$$

If we ignore the friction term on the right hand side assuming only the water surface term contributes to changing flow direction, the relative change to the flow momentum per unit distance caused by gravity can be measured by: $\frac{gh\left|\nabla H\right|}{h\left|\vec{u}\right|^2}$. Therefore at a cellular scale, the value of γ can be obtained by solving the following equation:

$$\frac{\gamma}{1-\gamma} = \frac{g\left|\nabla H\right|\delta_c}{\left|\vec{u}\right|^2} \tag{4.26}$$

Substituting the surface slope $\left|\nabla H\right|$ with our reference slope S_0, and flow velocity $\left|\vec{u}\right|$ with the reference velocity U_0, we define a new variable, the "cellular Froude number", Fr_c:

$$Fr_c = \frac{U_0}{\sqrt{gS_0L_0}} \tag{4.27}$$

And γ is calculated by

$$\gamma = \frac{1}{1+Fr_c^2} \tag{4.28}$$

Essentially Fr_c measures the ratio between the inertia and the gravitational force at the cellular spatial scale.

4.4. Model results

In this section we show the power of this new model by presenting model results with varying input parameters. These parameters include:

(1) The portion of sand in the upstream sediment input, f_{sand};

(2) The scale of the physical setting, the reference flow velocity U_0, the reference flow depth h_0, and basin depth h_B;

(3) The reference slope, S_0.

Strictly speaking, the choice of the reference slope S_0 depends on the sand-mud ratio as well as the scale of the physical setting. In our model runs for field scale we use $3*10^{-4}$ on purely sandy deltas, $1*10^{-4}$ on purely muddy deltas and a linear combination of the two on mixture deltas; for laboratory scale we use values on the order of 10^{-2} (e.g., $1*10^{-2}$).

By varying f_{sand} we hope to see a transition between a typical sandy (coarse-grained) delta to a typical muddy (fine-grained) delta. By changing the scale of the physical setting of the model, we hope to see resultant deltas respond in systematic behaviors.

We select three sets of results to present in this section. The first set are field scale deltas with different sand/mud ratio. The second set is a fan-like delta produced by setting the model scales to laboratory basin experiments. The third set are field scale deltas with different basin depths.

Table 4-3. List of delta model runs and parameter values.

Run #	f_{sand}	S_0	U_0 (m/s)	h_0 (m)	h_B (m)
1	0.9	$2.8*10^{-4}$	1.0	5	5
2	0.5	$2.0*10^{-4}$	1.0	5	5
3	0.1	$1.2*10^{-4}$	1.0	5	5
4	0.3	$1.6*10^{-4}$	1.0	5	5
5	1.0	$1.0*10^{-2}$	0.3	0.02	0.02
6	0.3	$1.6*10^{-4}$	1.0	5	2.5
7	0.3	$1.6*10^{-4}$	1.0	5	10
8	1.0	$2.0*10^{-2}$	0.3	0.02	0.02

Shaded rows are laboratory scale; others are field scale.

4.4.1. Deltas built with a mixture of sand and mud

In this group, the domain is a lattice grid of 120 by 60 cells. Cell size is 50 meters. Channel inlet is 5 cells wide (250 meters), with a flow depth of 5 meters and a flow velocity of 1.0 m/s. The total water discharge is 1250 m^3/s. The total sediment discharge is 1.25 m^3/s. We use a time step size calculated from equation (4.3) that is 25000 seconds (~7 hours). Both water and sediment discharge stay constant and we assume they are at bankfull discharge.

We show three model runs in Figure 4-5 with the portion of sand in the upstream sediment discharge at 90%, 50%, and 10%.

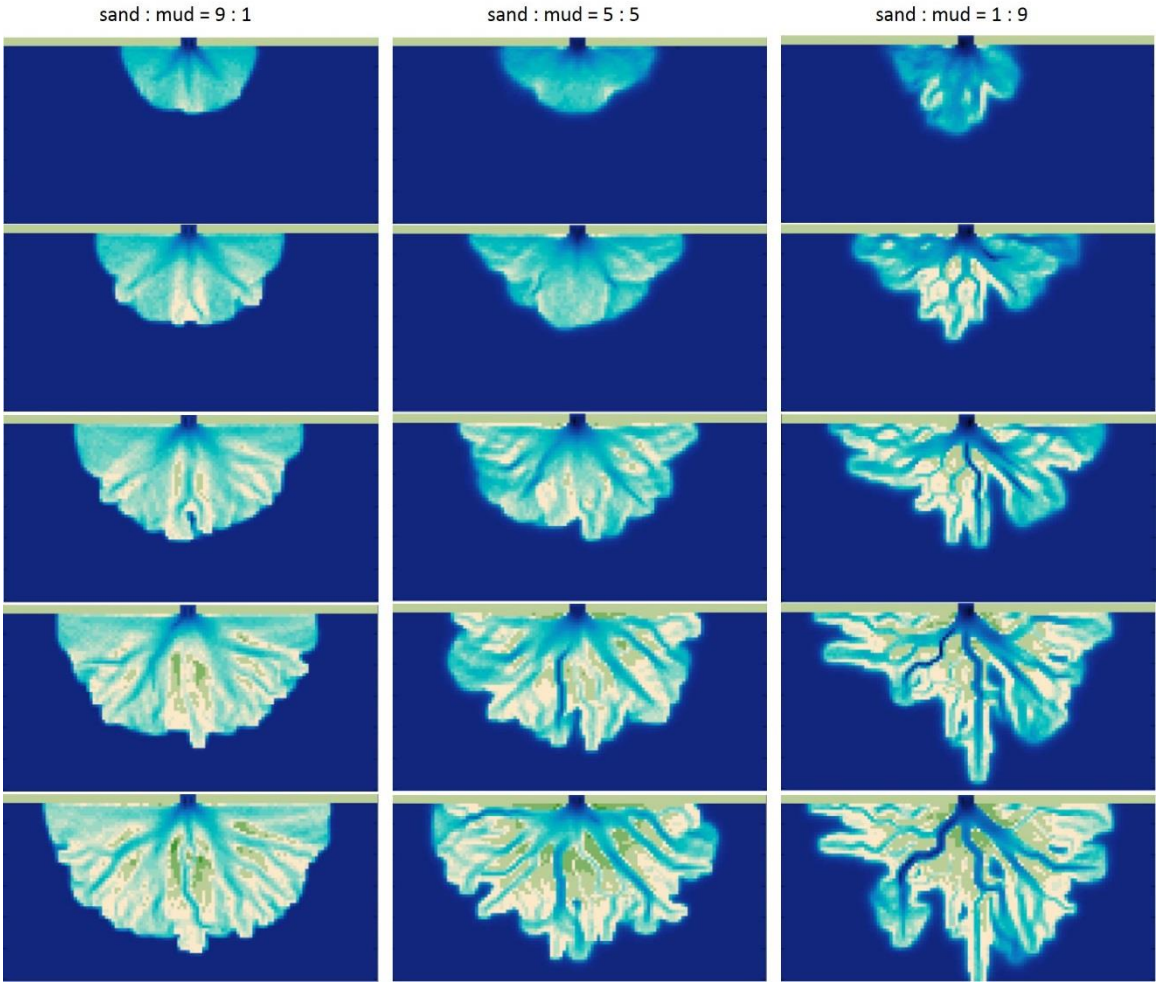

Figure 4-5. Time series of delta formation with different ratio of sand and mud flux (Run #1, #2 and #3). The color scheme shows bed elevation. Domain is about 3km by 6km. The time interval between rows is roughly 70 days (equivalent bankfull discharge time). Left column: deltas built with 90% sand and 10% mud. Center column: deltas built with 50% sand and 50% mud. Right column: deltas built with 10% sand and 90% mud.

The resultant deltas are different from run to run in the following characteristics:

- On a sandy delta the channels are relatively shallow and mobile, without well-defined levees. Flow is less confined. There are large areas of sheet flow. Shoreline is smooth and delta grows roughly in a semi-circular shape.

- On a muddy delta, channels are deeper and stable, with well-defined levees. Channel tends to elongate. Shoreline is rugose. Deltas built in different directions by switching lobes.

4.4.2. Deltas at different spatial and temporal scales

Laboratory experiments, numerical modeling and field observation are three important approaches of understanding the formation of deltas. We would like to test our model beyond field scale deltas, to model experimental deltas at laboratory settings. To do this, we change the domain to a lattice grid of 80 by 150 cells with a cell size of 0.02m. Inlet channel is still 5 cells wide but has flow depth of 0.02m and a flow velocity of 0.3m/s. Basin depth is 0.02m. Basically these are the settings for building an alluvial fan delta. The reference slope is set at 0.01. Time step is estimated at 33.3 seconds. Sediment input is considered to be coarse grain only.

In Figure 4-6 we show a time series of the resultant deltas. Note the displayed alluvial fan delta characteristics that a few active channels quickly switch around to build a semi-circular shape. To show the details of the channel switching process, we compare one switching event from our model results to the avulsion cycle described by Reitz and Jerolmack from the experimental fan delta (Reitz and Jerolmack, 2012). The model captures all the steps in the avulsion cycle (Figure 4-7 and Figure 4-8).

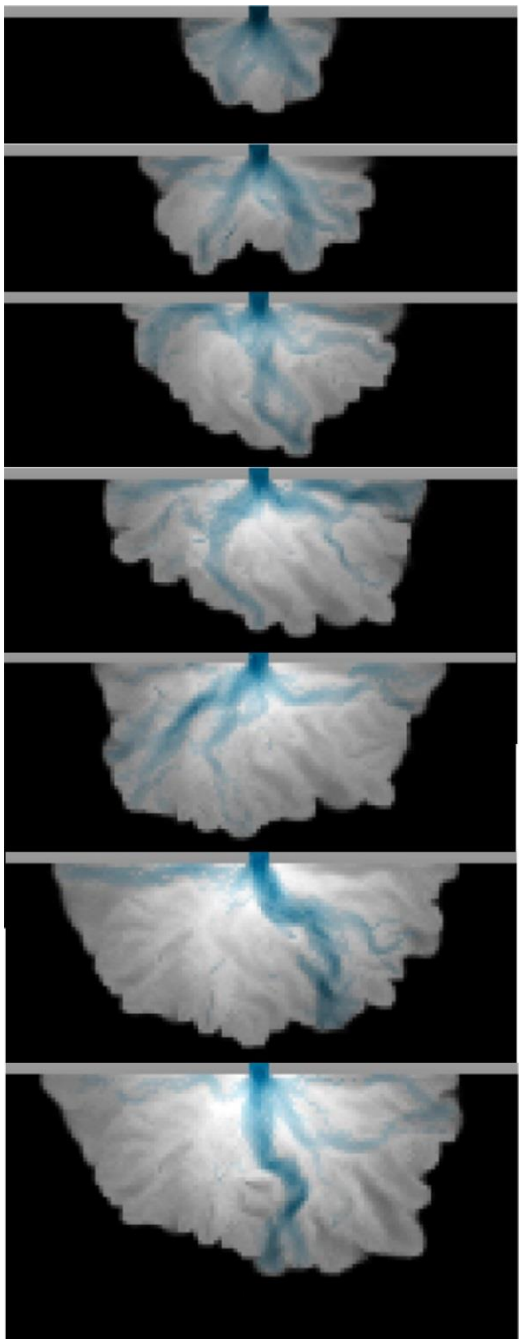

Figure 4-6. Time series snapshots of the delta produced by the model with laboratory setting. Active channel is marked by blue color overlay (more saturated blue means higher discharge) on a background grayscale image showing bed elevation (darker region has lower elevation).

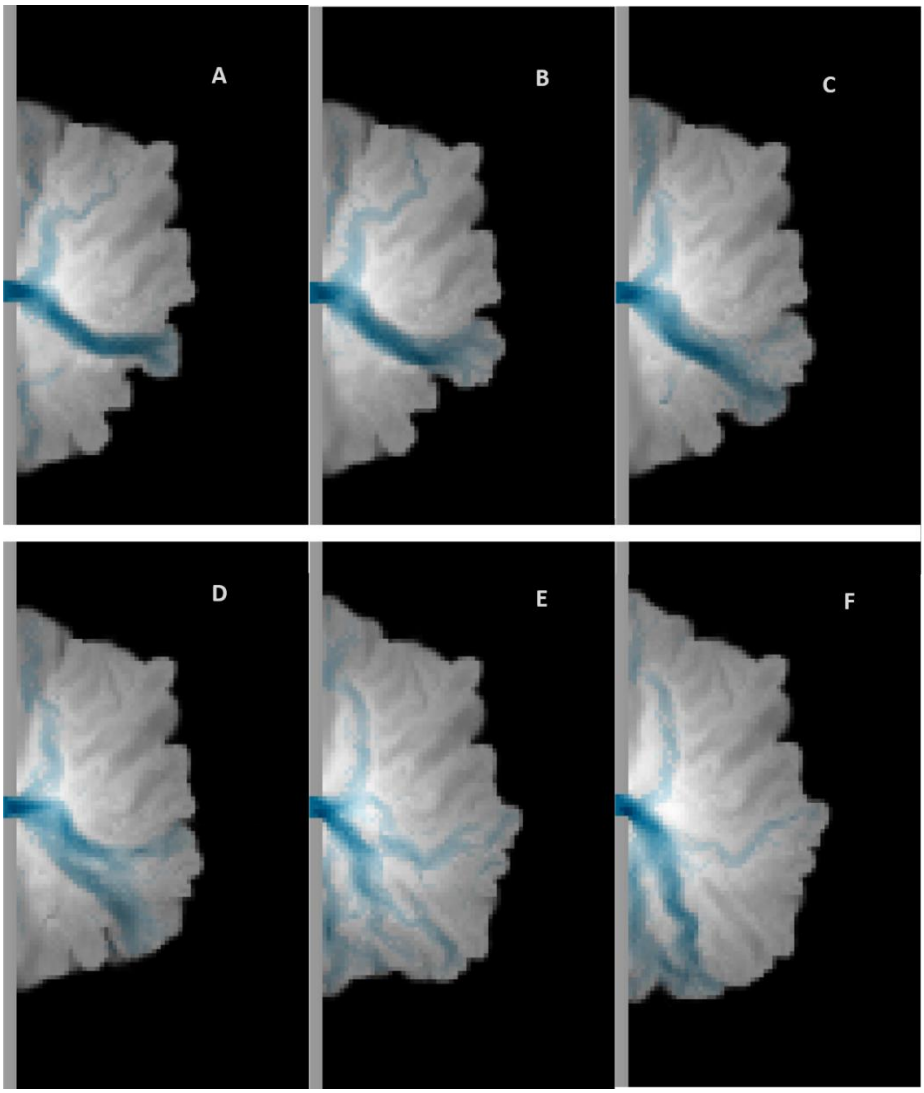

Figure 4-7. An avulsion cycle observed in our delta model results with laboratory-scale setting. Active channel is marked by blue color overlay (more saturated blue means higher discharge) on a background grayscale image showing bed elevation (darker region has lower elevation). The series of images matches the avulsion cycles observed by Reitz and Jerolmack 2012: (A) strongly channelizes, (B) pushes out the shoreline, (C) flares out locally to establish a semi-circular lobe, (D) backfills, (E) floods, and (F) channelizes.

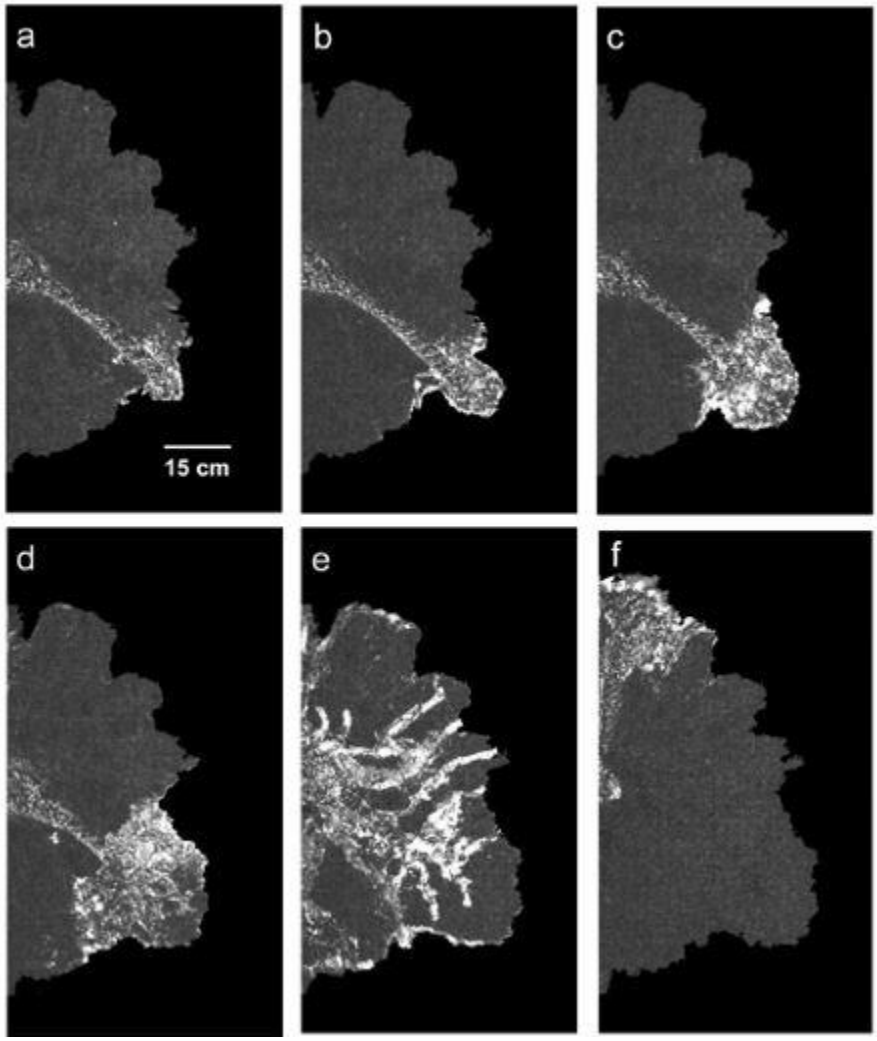

Figure 4-8. Avulsion cycle observed in laboratory fan experiments (Reitz & Jerolmack, 2012). Dark gray area is the coarse fan. White area is the location of water. They show that the system recursively (a) strongly channelizes, (b) pushes out the shoreline, (c) flares out locally to establish a semi-circular lobe, (d) backfills, (e) floods, and (f) channelizes.

4.4.3. Effects of relative basin depth

It has been well accepted that the accommodation space – the space that a delta can grow into – has an important role in the architecture and behaviors of a growing delta (e.g., Paola et al. 2000, Heller et al. 2001). However, towards the formation of river deltas in very low-Froude-number flow, it's still unclear how the depth of the basin affects the

overall morphology of the delta. Storms et al. (2007) uses Delft3D to model the initial delta formation from a river dominant effluent discharging constant flow and sediment loads into shallow and deep receiving basins under homopycnal conditions, and shows that the shallow basin delta is dominated by mouth bar bifurcations and a shoaling channel network, and exhibits significant stratigraphic complexity and sub-aerial development, while the deep basin delta is dominated by unstable bifurcations, levee breaches and avulsions (Storms et al. 2007). The authors suggested the shallow basin case resembles Wax Lake Delta. In our model run #6, #7, we test the same scenarios with exactly the same inlet channel conditions and discharge, but different basin depths. In run #6, the receiving basin is at half of the reference depth (defined by the inlet channel which is supposed to be at equilibrium state in terms of sediment transport), while in run #7, the receiving basin is at twice of the reference depth. In Figure 4-9 we show that our results give similar behaviors to the ones predicted by Storms et al. (2007). Furthermore, we would like to point out an interesting emergent feature from our model that has also been observed in the field of Wax Lake Delta by John Shaw and colleagues (John Shaw, PhD dissertation) (Figure 4-10).

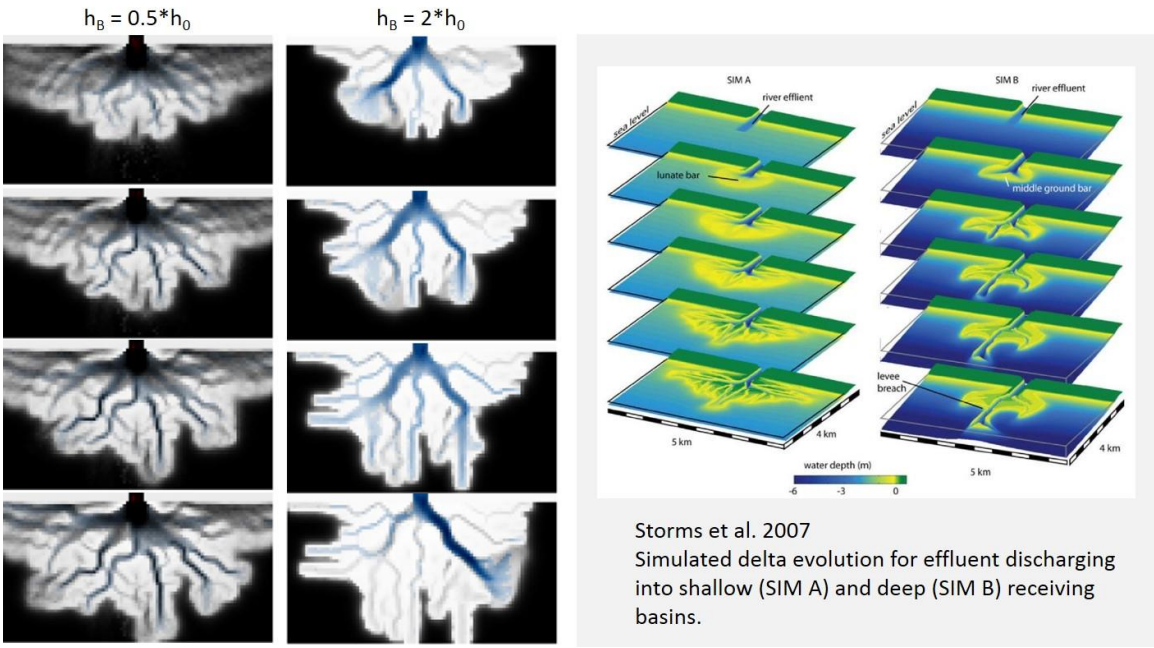

Figure 4-9. (Left side) Two model runs (run #6 and #7) with different basin depth and everything else the same. (Right side) Delft3D simulations by Storms et al. (2007). Both models predict similar morphological behaviors.

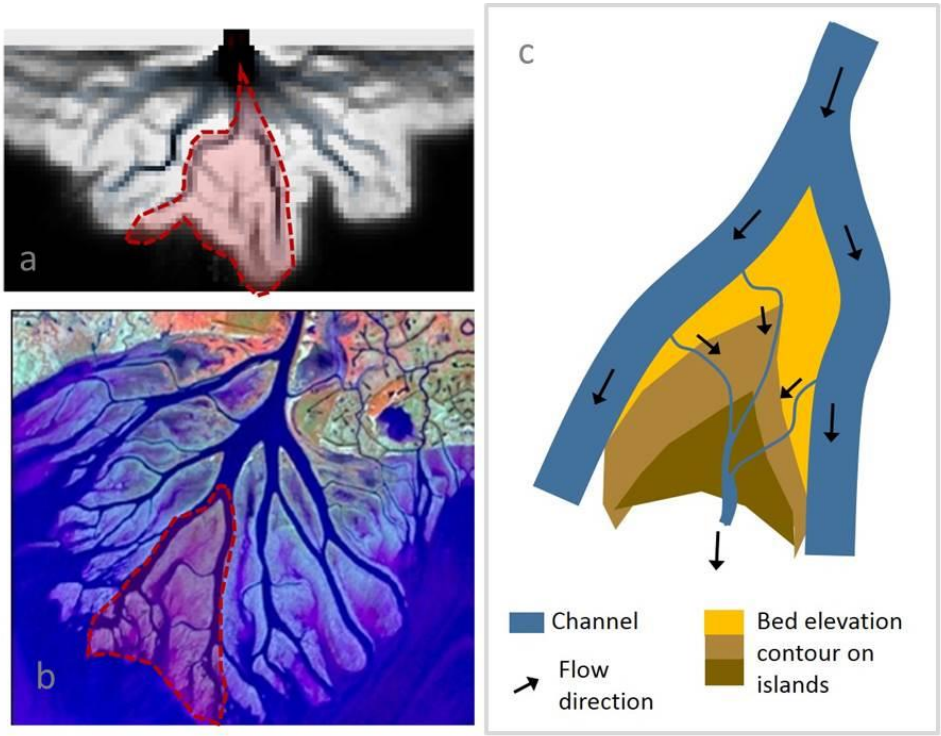

Figure 4-10. Flow features on the island of a delta formed in a shallow basin. (a) Model result from Run #6, where basin depth (2.5 meters) is only half of the inlet channel depth (5 meters); (b) Wax Lake Delta, where basin depth (<5 meters) is much less than the inlet channel depth (>20 meters); (c) schematic drawing showing the "tributary" flow feature on the island (Shaw et al., in preparation) observed both in the field (John Shaw, PhD dissertation) and in our numerical model results.

This "tributary" sub-network on islands (high-lighted in Figure 4-10) collects flow both from tie channels directly connected to the main channel network and from sheet flow topping the levees into the islands. Whether this sub-network is erosional or depositional, Shaw points out that at least they are not exactly favorable for deposition. In our model results, we notice the following feature that might explain the situation:

(1) The sub-network mainly collects fine sediment from the main channel network, which requires much slower flow to settle out;

(2) As the tributary sub-network joins into bigger trunk channels, the ability of the flow to carry sediment increases;

(3) At the downstream end of the network, where the trunk channel meets the open water, sediment deposit the same way as a normal delta lobe.

The difference between a shallow and deep receiving basin, according to our model results, is that:

- Channels will still try to maintain the same unit power of transporting sediment by maintaining a certain cross-sectional geometry with levees on the side and erosion or deposition on the bottom;
- In general a distributary channel network shoals up and channels are stable at shallower depth going seaward. With a shallow basin the amount of work is reduced. Also the narrow space promotes the splitting of flow which enhances the growth of a distributary network;
- A deep basin increases the time scale of establishing a stable channel, therefore introduces a much harsher competition among channels by allowing larger difference to occur. The variation of flow depth in channels exceeds the variation of lengths of channels, causing a stronger instability.

4.5. Recording of stratigraphy

A delta writes its own autobiography by preserving deposited sediment underground. These sedimentary records, stratigraphy, opens a door to understand the past. Therefore, the ability to record stratigraphy in a delta formation model enables us to directly investigate the connection between surface and sub-surface processes. In this model, we explore two methods that track the stratigraphy of model produced deltas: the first method tracks the distribution of coarse and fine sediment by recording the percentage of sand in each deposition event; the second method tracks the age of the deposit by labeling each deposition event with the time that its sediment enters the domain from the inlet channel.

4.5.1. Distribution of coarse and fine sediment

Generally speaking, coarse sediment (sand) can be found in channel belts and mouth bars, while fine sediment (mud) can be found in distal regions such as the bottom set of the delta, or on the floodplain or in abandoned channels.

We take a sample run of a field scale delta and 30% sediment input (Run #4). In Figure 4-11, we show a stratigraphic slice in the dip direction along the center line of the inlet channel. In Figure 4-12, we show the time series of the stratigraphic slice in the strike direction about 20 cells (1km) away from the inlet channel.

In both figures white color in the stratigraphy is pure sandy deposits and dark blue is pure muddy deposits. A mix of sand and mud deposits is colored according to the fraction of sand, with whiter color meaning more sand.

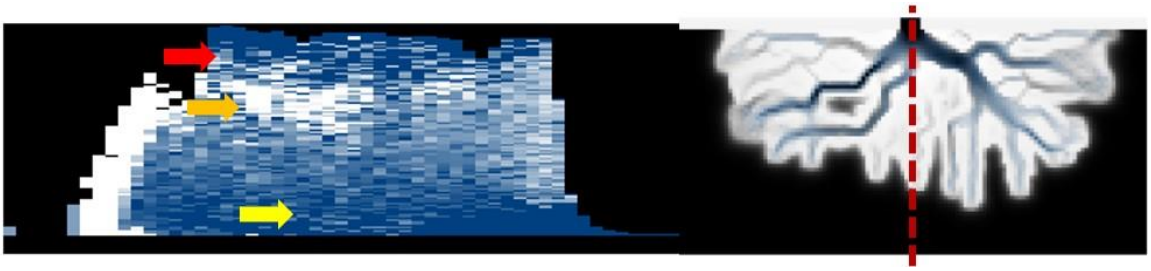

Figure 4-11. Stratigraphy slice in the dip direction of Run #4 (30% sand input). Note the layering of coarse and fine grains over time. Yellow arrow points to the bottom layer that accumulates fine grains at the bottom set of the delta; orange arrow points to the coarse grain layer deposited by channels that used to be active at that location; the two together shows the classic “coarsening-up” pattern in stratigraphy. The red arrow points to the fine grain deposited after the channels are abandoned.

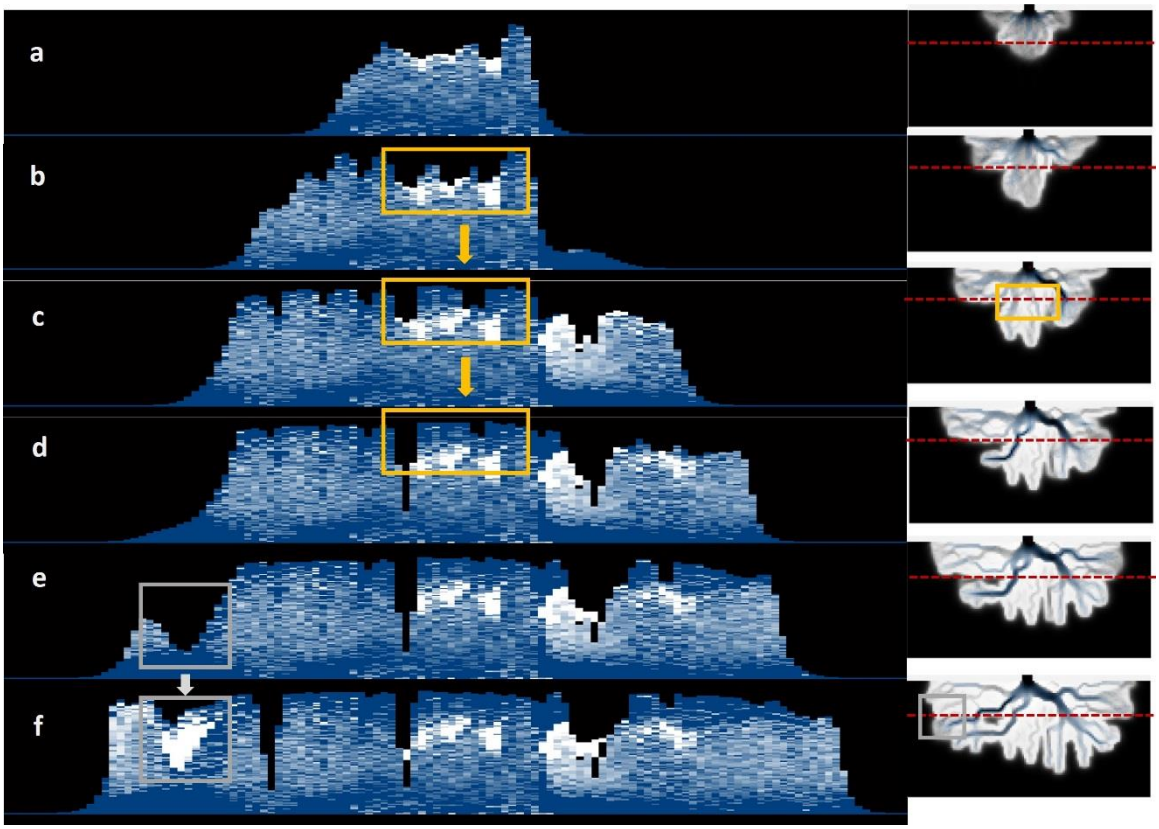

Figure 4-12. Time series of the stratigraphic slice in the strike direction about 20 cells (1km) away from the inlet channel. Note between (b) (c) and (d), in the yellow box, the abandoned channel belts are covered by muddy floodplain deposits. Also note between (e) and (f), in the light gray box, a mouth bar quickly deposits a significant amount of sand.

4.5.2. Distribution of deposition age

Although deposition age is usually difficult to observe either in the field (outcrops) or in laboratory settings, having the ability to record deposition age in stratigraphy is still an advantage for us to understand the connection between surface processes and subsurface architecture.

In Figure 4-13 we show a sample model run with the laboratory setting (Run #8). Note the evolution of the area that is pointed to by the yellow arrow. The series of images shows the deposition sequence from an individual avulsion event.

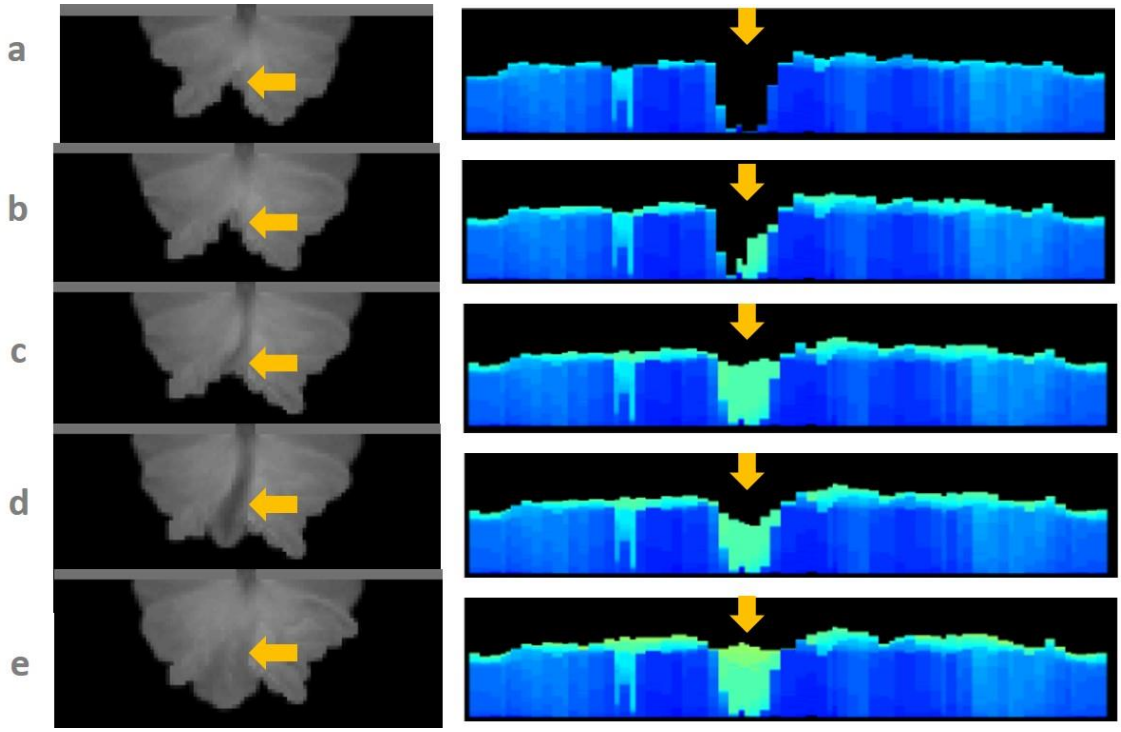

Figure 4-13. Time series of a delta produced by the model with laboratory scale and stratigraphy slices in the strike direction about 20 cells (0.4m) away from channel inlet. Note the evolution of the area that is pointed to by the yellow arrow. (a) a concaved shoreline – empty space in stratigraphy (b) channel begins to receive water and sediment – deposition begins (c) more water and sediment switch to the channel – space is filled up quickly (d) full avulsion completed – a channel is established by water digging into existing deposits (e) backfilling causes flooding and channel loses advantages – channel is filled back but there's a discontinuity in deposition age (yellowish green in upper portion and bluish green in lower portion).

4.6. Conclusions

In this chapter we extended the "weighted-random-walk" idea from Chapter 2 and Chapter 3 to build a delta formation model that resolves topography and a full range of channel dynamics, including elongation, bifurcation, avulsion, migration and lobe switching. In terms of system-scale behaviors, our model results are very close to those

produced from much higher complexity models (e.g. Delft3D), and some results resemble natural deltas very well.

Something to be noted is the computational time of this model. Our model runs presented in the result section took on average 3~4 hours for each of them, which can further be greatly reduced if the code is optimized in a more efficient way (currently everything is written in Matlab). The core of the code (without all the domain setup, value definition, etc.) is less than 400 lines.

What we would like to stress here, however, is not the computational advantage of our model – given that it is still a reduced-complexity model and is not designed to solve as much physical details as higher-complexity models like Delft3D. The best value of this model, in our point of view, is its flexibility coming from the rules of the model, such as the routing of flow according to inertia and slope, which allows people to immediately put their interpretation of the system into model behaviors and observe the difference in outcome. This is an excellent tool for hypothesis testing.

Currently we continue to work on two directions of future work:

(1) Adding new components to the model: so far what we have in mind are wave/tidal effects, and ecological processes such as vegetation and fish habitat distribution;
(2) Validation of existing model components: both flow and sediment routing schemes have parameter values that we don't fully understand, so our first step would be separating them as individual models and benchmark with higher-complexity models or field data.

We would also like to point out that the "weighted-random-walk" method is very closely related to the traditional cellular routing scheme with unit-discharge. In fact we see that routing of parcels with a probability field equivalent to a unit-discharge routing scheme that splits flow at each cell with the portions exactly equal to the routing probability vector at that cell, plus a random noise. It's still unclear what role this randomness plays in the final results and we need a quantitative test to explore it.

CHAPTER 5

EXPLORATORY MODELS

5.1. Introduction

Chapters 2, 3 and 4 are a summary of the outcome of a 6-year search for a Reduced-Complexity Model (RCM) framework for channel dynamics on river deltas. Apart from these results, we have also explored other forms of RCM prior to the final choice of using the "weighted random walk" method. Although the earlier attempts were abandoned on our path of exploration, these models have their own merits in terms of both modeling techniques and concepts that influenced the development of later models.

In this chapter, we give a brief description of the key ideas, construction and some representative results from the exploratory models. These models include: (1) analogical models utilizing computational methods developed for other diffusive transport systems that exhibit dendritic growth patterns, (2) a reduced hydrodynamic solver based on the shallow water equation under a low Froude number condition, and (3) a unit-discharge cellular routing scheme applied to model the morphology of river mouths.

5.2. Analogical models

Here we start by quoting the definition of "Analogical models" on Wikipedia:

"*Analogical models are a method of representing a phenomenon of the world, often called the 'target system' by another, more understandable or analyzable system. They are also called dynamical analogies. A simple type of analogy is one that is based on shared properties (Stanford Encyclopedia of Philosophy). Analogical models, also called "analog" or "analogue" models, therefore seek the analog systems that share properties with the target system as a means of representing the world. It is often practicable to construct source systems that are smaller and/or faster than the target systems so that*

one can deduce a priori knowledge of target system behavior. Analog devices are therefore those in which may differ in substance or structure but share properties of dynamic behavior. Dynamic analogies establish the analogies between electrical, mechanical, acoustical, magnetic and electronic systems."

Despite the poor understanding of the formation and dynamics of channels on a river delta, some other systems that also display a distributary dendritic pattern have been well studied with relatively mature simulation and analysis tools, such as the growth of dendrite crystals in an undercooled melt (Voller 2006). In this case, a solid seed is put into a bulk of undercooled melt, which introduces a negative temperature gradient from the surface of the solid seed into the liquid. The latent heat of the thin layer of liquid at the interface will be taken away by this negative gradient and the liquid solidify. The speed of growth is controlled by the magnitude of the gradient and some other factors (curvature, interface speed) (Voller, 2006; Voller, 2008). Given the similarity in the appearances between two systems, our questions are: (1) is there a deeper connection between the two systems in terms of the processes that govern the appearance and, (2) could the modeling technique for the better-understood system be applied to the other systems? To answer these questions, we build an analogical model using our understanding of dendrite crystal growth to approach the formation of channel network on river deltas.

5.2.1. Basic model: dendritic crystal growth in an undercooled melt

The foundation of the analogical model is the work by Voller (2008), in which an enthalpy method is applied to model dendritic growth in an undercooled binary alloy. Basically the method couples explicit difference solutions of equations expressing the conservation of enthalpy and solute to an iterative procedure that enforces node by node consistency between enthalpy, solute, liquid fraction, and interface under-cooling. In our analogical model, we further simplify the physical setting of the problem by ignoring

under-cooling effects, such as curvature under-cooling, solutal under-cooling, and kinetic undercooling. A detailed description of the setting of the problem and the numerical solver (Control Volume Finite Difference Method) for a general 1-D case is provided in Liang and Voller (2011).

For the purpose of understanding the formation of a dendritic structure, such as the characteristics of bifurcations, we explore the parameters that control the resultant shape of the dendrite. In the physical world, due to crystal anisotropy or other perturbations in the system, a perfectly circular seed will not grow evenly in all direction, instead, there will be preferred growth direction and primary arms will be aligned with these directions (Voller, 2008). In the numerical model with fixed grid, preferred growth directions can be introduced by controlling the "infection" process (Liang and Voller, 2011), which initiates the solidification process in the neighboring cells of a cell that has just solidified (the nodal liquid fraction of that cell increases to 1 in the latest time step). For example, on a lattice grid of square cells, each computational cell have eight neighboring cells, noted with directions, E, NE, N, NW, W, SW, S, and SE. By choosing the directions to be "infected" – to initiate the solidification process in a cell – different crystal shapes can be achieved. We explore four scenarios of infection on the structured grid: (1) all neighbors are infected; (2) only neighbors in the main compass directions (E, S, W, N) are infected; (3) only neighbors in diagonal directions (NE, NW, SE, SW) are infected; (4) each of the eight neighbors has a 50% chance to be infected, independently. The domain is a 201 by 201 lattice grid of square cells. Initially a seed of 1 by 1 cell is placed in the center of the domain (with equilibrium temperature and 50% liquid fraction).

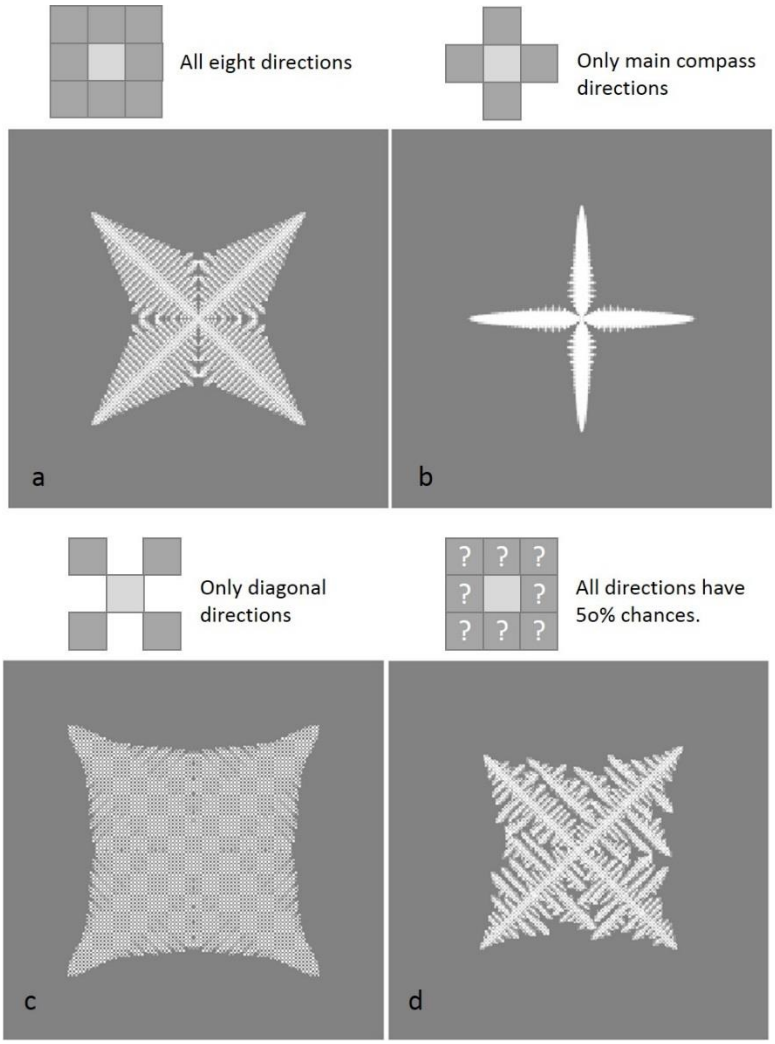

Figure 5-1. Simulated dendrite crystal patterns. A variety of shapes are achieved by choosing different preferred growth direction in the cellular rules for "infection". (a) all directions; (b) only the four main compass directions (E, S, W, N); (c) only the four diagonal directions (NE, NW, SE, SW); (d) a 50% chance for each direction.

To further test our hypothesis, we introduce an unstructured grid, which by nature brings irregularity in the interface and randomness in the direction of infection without arbitrary rules. The model uses an unstructured mesh of Delaunay triangulation in a square domain (Figure 5-2). Nodes are at vertexes of triangles. The control volume of each node is defined by a closed space with boundaries of straight lines connecting the center of

adjacent triangles. On this mesh we define “neighbors” of any given node *i* as the nodes that share a common side with node *i*:

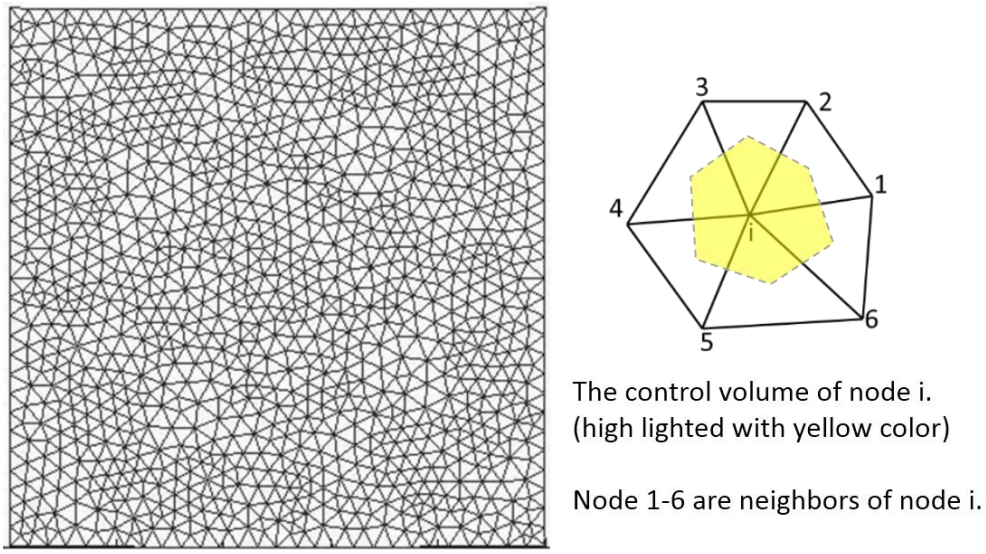

Figure 5-2. (Left) an example of the unstructured mesh generated with Delaunay triangulation. There are approximately 1000 nodes. (Right) an example of a control volume and neighbors.

Up to here, the exact mathematical framework for modeling dendrite crystal growth in undercooled melt can produce a network pattern that is qualitatively similar to the channel network on a river delta. In the following we extend the current framework by adding a few sets of cellular rules, to simulate sediment transport with channelization on river deltas.

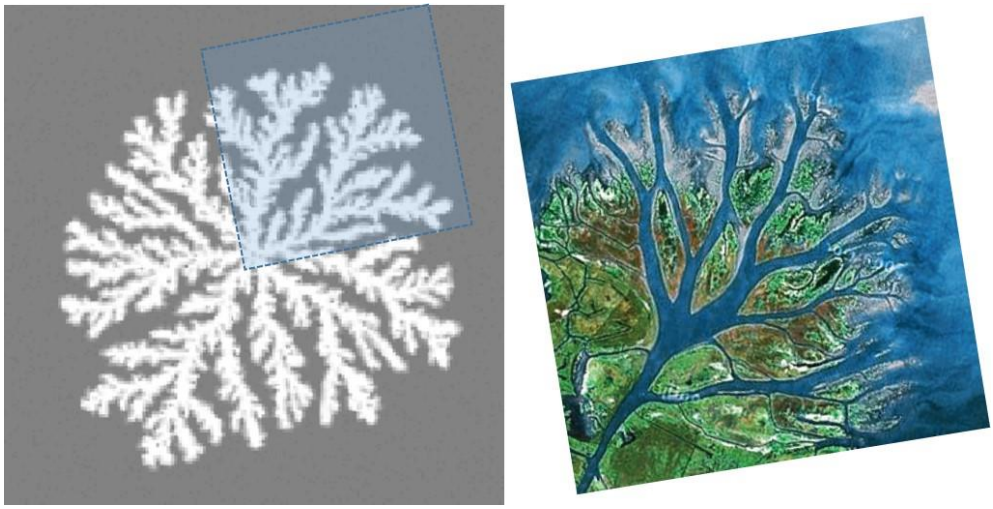

Figure 5-3. (Left) a dendrite crystal shape is generated on an unstructured grid with an initial seed located in the center of the square domain. There's no pre-defined preferred growth direction (infection applies to neighbors in all directions). Note the similarity between the highlighted region of the crystal and the channel network of Wax Lake Delta (on the right).

5.2.2. Modified model: the growth of channel network on river deltas

We use the same mathematical framework from the previous crystal growth model. A square domain is discretized by an unstructured mesh of Delaunay triangulation. The nodal values include:

(1) Potential h (with units of length), as an analogy to temperature T in the crystal growth model. It is defined as the elevation relative to a fixed datum (sea level). Initially (time $t = 0$), at each node i in the domain $h_i = h_0 < 0$. Sediment flux is proportional to the gradient of h. And h changes according to the imbalance of flux in the control volume, until reaches a fixed equilibrium value, $h_\Delta > 0$. Typically $h_0 = -1$ and $h_\Delta = 0.01$.

(2) Accumulative flow intensity ℓ (dimensionless), as an analogy to solid fraction (1-f) in the crystal growth model. At a given node i the value $0 \le l_i \le 1$, where 1 is the total amount of normalized flow intensity required to fully construct the

channel at node i; initially at every node $l_i = 0$. If a node i attains a value $l_i > 0$ during the simulation this indicates that a channel is forming ($0 < l_i < 1$) or has formed ($l_i = 1$).

With these two nodal values we design four types of nodes:

(1) An "ocean" node, identified by $h_0 < h_i < 0$, $l_i = 0$;

(2) A "floodplain" node identified by $0 < h_i < h_\Delta$, $l_i = 0$;

(3) A "channel" node identified by $h_i = h_\Delta$, $l_i = 1$;

(4) A "levee" node identified by $h_i = h_\Delta$, $l_i = 1$.

In the square domain, the inlet node is assigned at the lower left corner. The process is initiated by giving the inlet node a certain amount of flow intensity, $l_i = 0.5$. In each time step, the nodal values change during the simulation according to two set of rules: "building" rules and "aging" rules. Building rules are essentially equivalent to a Control Volume Finite Element solver of the governing equations, which is exactly the same as the crystal growth model. Aging rules are applied to the cellular structure of channel networks to regulate channel growth. The reason for bringing in this new set of aging rules is: if the process continues unchecked then some channels will out-compete others leading to "remnant" channels in the delta that remain static. In a physical setting it might be expected that these channels will fill in over a period of time and become part of the land. We deal with this situation by identification the remnant channel nodes that lost direct connection to the ocean and converting them to floodplain by lowering their flow intensity value l.

In Figure 5-4, we show one simulation result. Plots are taken at time steps 100, 300, 500 and 700. Domain has approximately 2000 nodes. Among the four node types, channel and ocean nodes are marked with blue color, levee and floodplain nodes are marked with green color.

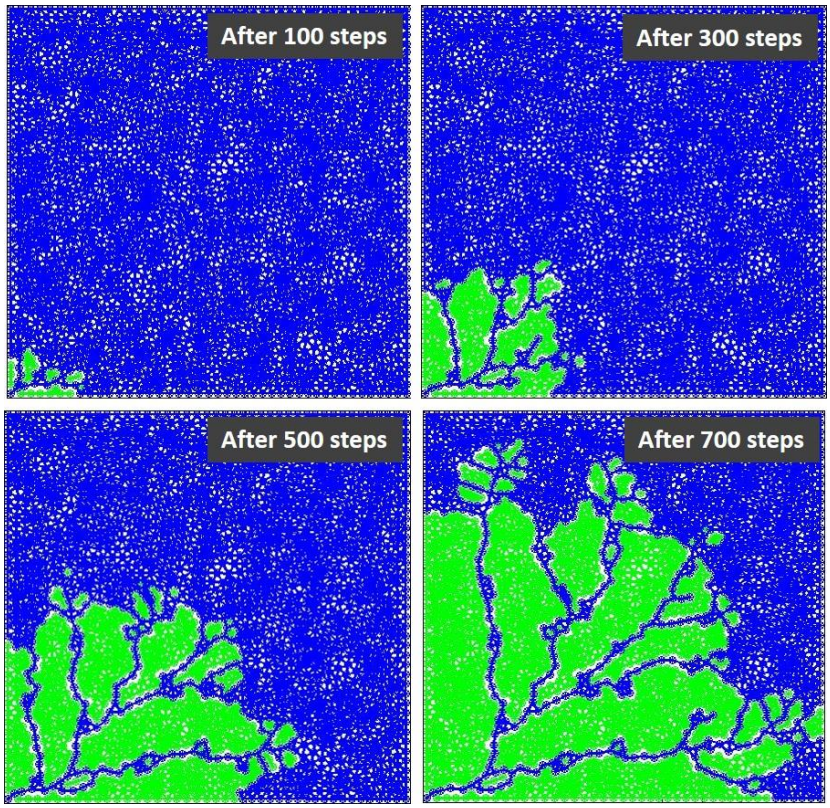

Figure 5-4. A time series of the simulation of delta channel network growth with an analogical model of dendrite crystal growth in undercooled melt. Note the formation of bifurcations, islands and the gradual abandonment of blocked channels. Other interesting features include lobe extensions along major channels.

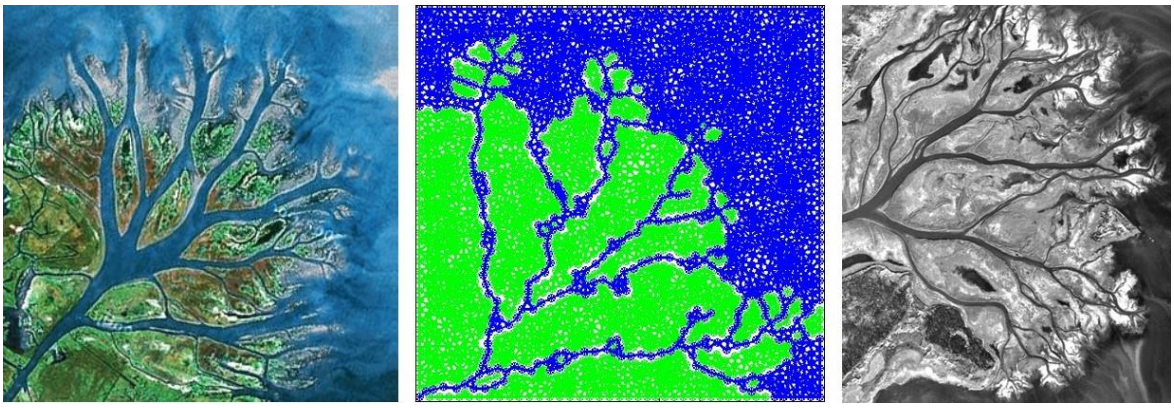

Figure 5-5. The model result (center image) compared to natural deltas with a bifurcation channel network, Wax Lake Delta in Louisiana, US (left image) and Mossy River Delta in Saskatchewan, Canada (right image).

To quantitatively study the similarity between the three images, we calculate the fractal dimension of the channel networks with the box-counting method. A river delta usually has a certain degree of self-similarity caused by the finer and finer structure created by the continuous process of bifurcations. An important measurement of this fractal structure is the box-counting dimension, also known as Minkowski-Bouligand dimension. The method works like this: put the fractal object over an evenly-spaced grid of square boxes (Figure 5-6), and count how many boxes contain part of the object of interest. For example, in this work we are interested in the channel network, so we count how many boxes contain channel nodes. The dimension is calculated by how this number changes as the size of the boxes becomes smaller. If $N(d)$ is the number of boxes containing the object of interest with a grid size of d, then the fractal dimension DIM is defined as:

$$DIM = \lim_{d \to 0} \frac{\log N(d)}{\log(1/d)} \tag{5.1}$$

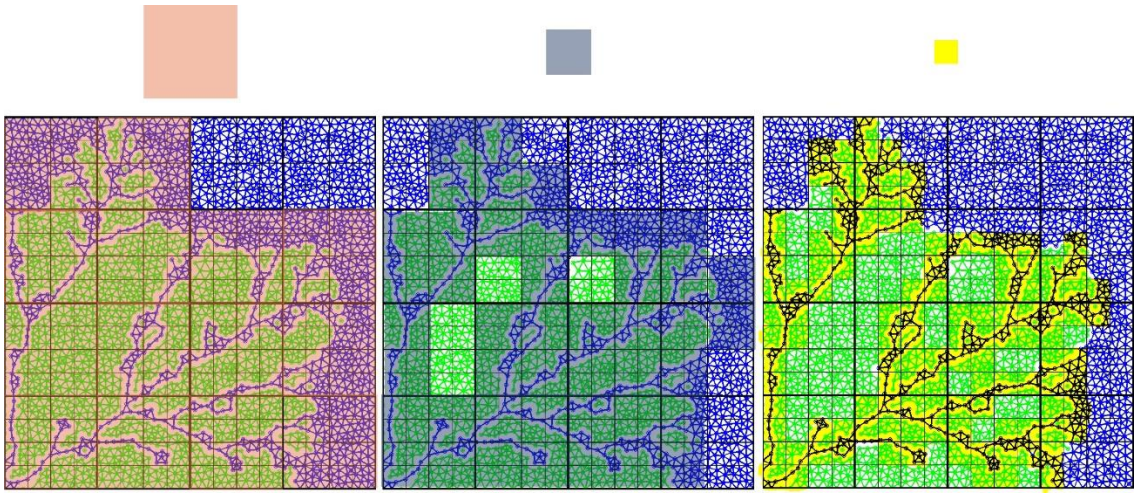

Figure 5-6. Illustration of a resultant channel pattern covered by three different sizes of the boxes using the box-counting method.

We use equation (5.1) with five box sizes on three model results and compare them to two natural deltas with clearly defined distributary channel networks: Mossy Delta and

Wax Lake Delta (data provided by Doug Edmonds). The images of model result #1, Mossy Delta and Wax Lake Delta can be found in Figure 5-5, and the images of model result #2 and #3 can be found in Figure 5-6.

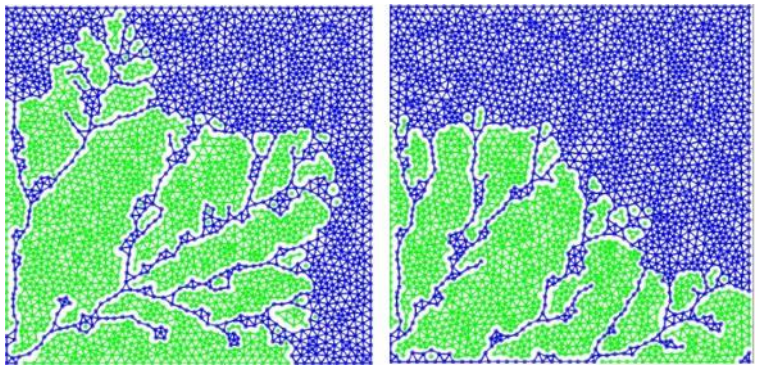

Figure 5-7. Patterns from model result #2 (left) and #3 (right). The difference in the results is caused by slightly different grid (e.g. number of cells and average size of the cells)

Table 5-1. A list of the fractal dimensions of the channel network patterns from the analogical model and from natural deltas.

Delta Network Pattern	Fractal Dimension
Model result #1	1.404
Model result #2	1.363
Model result #3	1.458
Mossy Delta	1.407
Wax Lake Delta	1.714

Shaded rows: the calculation for Mossy Delta and Wax Lake Delta is performed by Doug Edmonds.

We would like to point out two features from the results:

(1) Between the model results (#1, #2 and #3), there is a strong consistency that all three values are within 8% difference (1.363 to 1.458);

(2) Model results have an average fractal dimension (1.408) that is surprisingly close to the fractal dimension of Mossy Delta (1.407);

(3) The Wax Lake Delta has a much larger value (1.714) compared to all model results and Mossy Delta (all around 1.4).

The reason Wax Lake Delta is larger we think is that the surface area of water is much more significant compared to the whole area of the delta. This makes the channel network closer to a two-dimensional object.

5.3. Simplified hydrodynamic model

A major difficulty in constructing a morphodynamic model for the formation of river deltas is finding an efficient solution of fluid flow. Although it's not the primary approaches of RCMs, one option for designing an RCM is to explore simplified forms of the governing hydrodynamic equations, looking for the terms that matters more than others. In this case, we start with the shallow water equations. Here to obtain even more simplicity, and also to investigate the crucial terms, a solver is developed for flow with a low Froude number condition ($Fr^2 << 1$), which is common in natural river deltas. Our goal is to explore what details in the hydrodynamics can be left out and we hope to provide insights for designing a cellular routing scheme.

5.3.1. Flow solver for low-Froude-number shallow water

We start with the two-dimensional shallow water equations for mass and momentum conservation:

$$\nabla \cdot (h\vec{u}) = 0 \tag{5.2a}$$

$$h\vec{u} \cdot \nabla \vec{u} = -gh\nabla H - C_f |\vec{u}|\vec{u} \tag{5.2b}$$

where $\vec{u}$ is flow velocity vector, h is flow depth, H is water surface elevation, and C_f the coefficient of friction.

When the Froude number is small ($Fr^2 << 1$), the momentum equation (5.2b) reduces to the diffusive wave equation (Lal, 2008) by dropping out the change of inertia term on the left hand side and multiplying both sides with h^2,

$$0 = -gh^3 \nabla H - C_f |\vec{q}| \vec{q} \tag{5.3}$$

where flow unit discharge vector $\vec{q} = \vec{u}h$. Rearranging terms in equation (5.3) we get:

$$\vec{q} = \sqrt{\frac{gh}{C_f |\nabla H|}} h \nabla H . \tag{5.4}$$

As pointed out by Hajek and Wolinsky (2012), despite a relatively common application in large-scale engineering modeling (e.g. Lal et al., 2005), it's rare to see the diffusive wave equation applied to flow calculation in deltaic setting, such as avulsion modeling (Hajek & Wolinsky, 2012), except for the reduced-complexity model of Seybold et al. (2007, 2009), which uses unity as a constant diffusivity, rather than the term in equation (5.4), $\sqrt{\frac{gh}{C_f |\nabla H|}}$.

Combining equation (5.4) and (5.2a) and rearranging terms, the new equation to solve is:

$$\nabla \cdot \left(\sqrt{\frac{gh}{C_f |\nabla (h+\eta)|}} h \nabla (h+\eta) \right) = 0 \tag{5.5}$$

considering flow depth h as the only independent variable. Bed topography η is given for the whole domain (assuming there is no morphodynamic changes).

In order to solve equation (5.5) numerically, we propose a new method that takes a different form of (5.5):

$$\nabla \cdot \left(\frac{g}{C_f |\vec{q}|} h^3 \nabla h + \frac{g}{C_f |\vec{q}|} h^3 \nabla \eta \right) = 0 \tag{5.6}$$

Define a different diffusivity:

$$K = \frac{g}{C_f |\vec{q}|} \tag{5.7}$$

and a new variable

$$\psi = \int_0^h \alpha^3 d\alpha \tag{5.8}$$

so that these relationships hold: $\psi = \frac{h^4}{4}$, $h = (4\psi)^{1/4}$, $\nabla \psi = h^3 \nabla h$.

Equation (5.6) can then be written in the form of a nonlinear diffusion equation with a source term:

$$\nabla \cdot (K \nabla \psi + S) = 0 \tag{5.9}$$

where the source term is:

$$S = K(4\psi)^{3/4} \nabla \eta \tag{5.10}$$

and the diffusivity term is:

$$K = \frac{g}{C_f |\vec{q}|} = \frac{g}{C_f \sqrt{\left| \frac{g}{C_f} \nabla \psi + \frac{g}{C_f} (4\psi)^{3/4} \nabla \eta \right|}} \tag{5.11}$$

The equation system (5.9)-(5.11) is then solved numerically with a control volume finite element method over a discretized domain. The calculation starts with initial conditions of the following given values at each node in the domain: (1) bed elevation (η) – initial topology; (2) flow (ψ) – guessed value with boundary condition and (3) diffusivity (K) – guessed value.

5.3.2. Test: flow over bump

To test this new flow model, we design a “bump test”, which investigates how channel flow responds to a Gaussian-shaped obstacle on the bed (Figure 5-8). We are interested to know: will the flow accelerate over the bump or will it mainly split to the side and decelerate over the bump?

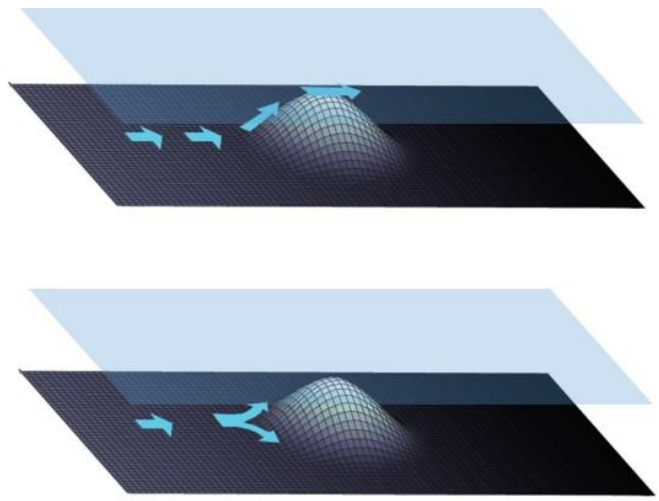

Figure 5-8. Illustration of the Gaussian-shaped bump on the bed of the channel. Upper and lower images show two types of flow behaviors we would like to see in model results: (upper image) flow accelerate over the bump, and (lower image) flow decelerate over the bump and mainly diverted around the bump.

This test is inspired by the work on the mechanics of river mouth-bar formation by Edmonds and Slingerland (2007). With a coupled hydrodynamic and morphodynamic model (Delft3D) they show how the flow velocity over the bar increases when height of bar is small and decrease as the bar grows higher (depth over bar is less than 40% reference depth) (Figure 5-9), which is the transition from flow accelerating over the bar to cause bar growth and flow decelerating over the bar to form bifurcations around the bar (Edmonds & Slingerland, 2007). Here what we are interested to know is whether the simplified flow model (equation (5.9)-(5.11)) based on the diffusive-wave approximation of the shallow water equations is capable to produce the same behavior, which is critical

for the formation of channel bifurcation – a basic ingredient for building a distributary channel network on a delta.

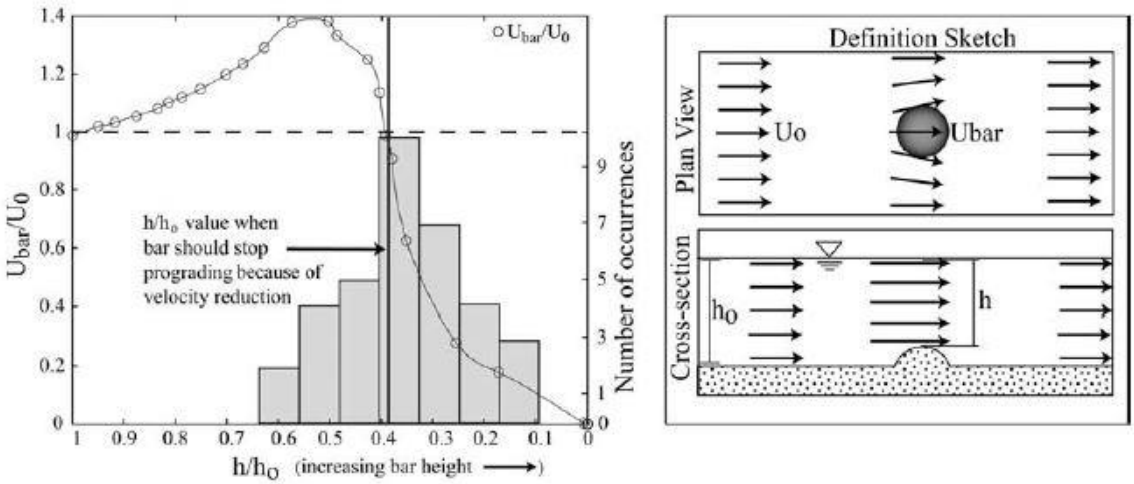

Figure 5-9. Centerline velocity over a fixed river mouth bar as a function of depth over bar relative to inlet depth (from Edmonds and Slingerland, 2007).

The domain is rectangular, representing a 200 meter reach of a 100 meter wide channel. The channel bed has a constant slope $S = 0.0025$ and a constant coefficient of friction $C_f = 0.1$. Note that this is an arbitrary value which is larger than the common range, 0.01~0.001. The upstream inlet has a constant flow rate of 50 m^3/sec and the downstream condition is a fixed water surface elevation of 1m. These settings give normal flow if the bed is flat. Now a Gaussian-shaped bump is superimposed on the flat bed, in the center of the domain with a radius about one third of the channel width. In our test, we vary the height of the bump from 10% to 99% of the normal flow water depth. For each bump height we run the simplified flow model and Delft3D (by Doug Edmonds) and compare the resolved flow field, with a focus on the velocity over the top of the bump. Results from three heights (20%, 60% and 90%) are shown in Figure 5-10.

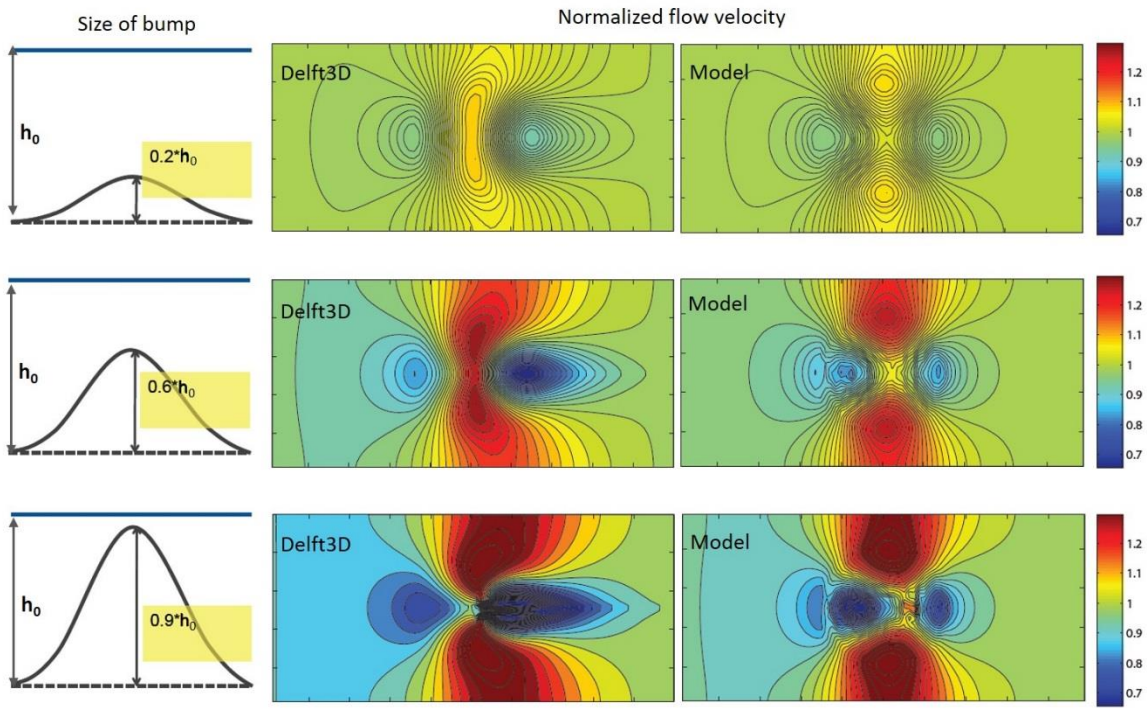

Figure 5-10. Normalized flow velocity contour plot for three normalized bump sizes (0.2, 0.6, 0.9). Results from Delft3D and from the new solver are compared side by side. Note the symmetric and diffusive behavior of the new solver. (Delft3D results by Doug Edmonds)

The difference between the results from Delft3D and our simplified hydrodynamic model is: (i) the flow field from the model is symmetric upstream and downstream of the bump, while Delft3D results show a clear skewness of the high velocity zone towards the downstream; (ii) the simplified hydrodynamic model is much more diffusive, that less flow "rushes" over the bump. Despite the significant quantitative difference, however, we would like to point out that in terms of the system behavior, both methods predicts a general trend of accelerating transitioning into decelerating as the bump grows higher (Figure 5-11). Also, both methods predict very close values of the critical bump heights for maximum velocity and the acceleration-deceleration transition (0.50/0.58 and 0.78/0.88) as marked in Figure 5-11. This is essential for designing a cellular flow routing scheme based on this simplified hydrodynamic model. In next section we give an example of a cellular routing model for mouth bar formation.

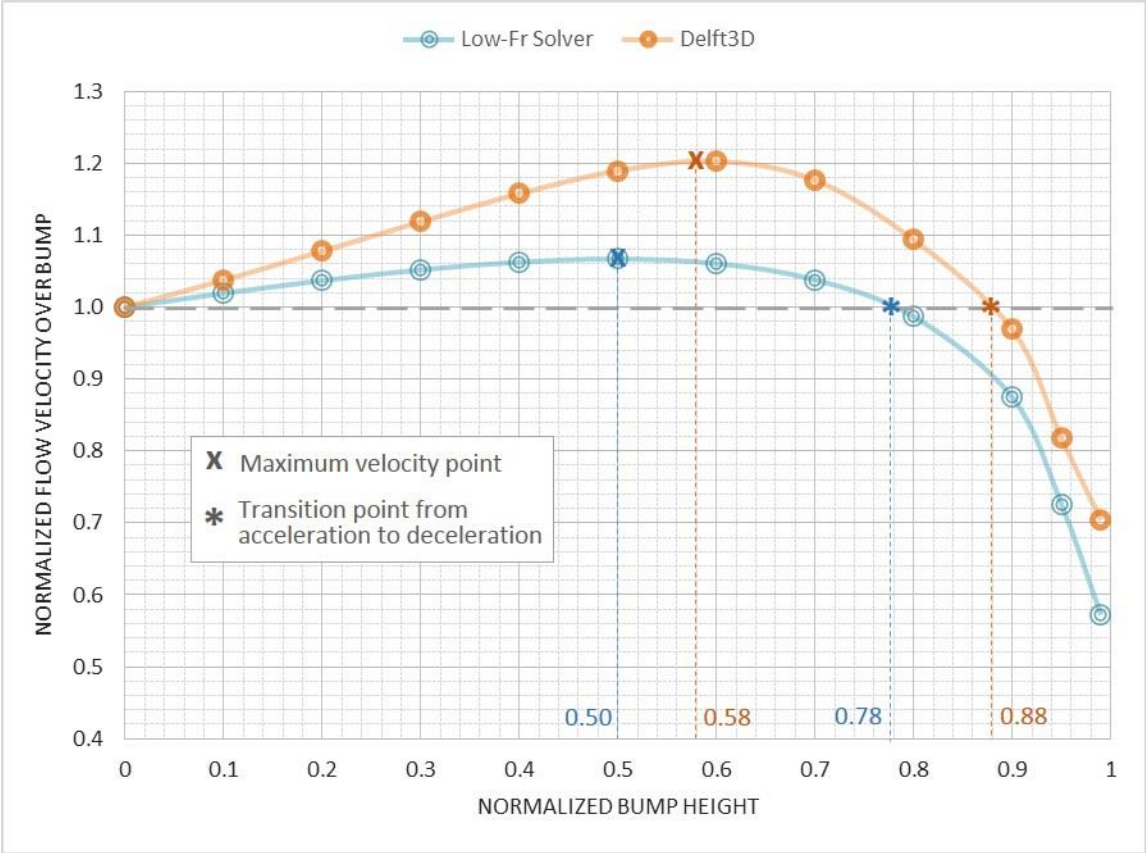

Figure 5-11. Comparison of flow velocities (normalized with a fixed upstream flow velocity) over the top of bumps with a range of heights (normalized by a fixed upstream flow depth). (Delft3D results by Doug Edmonds)

5.4. A preliminary cellular routing scheme for river mouth-bar formation

Cellular routing models did not receive significant attention among geomorphologists until the work by Murray and Paola (1994) on braided rivers. Since then newer models have been developed with new features and applied to a wider range of topics in the field of geomorphodynamics, such as eolian dunes (Werner 1995), river avulsions (Jerolmack & Paola, 2007), alluvial fans (Coulthard et al., 2002), meandering rivers (Coulthard & Van De Wiel, 2006), free bars in channels (Nicholas, 2010), delta formation (Seybold et al., 2007), coastline evolution (Ashton et al., 2001). Encouraged by the results from the

simplified hydrodynamic solver in the previous section, we would like to add to this family by designing a cellular routing model for river mouth-bar formation.

Recall in Section 5.3. the diffusive wave form of the shallow water equations under the low-Froude-number (referred to as "low-Fr" in the following) condition has the following relationship between flow unit discharge and flow depth:

$$|\vec{q}| = \sqrt{\frac{g}{C_f} h^3 |\nabla(h+\eta)|} \tag{5.12}$$

where h is flow depth and η is bed elevation. The significance of equation (5.12) is that flow rate can be locally determined by flow depth and bed topography only. Another factor which is an advantage for designing cellular models is that low-Fr flow also exhibits a "rigid-lid" feature that water surface has a mild slope and is insensitive to the change of bed topography, so that the variation in flow depth is mainly accounted by the variation of bed elevation. This means that we can potentially update bed topography without updating water surface profile at the same time.

The cellular domain is a rectangular lattice grid of 800 by 1500 square cells. Each cell is able to transport water to three immediate neighbors ($i = 1,2,3$) in the downstream direction (defined as from left to right) (Figure 5-12). The portion of flow received by each of the three downstream neighbor cells, $\{w_i\} \quad i = 1,2,3$, is calculated from:

$$\begin{gathered} w_i \propto \sqrt{\frac{g}{C_f} \bar{h}_i^3 |\nabla(h+\eta)|_i} \qquad i = 1,2,3 \\ \sum_{i=1,2,3} w_i = 1 \end{gathered} \tag{5.13}$$

Initially all cells in the domain have a dimensionless depth of unity and water surface has a constant slope from left to right (currently set to 10^{-5}). Flow comes in with a dimensionless velocity of unity from a line of cells on the left boundary. The calculation is carried on row by row until the last row of cells on the right side boundary. Once the flow rate is calculated, flow velocity is determined at each cell by dividing the unit

discharge value with the local flow depth. The change to the bed topography can be calculated with the Exner equation which is the continuity equation of sediment:

$$\frac{\partial \eta}{\partial t} = \nabla \cdot q_s \tag{5.14}$$

and a simplified Engelund-Hansen equation for sediment flux:

$$q_s = \alpha u^5 \tag{5.15}$$

where coefficient α is set to 1 in this dimensionless model.

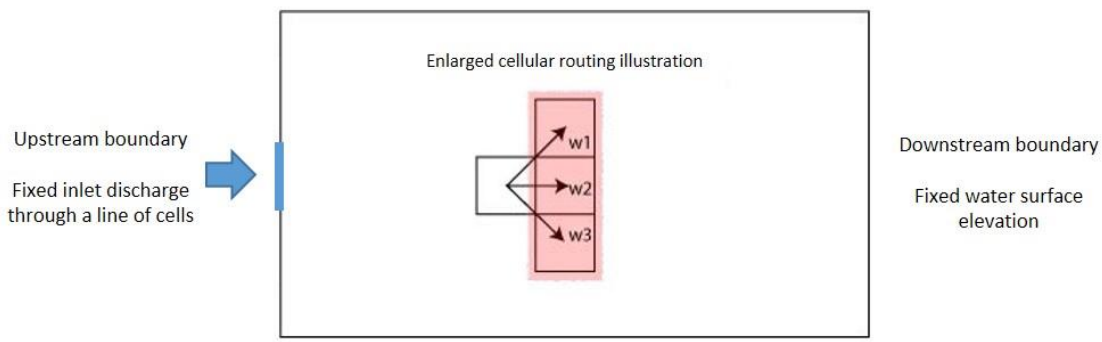

Figure 5-12. Illustration of the setting of the cellular model.

The results from this simple setting are shown in Figure 5-13, the color contour of bed topography. The model is able to predict the elongation by building subaqueous levees to confine the channel flow in the center. However, it doesn't show any trend to build a mouth bar. The reason is that with the simple three downstream neighbors routing scheme, the jet is not diffusive enough to deposit sediment at the front, especially with the effects of the levees formed along the sides. To improve this situation we add an artificial diffuser to the flow field after the routing in each time step, mimicking the lateral momentum transfer. This is also done by smoothing the calculated flow field in a row-by-row fashion:

$$q_{I,J}^{new} = 0.5q_{I,J} + 0.25q_{I,J-1} + 0.25q_{I,J+1} \tag{5.16}$$

where subscript (I, J) means the Ith row and J^{th} column. The strength of this diffuser is controlled by the number of times that equation (5.16) is applied in each time step, N_{diff}. By making N_{diff} a function of the normalized distance from the upstream inlet D/D_0, different spreading jets can be obtained (Figure 5-14).

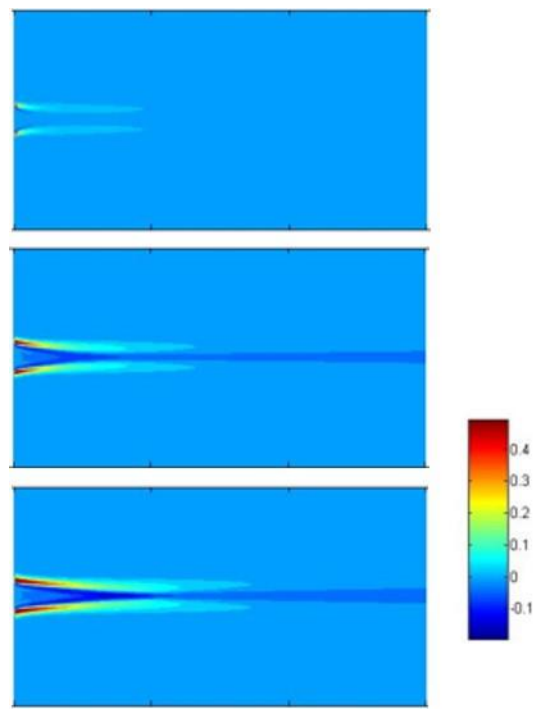

Figure 5-13. Subaqueous levees and channel elongation produced by the simple cellular routing scheme.

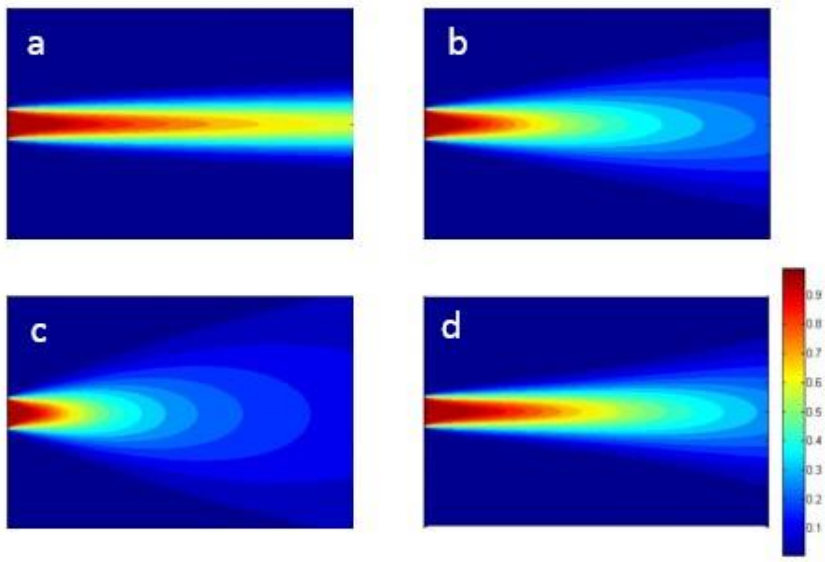

Figure 5-14. Flow velocity field produced by the simple cellular routing model scheme with a lateral diffuser. (a) no diffuser (b) a small constant $N_{diff} = 5$ (c) a larger constant $N_{diff} = 10$ (d) N_{smooth} as a linear function of distance from upstream inlet, $N_{diff} = 10\, D/D_0$.

We take the diffused jet flow in Figure 5-14(d) and redo the test in Figure 5-13. Now the results show subaqueous levees with channel elongation, as well as a mouth-bar at the front (Figure 5-15).

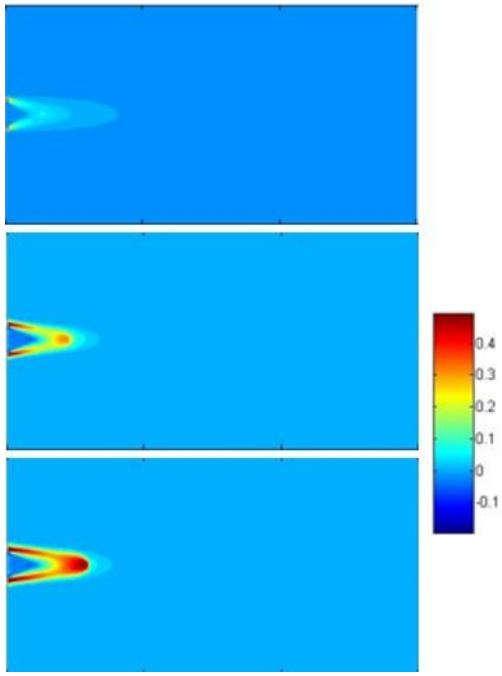

Figure 5-15. Levee formation, channel elongation, and mouth-bar formation with modified routing scheme (a linear lateral flow diffuser).

This is an encouraging result but the channel doesn't continue to bifurcate but keeps growing and pushes the mouth bar forward. We have the following hypothesis about why this happens and how to improve in the future:

- The simple "three downstream neighbor" scheme and a constant water surface gradient limit the change in flow direction, thus prevent substantial flow diversion (required for bifurcation) from happening;
- A flexible downstream flow direction and choice of receiving neighbors is the potential fix to the current problem.
- The diffusive profile of momentum in the jet needs to be improved, which may take advantage from more detailed models such as the potential vorticity theory (Falcini and Jerolmack, 2010).

5.5. Conclusions

In this chapter, we presented a few alternative RCMs for the formation of deltas with channel networks or for a key ingredient in growing a distributary network (mouth-bar induced flow diversion). As we stated in the introduction section, these models did not become a solid research line as the weighted-random-walk model in Chapters 2, 3 and 4, but we think they are useful models so we record them with details in this chapter.

The first model is the analogy between dendrite crystal growing in undercooled melt and the distributary channel network growth on deltas. It gives strikingly good comparison between model-simulated network pattern and natural deltas (Figure 5-5, Table 5-1). Despite the difference in the fundamental physical processes in these two distinct systems, here we would like to emphasize that dendritic patterns are so pervasive in nature, which makes it hard to believe there isn't any similarity in terms of the processes that create the patterns. Or in other words, the physics building the pattern may not depend on the details of the governing equations. This is something that worth looking further into, especially what controls the elongation and bifurcation of the branches. One potential future work is to connect with the Diffusion-Limited Aggregation (DLA) which also builds a fractal distributary network (Witten & Sander, 1981).

The second and third model are a simplified hydrodynamic solver for low-Fr shallow water equation (diffusive wave equation) and a preliminary cellular routing scheme designed based on the simplified hydrodynamic solver. The simple setup of models allows us to explore what information is critical to the system and what is not. A low-hanging fruit along this line would be a combination of our simplified hydrodynamic solver with the cellular structure of Seybold et al. (2007).

CHAPTER 6

FIXED AND DEFORMING GRID SOLUTIONS OF SOLIDIFICATION IN AN UNDERCOOLED MELT: A BENCHMARK PROBLEM

Published as: M. Liang & V. R. Voller (2011): Fixed and Deforming Grid Solutions of Solidification in an Undercooled Melt: A Benchmark Problem, Numerical Heat Transfer, Part B: Fundamentals, 60:1, 1-17.

A problem involving the solidification of a solid seed in an undercooled melt is posed. A sharp interface between solid and liquid is assumed and the equilibrium solidification temperature at this interface is controlled by both curvature and kinetic undercooling. Numerical solutions based on a fixed grid and on a deforming grid are developed. In the limits of a vanishing surface energy and large molecular mobility these solutions are verified by comparing with known analytical solutions. In general applications, with curvature and kinetic undercooling present, predictions from the fixed and deforming grid solutions are in close agreement. The results obtained highlight the role of the surface curvature and kinetic undercooling in controlling solidification speed and acceleration. In addition, both the fixed and deforming solution methods provide verification tools for more general 2-D and 3-D crystal growth simulations.

Although this work is focused on the thermal modeling of crystal growth, a significant motivation was to explore how undercooling thermal models could be adapted to model the formation of channels in sedimentary deltas.

Nomenclature:

c_l	Volumetric specific heat in the liquid phase (J/m^3-K)
c_s	Volumetric specific heat in the solid phase (J/m^3-K)
d_0	Capillary length (m)
ΔH	Volumetric enthalpy (J/m^3)
m	Domain dimension
n	Number of nodes in the domain
p	Index of node on solid/liquid interface
R	Solid/liquid interface position (m)
R_{seed}	Initial solid seed size (m)
T_{cur}	Curvature undercooling (K)
T_k	Kinetic undercooling (K)
T_{eq}	Equilibrium temperature at solid/liquid interface (K)
T_{in}	Initial bulk undercooling temperature (K)
T_m	Melting temperature (K)
T_{seed}	Initial seed temperature (K)
V	Speed of solid/liquid interface (m/s)
v	Grid speed (m/s)
α_l	Diffusivity in the liquid phase (m^2/s)
α_s	Diffusivity in the solid phase (m^2/s)
β_{cur}	Curvature undercooling coefficient (K·m)
β_k	Kinetic undercooling coefficient (K·s/m)
χ	Phenomenological model parameter
γ	Surface tension (N/m)
κ	Curvature (1/m)
μ	Kinetic mobility (m/s-K)

6.1. Introduction

Under appropriate conditions, when a solid spherical seed, at the equilibrium solidification temperature $T = T_{eq}$, is placed in a bulk undercooled liquid melt at temperature $T_{in} < T_{eq}$ the seed will solidify and grow. In a physical setting this growth will initially be unstable and due to anisotropy or noise the solid will exhibit a dendritic growth (Kurtz & Fisher, 1986). In contrast, in a mathematical setting, where noise and anisotropy can be eliminated, the initial seed will not form dendrites but retain a spherical shape as it grows. Under the limit conditions of no surface undercooling at the solid/liquid interface it is possible to arrive at analytical solutions of this mathematically enforced stable growth. Carslaw and Jaeger (1959) present similarity solutions for the solidification of a solid seed in a bulk undercooled pure melt in planar, cylindrical and spherical coordinates systems. In more recent work, under the limit condition that the Stefan number goes to zero (small specific heat compared to latent heat) Dantzig and Rappaz (2009) extend the cylindrical and spherical case of Carslaw and Jaeger (1959) to analytically account for cases that exhibit curvature undercooling of the surface of the growing seed. Further, Voller (2006, 2008, 2009), develops an analytical solution for planar (Voller 2006, 2008), cylindrical and spherical (Voller 2009) solidification of a seed in an undercooled binary alloy where solutal surface undercooling is accounted for. Although such analytical solutions lack the physical reality of unstable growth they do provide a sound benchmark for numerical solidification methods (Beckermann et al. 1999, Kim et al. 2000, Udaykumar et al. 2003, Pal et al. 2006, Voller 2008, Fabbri & Voller 1995, Voller and Cross 1981, Sethian 1996, Chatterjee 2010, Fang et al. 2009), This is particularly true for methods directed at modeling dendritic crystal growth processes in 2 and 3 dimensions (Beckermann et al. 1999, Kim et al. 2000, Udaykumar et al. 2003, Pal et al. 2006, Voller 2008); where—on artificially removing the physical anisotropy—the mathematical benchmark solutions can be used to access the level of artificial grid anisotropy in a given numerical approach. The full benchmarking utility of the analytical solutions in this application, however, is held back by their current inability

to generally accounting for curvature and kinetic undercooling at the growing solid surface.

In this paper solidification of a solid seed in an undercooled melt is examined. The main contribution is to show that if the axisymmetric nature of the problem is exploited, and care is taken, numerical solutions can be developed that retain stable growth of the seed. Further, unlike the current analytical solutions, these solutions can account for curvature and kinetic undercoolings, thereby leading to a wider class of benchmarks for general multi-dimensional solidification codes.

The work is laid out as follows. First a general axisymmetric problem is posed involving the growth of a spherical or cylindrical seed in an undercooled melt. This problem accounts for the undercooling of the growing solid surface due to curvature and kinetic effects. Numerical solutions based on both fixed (enthalpy) and deforming grids are developed. Previously, such numerical solutions have been developed for planar 1-D solidification (Fabbri & Voller 1995), where curvature undercooling does not occur. The authors are unaware, however, of solutions of this nature specifically developed to model axisymmetric cases accounting for both curvature and kinetic surface undercooling. The performance of the numerical models developed for this general case is initially compared with the limiting case analytical solutions presented in Carslaw and Jaeger (1959). Following this verification the numerical solutions are used to examine the relative roles of curvature and kinetics undercoolings in controlling the rate of solidification.

6.2. Governing equations

To derive appropriate governing equations we consider the growth of a solid seed, with initial size R_{seed} and initial temperature T_{seed}. This seed is placed in a liquid melt at a uniform bulk undercooled temperature $T_{in} < T_{seed} \leq T_m$ — the solidification temperature (K). It is assumed that noise and surface anisotropy can be neglected so that if the seed grows it will retain a cylindrical or spherical shape with a radius $R(t)$, see Figure 6-1.

Due to the curvature and speed of the growing surface $R(t)$ the equilibrium temperature of the solidification will be undercooled, i.e., the temperature at the solid/liquid interface on the surface of the seed is set by

$$T_{eq} = T_m - T_{cur} - T_k . \tag{6.1}$$

The second term on the right of (6.1)

$$T_{cur} = \frac{\gamma T_m}{\Delta H}\kappa = \beta_{cur}\kappa \tag{6.2}$$

is the undercooling due to the curvature $\kappa = 1/R$, where γ (N/m) is the surface tension, ΔH (J/m^3) is the volumetric enthalpy and through the remainder of this work the parameter $\beta_{cur} = \frac{\gamma T_m}{\Delta H}$ will be referred to as the curvature undercooling coefficient. The third term on the right of Eq. (6.1)

$$T_k = \frac{1}{\mu}\frac{dR}{dt} = \beta_k V \tag{6.3}$$

is the kinetic undercooling of the interface, where $\frac{dR}{dt} = V$ is the interface or growth speed, μ is kinetic mobility (m/s-K), and the parameter $\beta_k = \frac{1}{\mu}$ is referred to as the kinetic undercooling coefficient.

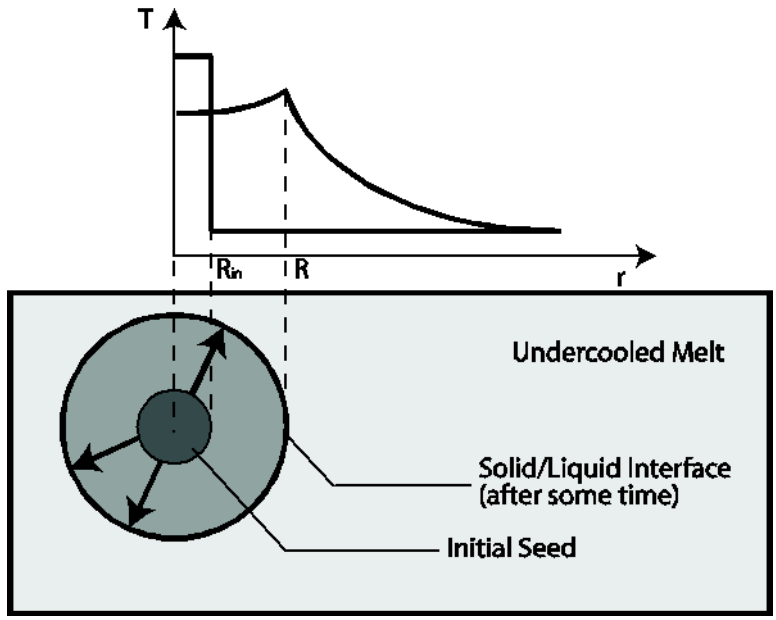

Figure 6-1. Illustration of the physical setting of the problem

If the initial seed radius in Figure 6-1 satisfies the condition

$$R_{seed} > \frac{\beta_{cur}}{T_m - T_{in}} \tag{6.4}$$

The solidification equilibrium temperature in Eq. (6.1) will be above the bulk liquid temperature and the seed will grow. The governing equations for this growth are as following.

Heat conduction in the solid

$$\frac{\partial T}{\partial t} = \frac{1}{r^m}\frac{\partial}{\partial r}\left(r^m \alpha_s \frac{\partial T}{\partial r}\right), \quad 0 < r < R(t), \tag{6.5}$$

with boundary conditions

$$\frac{dT}{dr} = 0 \text{ as } r \to 0 \text{ and } T = T_{eq} \text{ at } r = R(t). \tag{6.6}$$

Heat conduction in the liquid

$$\frac{\partial T}{\partial t} = \frac{1}{r^m}\frac{\partial}{\partial r}\left(r^m \alpha_l \frac{\partial T}{\partial r}\right), \qquad r > R(t), \tag{6.7}$$

With boundary conditions

$$T = T_{eq} \text{ at } r = R(t) \text{ and } T \to T_{in} < T_m \text{ as } r \to \infty. \tag{6.8}$$

In the above, α_s is the thermal diffusivity in solid phase and α_l is the thermal diffusivity in the liquid phase. Closure of Eq. (6.7) and Eq. (6.8) requires an additional condition at the solid/liquid interface to determine the growth speed, the Stefan condition

$$\Delta H \frac{dR}{dt} = -\alpha_l c_l \left.\frac{dT}{dr}\right|_{r=R(t)^+} + \alpha_s c_s \left.\frac{dT}{dr}\right|_{r=R(t)^-}, \tag{6.9}$$

where c_l is the volumetric specific heat in liquid phase and c_s is the volumetric specific heat in solid phase.

The domain of the problem is a one-dimensional semi-infinite slot (planar $m = 0$), wedge (cylindrical $m = 1$) or cone (spherical $m = 2$). Here for convenience of presentation we will assume that the seed is spherical which sets the exponent $m = 2$ in the above equations. Note, however, these equations and the following numerical developments can be really adapted for a cylindrical seed or plane front solidification on respectively setting the value of $m = 1$ or $m = 0$.

To arrive at a dimensionless form of governing equations, the following dimensionless numbers are introduced:

$$T^* = \frac{T - T_m}{\Delta H / c_l} \quad t^* = \frac{\alpha_l t}{d_0^2} \quad r^* = \frac{r}{d_0} \quad R^* = \frac{R}{d_0} \quad V^* = \frac{V d_0}{\alpha_l}$$
$$\kappa^* = d_0 \kappa \quad \beta_{cur}^* = \frac{\beta_{cur}/d_0}{\Delta H / c_l} \quad \beta_k^* = \frac{\alpha_l \beta_k / d_0}{\Delta H / c_l} \tag{6.10}$$

where the superscript (*) indicates a dimensionless quantity and d_0 is the capillary length.

From this point on only dimensionless quantities will be used and for clarity the * subscript will be dropped. In this way with the assumption of constant specific heats and the thermal diffusivities ($c_l = c_s$ and $\alpha_l = \alpha_s$) the dimensionless form of the governing equations are:

Heat transport in the solid,

$$\frac{\partial T}{\partial t} = \frac{1}{r^2}\frac{\partial}{\partial r}\left(r^2 \frac{\partial T}{\partial r}\right) \qquad 0 \le r < R(t), \tag{6.11}$$

with boundary conditions

$$\frac{dT}{dr} = 0 \text{ as } r \to 0\,,\ T = T_{eq} \text{ at } r = R(t) \tag{6.12}$$

Heat transport in the liquid,

$$\frac{\partial T}{\partial t} = \frac{1}{r^2}\frac{\partial}{\partial r}\left(r^2 \frac{\partial T}{\partial r}\right) \qquad r > R(t) \tag{6.13}$$

with boundary conditions

$$T = T_{eq} \text{ at } r = R(t),\ \ T \to T_{in} < T_m \text{ as } r \to \infty. \tag{6.14}$$

On the moving solid/liquid interface at $r = R(t)$, the Stefan condition is

$$V \equiv \frac{dR}{dt} = \left.\frac{dT}{dr}\right|_{r=R(t)^+} + \left.\frac{dT}{dr}\right|_{r=R(t)^-} \tag{6.15}$$

and the equilibrium temperatures is given by

$$T_{eq} = -\beta_{cur}\kappa - \beta_k V \tag{6.16}$$

6.3. Numerical solutions

In order to analyze the effects of curvature and interface speed in controlling the solidification rate, two numerical methods are developed, a fixed grid enthalpy method

and a deforming grid method. In these developments the focus is on the spherical case ($m = 2$) but both methods can be readily adapted to the planar and cylindrical case.

6.3.1. Fixed grid method (enthalpy method)

The volumetric enthalpy is defined as the sum of sensible and latent heats; in dimensionless form

$$H = T + f \tag{6.17}$$

where f is the liquid fraction. With the enthalpy a single domain governing equation can be constructed as

$$\frac{\partial H}{\partial t} = \frac{1}{r^2}\frac{\partial}{\partial r}\left(r^2 \frac{\partial T}{\partial r}\right), \quad r \geq 0 \tag{6.18}$$

In solving Eq. (6.18) a discrete domain of cell centered control volumes is used. Nodes are numbered $i = 1,...,n$, and the position of each node is given by the radius r (distance from the first node). Assuming a constant spacing, an explicit time integration of Eq. (6.18) leads to the control volume scheme

$$H_i^{new} = H_i + \frac{\Delta t}{r_i^2 \Delta r}\left(r_{i-\frac{1}{2}}^2 \frac{T_{i-1} - T_i}{\Delta r} + r_{i+\frac{1}{2}}^2 \frac{T_{i+1} - T_i}{\Delta r}\right) \tag{6.19}$$

Solidification is initiated by inserting a solid spherical seed with origin at node 1. The temperature of the seed is $0 \geq T_{seed} > T_{in}$ and its radius, chosen to meet the condition in (6.4), is set as an exact multiple of the discrete cell size, i.e., $R_{seed} = (p-1)\Delta r$. In this way, appropriate initial nodal settings are

$$f_i = \begin{cases} 0, & i < p \\ 0.5, & i = p \\ 1, & i > p \end{cases} \tag{6.20}$$

and,

$$T_i = \begin{cases} T_{eq,} & i \le p \\ T_{in} & i > p \end{cases} \tag{6.21}$$

The far field condition is met by fixing the node n temperature to $T_n = T_{in}$ and placing it at a distance where it has no significant influence on the solution.

At each step in the solution

1) An updated nodal enthalpy field H_i^{new} is obtained from (6.19).

2) To move forward to the next time step updated nodal liquid fraction and temperatures fields need to be extracted from these values. At nodes where the current liquid fraction $f_i = 0$ (in the solid) the updated nodal temperatures are given by $T_i^{new} = H_i^{new}$. At nodes where the current liquid fraction $f_i = 1$ (in the liquid) $T_i^{new} = H_i^{new} - 1$. At the unique node p where $0 < f_p < 1$ the relationship

$$H_p^{new} = T_{eq} + f_p^{new} \tag{6.22}$$

is used to update both the temperature and nodal liquid fraction. Using equation (6.22) requires a value of the current equilibrium temperature T_{eq} which by (6.16) requires approximations of the current interface curvature κ and growth speed V .

3) On assuming that the liquid fraction f_p can be used to track the position of the phase change across the control volume the value

$$R = [(p - .5) - f_p]\Delta r \tag{6.23}$$

provides a reasonable estimate of the current interface position. Hence an approximation of the curvature is given by

$$\kappa = \frac{1}{R} = \frac{1}{[(p - .5) - f_p]\Delta r} \tag{6.24}$$

4) On viewing the enthalpy method as a level set method (see appendix), the interface speed can be approximated by

$$V = \frac{\Delta r}{\Delta t}\left(f_p - f_p^{new}\right) \tag{6.25}$$

5) Using (6.24) and (6.25) in the expression (6.16) for the equilibrium temperature, a rearrangement of (6.22) results in the following explicit liquid fraction update

$$f_p^{new} = \max\left[0,\ \frac{H_p^{new} + \frac{\beta_{cur}}{R} + \beta_k \frac{\Delta r}{\Delta t} f_p}{1 + \beta_k \frac{\Delta r}{\Delta t}}\right] \tag{6.26}$$

6) Following (26) the corresponding nodal temperature given by

$$T_p^{new} = T_{eq} = H_p^{new} - f_p^{new} \tag{6.27}$$

The above procedures are sufficient to track the progress of the solidification through the pth control volume. Completion of the movement through the volume is signified when a value of $f_p^{new} = 0$ is returned by (6.26). In this case before calculations at the next time step are commenced the nodal liquid fraction in the cell $p+1$ is adjusted to $f_{p+1}^{new} = 0.99$. This step, referred to as "infection" ensures a progress of the solidification from one computational cell to the next.

6.3.2. Deforming grid method

The deforming grid method explicitly separates the solid and liquid domains and solves the problem statement (6.11) - (6.16). In the deforming grid solution the initial grid used is similar to the grid used in the fixed grid enthalpy solution where the initial solid seed has radius $R_{seed} = (p-1)\Delta r$. Here, however, as the solution evolves the grid deforms such that the original node p is always located on the growing solid seed interface. On this deforming grid, an implicit discrete heat balance, at a node removed from the interface (i.e., located in the full solid or full liquid) can be written as

$$\frac{\Delta r r_i^2 T_i - \Delta r^{old} r_i^{old^2} T_i^{old}}{\Delta t} = \left(r_{i-\frac{1}{2}}{}^2 \cdot \frac{T_{i-1} - T_i}{\Delta r} - r_{i+\frac{1}{2}}{}^2 \cdot \frac{T_i - T_{i+1}}{\Delta r} \right) + \left(v_{i+\frac{1}{2}} \cdot r_{i+\frac{1}{2}}{}^2 \cdot T_{i+\frac{1}{2}} - v_{i-\frac{1}{2}} \cdot r_{i-\frac{1}{2}}{}^2 \cdot T_{i-\frac{1}{2}} \right) \tag{6.28}$$

where un-superscripted values are at the current time level, cell interface quantities are averages of the neighbor node values, e.g., $\phi_{i+\frac{1}{2}} = \frac{\phi_{i+1} + \phi_i}{2}$, and v_i is the grid speed of node i. The first term on the right of (6.28) is the heat balance due to diffusion, and the second term is due to the grid advection. The appearance of the term $\Delta r^{old} r_i^{old^2}$ on the left hand side indicates that the heat balance needs to account for the change in the cell volume from one time step to the next. Equation (6.28) can be simplified by recognizing that the grid volume is conserved, i.e.,

$$\frac{\Delta r r_i^2 - \Delta r^{old} r_i^{old^2}}{\Delta t} = v_{i+\frac{1}{2}} r_{i+\frac{1}{2}}^2 - v_{i-\frac{1}{2}} r_{i-\frac{1}{2}}^2 \tag{6.29}$$

leading to the compact form

$$a_p T_i = a_p^0 T_i^{old} + a_e T_{i+1} + a_w T_{i-1} \tag{6.30}$$

with

$$a_w = \frac{r_{i-\frac{1}{2}}{}^2}{\Delta r} - \frac{r_{i-\frac{1}{2}}{}^2 \cdot v_{i-\frac{1}{2}}}{2}, \qquad a_e = \frac{r_{i+\frac{1}{2}}{}^2}{\Delta r} + \frac{r_{i+\frac{1}{2}}{}^2 \cdot v_{i+\frac{1}{2}}}{2},$$
$$a_p^0 = \frac{\Delta r^{old} \cdot r_i^{old^2}}{\Delta t}, \qquad a_p = a_p^0 + a_w + a_e \tag{6.31}$$

In operation (6.30) is solved in both the solid and the liquid domain. In the solid domain the equations are solved at node points 1 through $p-1$. Here $\Delta r = \Delta r_s = R/(p-1)$, and at node 1 $a_w = 0$ and $a_p^0 = (\Delta r_l^{old^3}/8)$. The liquid domain involved nodes $p+1$ through $n-1$, with $\Delta r = \Delta r_l = (R_n - R)/(n-p)$; the nth node has a fixed location R_n and temperature T_{in}.

Solution of the deforming grid scheme in one time step involves the following iterative procedure:

1) The first iteration is initiated by setting the current values to the old time step values.

2) On recognizing that at the front node p, $T_p = T_{eq}$, a second order discrete form of the Stefan condition (6.15) can be used to obtain the following equation for the solid/liquid interface speed

$$V = -\frac{-.5T_{p+2} + 2T_{p+1} - 1.5T_{eq}}{\Delta r_l} - \frac{-.5T_{p-2} + 2T_{p-1} - 1.5T_{eq}}{\Delta r_s} \tag{6.32}$$

This expression can be used in the definition (6.16) to provide a current approximation of the equilibrium temperature

$$T_{eq} = \frac{-\frac{\beta_{cur}}{r_P} - \beta_k\left(\frac{2T_{P+1} - .5T_{P+2}}{\Delta r_l} + \frac{2T_{p-1} - .5T_{P-2}}{\Delta r_s}\right)}{1 + \frac{1.5\beta_k}{\Delta r_l} + \frac{1.5\beta_k}{\Delta r_s}} \tag{6.33}$$

3) The estimate for the equilibrium temperature can be substituted back into (6.32) to obtain an estimate of the front speed and in turn an update of the seed radius

$$R = R^{old} + \Delta t V \tag{6.34}$$

4) This radius provides updates for the grid spacing

$$\begin{aligned} \Delta r_s &= \frac{R}{n-1} \\ \Delta r_l &= \frac{R_n - R}{n-p} \end{aligned} \tag{6.35}$$

nodal positions

$$r_i = \begin{cases} (i-1) * \Delta r_s, & i \le p \\ R + (i-p)\Delta r_i, & i > p \end{cases} \tag{6.36}$$

and grid velocities

$$v_i = \frac{r_i - r_i^{old}}{\Delta t} \tag{6.37}$$

5) Finally, with the settings (6.35)-(6.37), the coefficients in (6.31) can be calculated and the discrete equation (6.30) solved (e.g., via an inner iterative solver) for an updated temperature field.

Steps 1) - 5) are repeated until convergence occurring when the difference between two successive iterations (j and j+1) of R falls below a given tolerance; currently

$$\left| R^{j+1} - R^{j} \right| < \Delta t \cdot 10^{-6} \tag{6.38}$$

6.3.3. Numerical Considerations

In using the above schemes it is important to be aware of some operational issues and drawbacks.

1) Provided that condition (6.4) on the seed radius, R_{seed}, is satisfied growth will occur for any seed with an initial temperature $0 \geq T_{seed} > T_{in}$. The initial surface equilibrium temperature experienced by this seed will be a function of its initial curvature and the initial front speed. In the absence of kinetic undercooling $(\beta_k = 0)$ the initial seed temperature is set by the curvature $T_{seed} = -\beta_{cur} / R_{seed}$. When kinetic undercooling is present $(\beta_k > 0)$ a simplified treatment sets $T_{seed} = T_{in} + \varepsilon$, where $\varepsilon \sim 0.01$.

2) It is important to recognize that the strong coupling between the equilibrium temperature and the front speed in the deforming grid scheme, equation (6.33), is the key to an effective solution. Solutions can be achieved without this coupling but experience shows that without severe under-relaxation iterations are highly oscillatory.

3) The accuracy of the deforming grid can be improved by using the combination of the calculated speeds, at new time and previous time level, i.e., $V^* = \frac{V + V^{old}}{2}$, in the update of the seed radius in (6.34).

4) In keeping with the standard enthalpy method (Voller and Cross 1981), a plot of predictions at every time step of the fixed grid solver will show "jumps" in predictions as the phase front passes across the interface between two computational cells. Since the enthalpy fixed grid method is ultimately based on conserving the heat in the system, however, these discontinuities do not result in an accumulation of error as the process continues. In keeping with the arguments in Voller and Cross (1981) a smooth progress of the growth of the seed can be tracked by only extracting and storing values from the solution at the points in time where the interface cell liquid factions goes from $f_p^{old} < 0.5$ to $f_p \geq 0.5$, i.e., as the solid/liquid interfaces moves across node p. The lack of accumulation of error and robustness of the Voller –Cross method will be confirmed in the results below by demonstrating that the proposed fixed grid scheme recovers predictions in close agreement with the alternative deforming grid scheme and available analytical solutions.

6.4. Verification: comparison with analytical solution (similarity solution)

<u>No undercooling:</u> When both the kinetic and interface curvature effects are neglected, i.e. $T_{eq} = 0$, Carslaw and Jaeger (1959) derive a similarity solutions by assuming the interface position is proportional to the square root of time

$$R(t) = 2\lambda\sqrt{t} \tag{6.39a}$$

For a spherical seed λ is given by the root of

$$\lambda^2 e^{\lambda^2}\left(e^{-\lambda^2} - \lambda\pi^{\frac{1}{2}} erfc(\lambda)\right) - \frac{1}{2}\left(T_{eq} - T_{in}\right) = 0 \tag{6.39b}$$

The solid temperature is fixed at $T = 0$, and the liquid temperature

$$T = T_{in} + \frac{2\lambda\left(T_{eq} - T_{in}\right)}{e^{-\lambda^2} - \lambda\pi^{\frac{1}{2}} erfc(\lambda)}\left\{\frac{t^{\frac{1}{2}}}{r} e^{-\frac{r^2}{4t}} - \frac{\pi^{\frac{1}{2}}}{2} erfc\left(\frac{r}{2t^{\frac{1}{2}}}\right)\right\} \tag{6.40}$$

where the complimentary error function is

$$erfc(x) = 1 - erf(x) = \frac{2}{\sqrt{\pi}} \int_x^{\infty} e^{-t^2} dt \tag{6.41}$$

The problem of growth in the absence of surface undercooling has been solved using the fixed grid and deforming grid methods outlined above. In these calculations the dimensionless domain length is 100, the initial seed size is $R_{seed} = 0.2$, and the bulk undercooling temperature is $T_{in} = -0.5$. Following a grid study, results are reported using, in the fixed grid solver, a space grid of 1001 node points and a time step of 0.002. The deforming solver uses the same number of node points but, because of the implicit nature of the solution, it uses a larger time step, of 0.01. Comparison of the numerical predictions for the movement of the solid seed surface with the analytical solution, see Figure 6-2**,** indicates a good match; thereby verifying the soundness of the basic operation of both the proposed fixed and deforming grid numerical schemes.

<u>Undercooling</u>: In the most general case, the equilibrium temperature at the interface varies with its position and speed and in general the analytical solution presented above does not hold. A special case of surface undercooling, however, can be manufactured that will admit an analytical solution and allow for a more complete verification of the proposed schemes. If the following time varying values

$$\beta_{cur}^{v} = \psi_{cur}\sqrt{t}, \quad \beta_{k}^{v} = \psi_{k} R \tag{6.42}$$

where the ψ 's are constants, are used for the surface undercooling coefficients the equilibrium temperature will have the constant value

$$T_{eq} = -\frac{\psi_{cur}}{2\lambda} - \psi_k \cdot 2\lambda^2 \tag{6.43}$$

and the analytical solution (6.39)-(6.41) holds. This problem can be readily used to test the ability of the proposed schemes to handle kinetic and curvature undercoolings. This is achieved by withholding from the numerical schemes the information that the equilibrium temperature is a constant. In this way, the schemes operates as designed, with the varying values of the surface undercooling coefficients in (6.42) used with numerical estimated interface position and speed to determine the equilibrium temperature at each point in the solution. A test solution, using the previous grid and time steps , with the settings $\psi_{cur} = 0.2\lambda$ and $\psi_k = \frac{0.1}{2\lambda^2}$ ($T_{eq} = -0.2$), see Figure 6-3, clearly demonstrates that in tracking the growth of the spherical seed both the deforming and fixed grid solution can handle surface undercooling with no loss of accuracy.

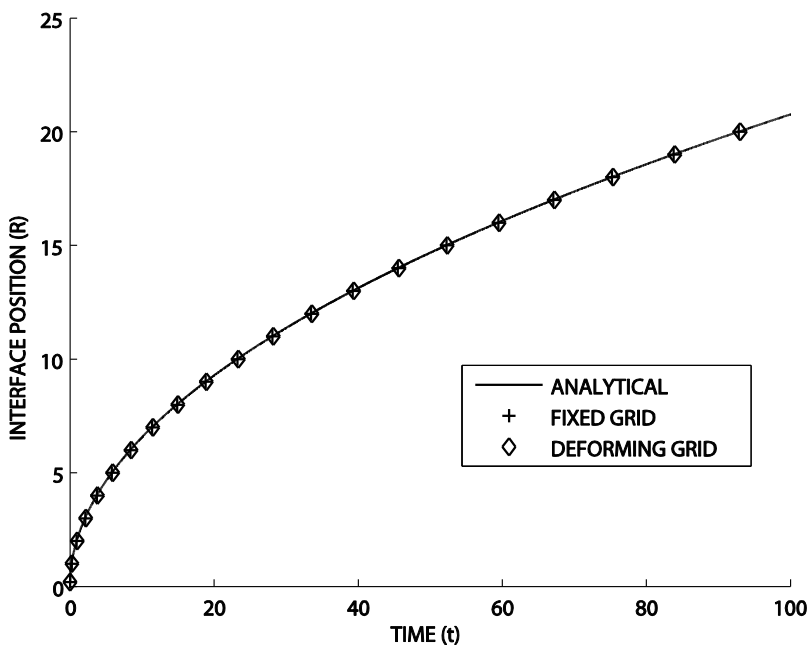

Figure 6-2. Comparison with analytical solution (with no undercooling)

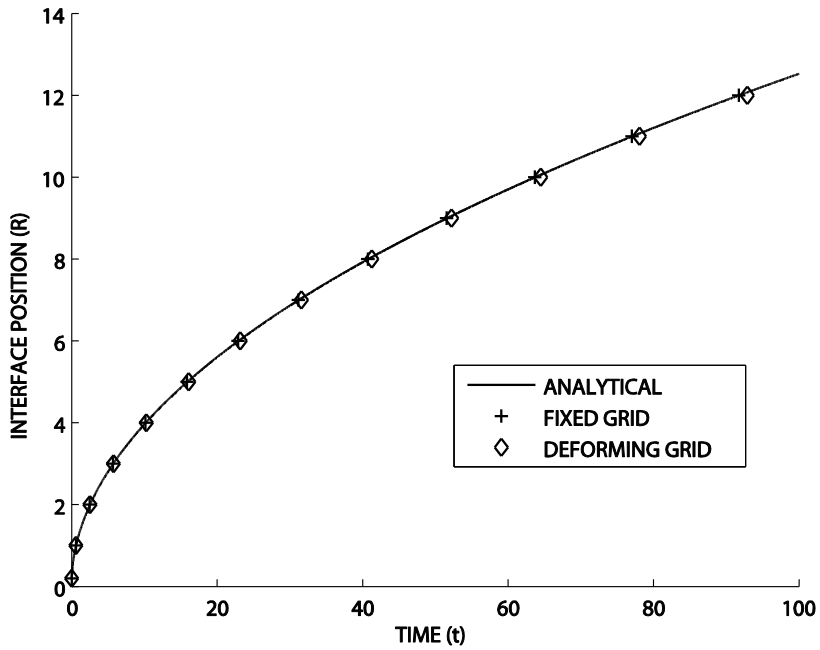

Figure 6-3. Comparison with analytical solution (with undercooling)

6.5. Results

Before the two proposed methods are tested on general undercooling problems where β_{cur} and β_k are arbitrary positive constants it is worthwhile to explore the roles of the curvature and kinetic surface undercoolings. Towards this end the following approximate phenomenological model for the behavior of the interface (growth) speed is suggested

$$\frac{dR}{dt} = \chi \frac{T_{eq} - T_{in}}{R[1 - e^{c(R_{seed} - R)}]} \tag{6.44}$$

where χ is a single positive constant. This is a reasonable approximate model of the growth behavior since it (i) accounts for the fact that the main driver of the solid growth is the temperature difference between the seed surface and bulk liquid $(T_{eq} - T_{in})$, (ii) at early times (when $R \approx R_{seed}$) this difference operates over a vanishingly small distance,

and (iii) as time increases it recovers the analytical square root of time dependence on the seed radius as $T_{eq} \rightarrow$ constant. On using (6.16) the model (6.44) can be written as

$$(R[1-e^{\chi(R_{seed}-R)}]+\chi\beta_k)\frac{dR}{dt}=-\chi\frac{\beta_{cur}}{R}-\chi T_{in} \tag{6.45}$$

This model clearly shows the role of the kinetic coefficient β_k in controlling the growth speed. A larger value of β_k will reduce the growth speed throughout the calculation. On differentiating (6.45) w.r.t. time the following expression for the growth acceleration is obtained

$$(R[1-e^{\chi(R_{seed}-R)}]+\chi\beta_k)\frac{d^2R}{dt^2}=\chi\frac{\beta_{cur}}{R^2}-\{e^{\chi(R_{seed}-R)}[\chi R-1]+1\}\frac{dR}{dt} \tag{6.46}$$

From (6.46) an important feature of the curvature coefficient is revealed. First note at early times ($R \approx R_{seed}$) the last term on the right of (6.46) will dominate and the seed growth will decelerate with time. Depending on the value of curvature coefficient β_{cur}, however, this deceleration can be reversed at later times. Once the initial transient has past and the term $e^{\chi(R_{seed}-R)}$ is small, a large enough curvature undercooling could result in a period of time over which the seed growth accelerates. A situation that will revert back to a deceleration once the seed radius becomes large enough, i.e., when $\chi\frac{\beta_{cur}}{R^2}<\frac{dR}{dt}$.

The above suggested behavior for the front speed is tested by using the proposed fixed and deforming grid numerical solutions. In these applications the domain length is 100, the initial seed size is $R_{seed}=5$ and the bulk under-cooling temperature is $T_{in}=-0.5$. Both fixed and deforming methods use 1001 node points. The fixed grid uses a time step of 0.002, and the deforming grid uses a time step of 0.01. Figure 6-4 shows interface speed predictions for three different combinations of β_{cur} and β_k. In these results the first thing to notice is the close agreement between the fixed and deforming grid predictions. In this case, since speed predictions represent a derivative of the front position, obtaining

a close match fully illustrates the consistency between the fixed and deforming grid predictions. Further, the results in Figure 6-4 also match the trends identified in the approximate behavioral model in (6.45) and (6.46). In the case that $\beta_{cur} = 1$ and $\beta_k = 1$ the speed dR/dt is always large enough to supersede any curvature induced acceleration (see right hand side of (6.46)) and the predicted front speed decreases monotonically. If the value of the kinetic coefficient is increased $\beta_{cur} = 1$ and $\beta_k = 2$, the form of the results is unchanged, the increased value of β_k simply reducing the growth speed. If, on the other hand, the value of the curvature undercooling coefficient is increased, $\beta_{cur} = 2$ and $\beta_k = 1$, the curvature induced acceleration (the term $c\frac{\beta_{cur}}{R^2}$ in (6.46)) is sufficiently large to allow for a period of acceleration prior to the long time deceleration behavior. This qualitative agreement between the behaviors predicted with the numerical and approximate model in (6.45) is reinforced by comparing the numerical and approximate growth speed predictions, see Figure 6-5. An exact match in Figure 6-5 should not be expected since the approximate model (6.45) does not explicitly account for evolving temperature profiles. Never the less, it is worth noting that the qualitative behavior of the approximate model does match the behavior of the numerical model for all choices of the undercooling coefficients.

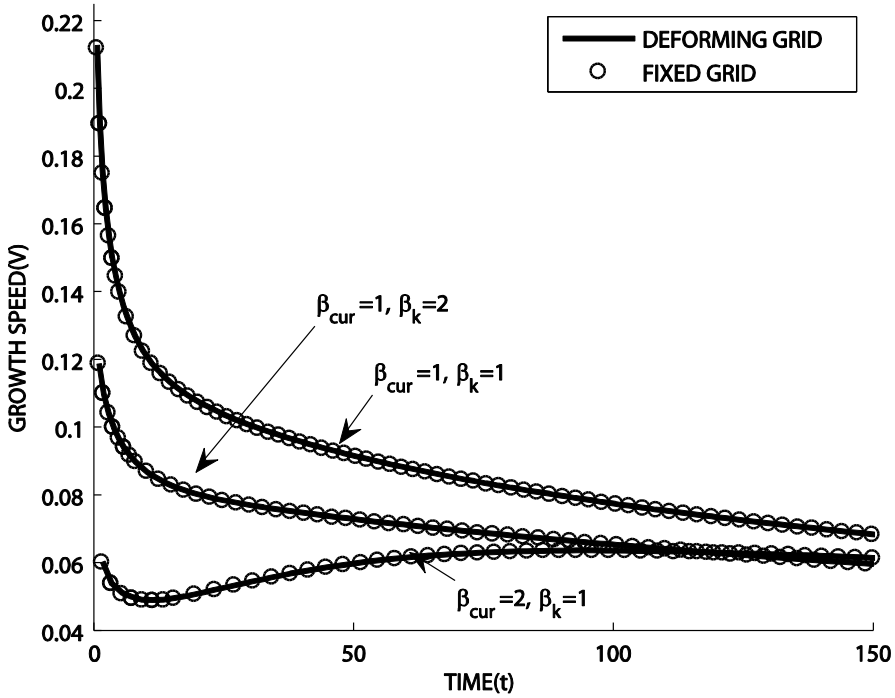

Figure 6-4. Fixed and deforming predictions for growth speed when both kinetic and curvature surface undercooling are in operation.

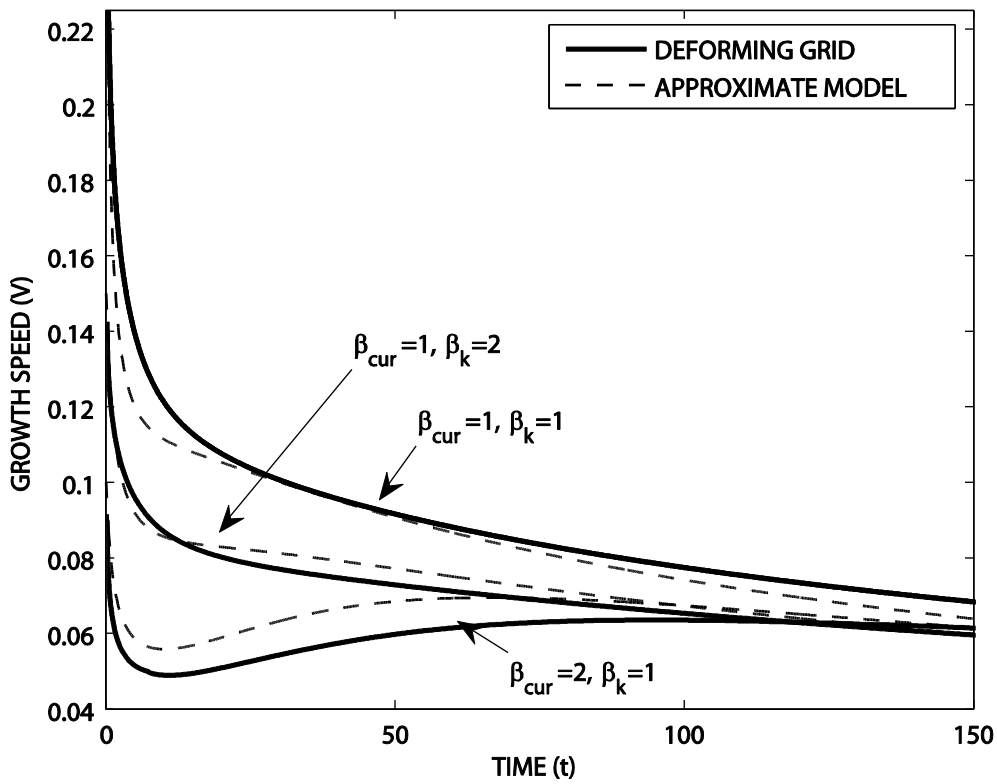

Figure 6-5. Comparison of approximate model (6.45) (with $\chi = 3$) and deforming grid prediction for growth speed, when both kinetic and curvature surface undercooling are in operation.

6.6. Conclusions

The problem of handling a moving boundary problem with a general surface undercooling is a numerically challenging problem and provides a reliable and worthwhile test for comparing fixed grid and deforming grid solution technologies. This work has developed two alternative techniques, a fixed grid enthalpy scheme and a deforming grid scheme, for dealing with the solidification of a solid seed in an undercooled melt. The novel aspect is the assumption of a sharp solid/liquid interface with the equilibrium solidification temperature set by both kinetic and surface energy undercooling. Across a wide range of applications predictions from both the fixed and deforming grid solutions are in close agreement.

The predictions obtained from the calculations shed light on understanding the role of the surface curvature and kinetic undercooling in controlling the solidification rate. In particular it is observed through the numerical results, and confirmed with a simple phenomenological model, that the main role of the kinetic undercooling is to reduce the growth speed whereas a large enough curvature undercooling has the additional ability to accelerate the seed growth.

The numerical techniques presented here also have an important role in the development and benchmarking of multi-dimensional methods for simulating dendritic growth in an undercooled melt (Beckermann et al. 1999, Kim et al. 2000, Udaykumar et al. 2003, Pal et al. 2006, Voller 2008, Fabbri & Voller 1995). A core difficulty in such calculations is grid anisotropy; the nature of the grid imposes a non-physical anisotropy on the predictions. The axisymmetric solutions developed here provide a comprehensive and general benchmark for assessing the impact of grid anisotropy of any given method. For example one can envision an attempt to solve the growth of the spherical seed on a Cartesian 3-D mesh. The rate of departure from the maintenance of a spherical seed would be a sound measure of the grid-anisotropy.

In closing it is worth considering the relative performance of the fixed and deforming grid methods. In terms of CPU requirements, due to the tight coupling and time implicit nature of the calculations, the deforming grid solution can operate more efficiently than the fixed grid solution. For example in obtaining the results for $\beta_{cur} = 1$ and $\beta_k = 1$ in Figure 6-4, $CPU_{deform} / CPU_{fix} \approx 0.1$.

The deforming grid solution also provides smooth predictions at every time step. In contrast, at times when the solid seed surface is not in the vicinity of a node, the fixed grid predictions can exhibit oscillations. As such, in the context of the two methods presented here, due to its efficiency and accuracy, the authors recommend using the deforming grid as a main analysis tool and reduce the easier to program fixed grid enthalpy scheme to the role of solution verification. In the general case, however, the deficiencies in the low-order enthalpy method could be overcome by using a higher order

fixed grid level set method (Kim et al. 2000, Sethian 1996). In such a case, due to its flexibility for dealing with complex front geometries this scheme would be preferable to a deforming grid scheme.

CHAPTER 7

CONCLUSTIONS AND FUTURE WORK

7.1. Conclusions

The goal of my PhD research was to develop Reduced-Complexity Models (RCMs) for the formation of river deltas at the scale of channel dynamics. In this collection of work we present the complete developing process towards a full delta formation model (Chapter 2, 3 and 4), as well as some of our earlier exploratory models (Chapter 5 and 6). The value of these models comes not only from the simulation results, but also from the journey of building them.

The main achievement in terms of modeling is the comprehensive delta building model in Chapter 4, which uses a framework of parcel-based weighted random walk. We use two chapters (Chapter 2 and 3) to describe how this weighted random walk framework starts from a simple and almost trivial cellular filling model to incorporating intuitive representations of fluid momentum balance to produce realistic plan-form meander rivers. In Chapter 4, the simple representations are further refined to connect to hydrodynamic equations and to deal with bed topography. In each step of improvement, we explain the reason for taking that step and what the model gains from that extra component. The final output in Chapter 4 includes realistic delta topography that compare to the output from higher-complexity models and a full range of channel dynamics. Although current focus is still on how many different behaviors the model can produce, we already see the potential of the model in answering real world questions such as why Wax Lake Delta has that distinct channel network pattern. The ability of the model to record stratigraphy makes it a handy tool for explaining outcrops as well as processes in laboratory basin experiments.

Some of our endeavors in the past six years didn’t grow into a full capacity delta building model as the one in Chapter 4, but we still see their values as potential ingredients for

new models and document them in details (Chapter 5 and 6). There are two things we would like to point out. First, despite the lack of physical connection in our analogical model between dendrite crystal growth and distributary channel network, we don't see this path as a dead-end; this is just a very preliminary attempt to cross over two systems with strikingly similar behaviors, and the method we use and the assumptions we make could be applied to other systems. Second, now looking back at the simple cellular routing model for mouth-bar formation, we realized there are some easy improvements that we can make according to some key ideas development in Chapter 3 and 4. This again proves that the value of our work is not only the output of the models but also the ideas, trials-and-errors during the process of developing them.

7.2. Future work

Following Chapter 4, we would like to improve the model by (i) adding more components (such as wave and tidal effects); (ii) coupling with ecological processes (such as vegetation growth); (3) validating and benchmarking current model component; (4) making comparisons between model stratigraphy and experimental stratigraphy.

For the validation work, I have already started collaborating with researchers at my post-doctoral institution (UT Austin) to test the hydrodynamic model in Chapter 4 and compare to Delft3D and field measurement at the Wax Lake Delta.

For the stratigraphy comparison, our first step is to test modeled delta responses to base-level change and subsidence against data from the Jurassic Tank experiments at Saint Anthony Falls Laboratory and the ones at UT Morphodynamics Lab.

We also hope to apply the same model framework to other environments, such as meandering rivers, which would be a direct extension of Chapter 3 with a similar construction of Chapter 4.

Last but not lease, it's important and to develop quantitative measurements for what RCMs rely on – the "behaviors" of a system. Currently a lot of comparisons are done

with an “eye-ball examination” that is only descriptive and qualitative. A set of metrics would be of great help to evaluate and improve RCMs.

7.3. The philosophy of reduced-complexity models

Now let’s have a look back about what are RCMs. All models by nature are reduced complexity, as it’s impossible to reproduce the exact details of any natural systems. But we still emphasize on the “reduced-complexity”, as opposed to the reductionist models, to advocate a very often under-estimated way of thinking, that how much can a system live without yet still keeps its basic behaviors and organizations?

RCMs offers a way of pure creation. Since they are based on behaviors, modelers don’t have to make every component accurate. We give two examples show this powerful flexibility. The first is from the work by Murray and Paola (1994), where they point out that the value of the exponent that relates sediment flux to water flux and slope does not affect the behaviors of the braided river model as long as its value is larger than one. The second is from the work by Ashton et al. (2001), where the long shore sediment flux is a function of the wave angle and the detailed shape of the curve doesn’t matter as long as in the range of 0 degrees to 180 degrees it first increases and then decreases. This means we can build more direct relations between processes in a system.

In the end, we quote an interesting writing, which fits very well in the topic of reduced-complexity.

On Exactitude in Science

Jorge Luis Borges, Collected Fictions, translated by Andrew Hurley.

… In that Empire, the Art of Cartography attained such Perfection that the map of a single Province occupied the entirety of a City, and the map of the Empire, the entirety of a Province. In time, those Unconscionable Maps no longer satisfied, and the Cartographers Guilds struck a Map of the Empire whose size was that of the Empire, and which coincided point for point with it. The following Generations, who were not so fond of the Study of Cartography as their forebears had been, saw that that vast Map was

Useless, and not without some Pitilessness was it, that they delivered it up to the Inclemencies of Sun and Winters. In the Deserts of the West, still today, there are Tattered Ruins of that Map, inhabited by Animals and Beggars; in all the Land there is no other Relic of the Disciplines of Geography.

--- *Suarez Miranda, Viajes de varones prudentes, Libro IV, Cap. XLV, Lerida, 1658*

REFERENCES

Ashton, A., Murray, A. B. and Arnault O. (2001) 'Formation of coastline features by large-scale instabilities induced by high-angle waves', *Nature*, vol. 414, pp. 296-300.

Bates, P. D., Horritt, M. S. and Fewtrell, T. J. (2010), 'A simple inertial formulation of the shallow water equations for efficient two-dimensional flood inundation modeling', *Journal of Hydrology*, vol. 387, pp. 33-45.

Beckermann, C., Diepers, H. J., Steinbach, I. , Karma, A. and Tong, X. (1999), 'Modeling Melt Convection in Phase-Field Simulations of Solidification', *J. Comp. Phys*, vol. 154, pp.468–496.

Carslaw, H. S. and Jaeger, J. C., (1959) *Conduction of Heat in Solids, 2nd ed*., Clarendon Press, Oxford.

Chatterjee, D. (2010) 'Lattice Boltzmann Simulations of Incompressible Phenomena in Macroscopic Solidification Processes', *Numer. Heat Transfer, Part B*, vol. 58, pp.55-72.

Coulthard, T. J., Macklini, M. G., Kirkby, M. J. (2002) 'A cellular model of Holocene upland river basin and alluvial fan evolution', *Earth Surf. Process. Landforms*, vol. 27, pp. 269-288.

Coulthard, T. J. and Van de Wiel, M. J. (2006) 'A cellular model of river meandering', *Earth Surf. Process. Landforms*, vol. 31, pp. 123-132.

Dantzig, J. and Rappaz, M. (2009) *Solidification*, EPFL press.

Dietrich, W. E. and Smith, J. D. (1983) 'Influence of the point bar on flow through curved channels', *Water Resources Research*, vol. 19 no. 5, pp. 1173-1192.

Edmonds, D. A., Slingerland, R. L. (2007) 'Mechanics of river mouth bar formation: implications for the morphodynamics of delta distributary networks'. *J. Geophys. Res.* 112:F02034

Edmonds, D.A., Slingerland R.L.. (2010) 'Significant effect of sediment cohesion on delta morphology'. *Nat. Geosci.*3:105–9

Fabbri, M. and Voller, V. R. (1995) 'Numerical-Solution of Plane-Front Solidification with Kinetic Undercooling', *Numer. Heat Transfer, Part B*, vol. 27, pp. 467-486.
Fagherazzi, S. and Overeem, I. (2007) 'Models of deltaic and inner continental shelf landform evolution', *Annual review of aerth and planetary sciences*, vol. 35, pp. 685-715.

Fang, H.S. , Bao, K. , Wei, J.A. , Zhang, H., Wu, E.H., and Zheng, L.L. (2009) 'Simulations of Droplet Spreading and Solidification using an Improved SPH Model', *Numer. Heat Transfer, Part A*, vol. 55, pp.124-143.

Falcini, F. and Jerolmack, D. J. (2010) 'A potential vorticity theory for the formation of elongate channels in river deltas and lakes', *J. Geophys. Res.*, 115, F04038, doi: 10.1029/2010JF001802.

Frazier, D. E. (1967) ‘Recent deltaic deposits of the Mississippi River: their development and chronology: Gulf Coast Association of Geological Societies Transactions’, v. 27, p. 287-315.

Geleynse N., Storms J. E. A., Stive M. J. F., Jagers H. R. A.,Walstra D. J. R. (2010) ‘Modeling of a mixed-load fluvio-deltaic system’, *Geophys. Res. Lett.* 37:L05402.

Gu¨neralp, I. and Rhoads, B. L. (2009) ‘Empirical analysis of the planform curvature-migration relation of meandering rivers’, *Water Resources Research*, vol. 45, W09424.

Hajek, E. A., Wolinsky, M. A. (2012) ‘Simplified process modeling of river avulsion and alluvial architecture: connecting models and field data’, *Sedimentary Geology*, vol. 1-30, pp. 257-260.

Heller, P. L., Paola, C., Hwang, I., John, B., Steel, R. (2001) ‘Geomorphology and sequence stratigraphy due to slow and rapid base-level changes in an experimental subsiding basin (XES 96-1)’, *AAPG Bulletin*, vol. 85 (5), pp. 817-838.

Howard, A. D. and Knutson, T. R. (1984) ‘Sufficient conditions for river meandering: a simulation approach’, *Water Resources Research*, vol. 20 (11), pp. 1659-1667.

Ikeda, S., Parker, G., Sawai, K. (1981) ‘Bend theory of river meanders. Part I. Linear development’, *J. Fluid Mech.*, vol. 112, pp. 363-377.

Jerolmack, D.J., and Paola, C. (2007), ‘Complexity in a cellular model of river avulsion’, *Geomorphology*, vol. 91, pp. 259-270.

Kim, W., Mohrig, D., Twilley, R., Paola, C., and Parker, G. (2009), ‘Is it feasible to build new land in the Mississippi River Delta?’: EOS, v. 90, no. 42, p. 373-374

Kim, Y-T , Goldenfeld, N., Dantzig, J. (2000) ‘Computation of Dendritic Microstructures Using a Level Set Method’, *Phys. Rev. E*, vol. 62, pp. 2471-2474.

Kurtz, W. and Fisher, D. J. (1986),*Fundamentals of Solidification*, Trans Tech, Switzerland.

Lal, A.M.W. (2008) ‘Development of a Robust Diffusion-Kinematic Flow Algorithm for Regional Hydrologic Models Operating with Large Time Steps’, *Proceedings of the World Environmental & Water Resources Congress 2008*, pp. 1-7.

Lal, A. M. W., Van Zee, R., Belnap, M. (2005) ‘Case Study: Model to Simulate Regional Flow in South Florida’, *Journal of Hydraulic Engineering*, vol. 131 no. 4, pp. 254-258.

Liang, M. and Voller V. R. (2011) ‘Fixed and Deforming Grid Solutions of Solidification in an Undercooled Melt: A Benchmark Problem’, *Numerical Heat Transfer, Part B: Fundamentals*, vol. 60:1, pp. 1-17.

Liu, J., Saito, Y., Kong, X., Wang, H., Xiang, L., Wen, C., Nakashima, R. (2010) ‘Sedimentary record of environmental evolution off the Yangtze River estuary, East China Sea, during the last ~13,000 years, with special reference to the influence of the Yellow River on the Yangtze River delta during the last 600 years’, *Quaternary Science Review*, vol. 29 (17-18), pp. 2424-2438.

Lorenzo-Trueba, J., Voller, V. R., Paola, C. (2013) ‘A geometric model for the dynamics of a fluvially dominated deltaic system under base-level change’, *Computers & Geosciences*, vol. 53, pp. 39-47,

Murray, A. B. and Paola, C. (1994) ‘A cellular model of braided rivers’, *Nature*, vol. 271, pp. 54-57.

Murray, A. B. (2003) ‘Contrasting the Goals, Strategies, and Predictions Associated with Simplified Numerical Models and Detailed Simulations, in Prediction in Geomorphology’ (eds P. R. Wilcock and R. M. Iverson), American Geophysical Union, Washington, D. C.. doi: 10.1029/135GM11

Nicholas, A. P. (2010) ‘Reduced-complexity modeling of free bar morphodynamics in alluvial channels’, *J. Geophys. Res.*, vol. 115, F04021,

Overeem, I., Syvitski, J. P. M., Hutton, E. W. H (2005), ‘Three-dimensional numerical modeling of deltas’, *River Deltas – Concepts, Models, and Examples, SEPM Special Publication*, No.83.

Pal, D., Bhattacharya, J., Dutta, P., Chakraborty, S. (2006) ‘An Enthalpy Model for Simulation of Dendritic Growth’, *Numer. Heat Transfer, Part B*, vol. 50, pp. 59-78.

Paola, C. (2000) 'Quantitative models of sedimentary basin filling', *Sedimentology*, vol. 47, pp. 121-178.

Paola, C and Leeder, M (2011) ‘Complexity and the memory of landscape’, *Nature*, 469 (7328). pp. 38-39.

Paola, C., Twilley, R.R., Edmonds, D.A., Kim, W., Mohrig, D., Parker, G., Viparelli, E. and Voller, V.R. (2011) 'Natural Processes in Delta Restoration: Application to the Mississippi Delta', in Carlson, C. and Giovannoni, S. (ed.) *Annual Review of Marine Science*, Annual Reviews.

Parker G and Andrews ED (1986) ‘On the time development of meander bends’, *Journal of Fluid Mechanics* 162: 139–156.

Parker, G., Muto, T., Akamatsu, Y., Dietrich, W.E. and Lauer, J.W. (2008) 'Unravelling the conundrum of river response to rising sea-level from laboratory to field. Part I: Laboratory experiments', *Sedimentology*, vol. 55, no. 6, pp. 1643-1655.

Parker, G., Shimizu, Y., Wilkerson, G. V., Eke, E. C., Abad, J. D., Lauer, J. W., Paola, C., Dietrich, W. E., Voller, V. R. (2011) ‘A new framework for modeling the migration of meandering rivers’, *Earth Surf. Process. Landforms*, vol. 36 (1), pp. 70-86.

Reitz, M. D., Jerolmack, D. J., Swenson, J. B. (2010) ‘Flooding and flow path selection on alluvial fans and deltas’, *Geophys. Res. Lett.* 37:L06401

Reitz, M. D. and Jerolmack, D. J. (2012) ‘Experimental alluvial fan evolution: channel dynamics, slope controls, and shoreline growth’, *J. Geophys. Res.*, vol. 117, F02021.

Rinaldo A., Fagherazzi, S., Lanzoni, S., Marani, M., Dietrich, W. E. (1999) ‘Tidal networks 2. Watershed delineation and comparative network morphology’, *Water Resour. Res.* 35(12):3905–17.

Schumm, S. A. (1967) ‘Meander wavelength of alluvial rivers’, *Science*, vol. 157, pp. 1549–1550.

Sethian, J. A. (1996) ‘A Fast Marching Level Set Method for Monotonically Advancing Fronts’, *PNAS*, vol. 93, pp. 1591-1595.

Seybold H., Andrade J. S., Herrmann H. J. (2007) ‘Modeling river delta formation’, *Proc. Natl. Acad. Sci. USA* 104:16804–9.

Seybold, H., Molnar, P., Singer, H. M., Andrade Jr, J. S., Herrmann, H. J., Kinzelbach, W. (2009) ‘Simulation of birdfoot delta formation with application to the Mississippi Delta’, *J. Geophys. Res.* 114:F03012.

Storms, J. E. A., Stive, M. J. F. et al. (2007) ‘Initial Morphologic and Stratigraphic Delta Evolution Related to Buoyant River Plumes’, *Proceedings of the Sixth International Symposium on Coastal Engineering and Science of Coastal Sediment Process, New Orleans, Louisiana, American Society of Civil Engineers*.

Sun, T., Paola, C., Parker, G., Meakin, P. (2002) ‘Fluvial Fan deltas: linking channel processes with large-scale morphodynamics’, *Water Resources Research*, vol. 38 (8), pp. 26-1-26-10.

Tarboton, D. G., (1997), ‘A new method for the determination of flow directions and contributing areas in grid digital elevation models’, *Water Resources Research*, vol. 33(2), pp. 309-319.

Day, J.W., Boesch, D.F., Clairain, E.J., Kemp, G.P., Laska, S.B., Mitsch, W.J., Orth, K., Mashriqui, H., Reed, D.J., Shabman, L., Simenstad, C.A., Streever, B.J., Twilley, R.R., Watson, C.C., Wells, J.T. and Whigham, D.F. (2007) 'Restoration of the Mississippi Delta: Lessons from Hurricanes Katrina and Rita', *Science*, vol. 315, no. 5819, pp. 1679-1684.

Udaykumar, H.S., Marella S., Krishnan S. (2003) ‘Sharp-Interface Simulation of Dendritic Growth with Convection: Benchmarks’, *Int. J. Heat Mass Transfer*, vol. 46, pp. 2615–2627.

Voller, V.R. and Cross M. (1981) ‘Accurate Solutions of Moving Boundary Problems Using the Enthalpy Method’, *Int. J. Heat Mass Transfer*, vol. 24, pp. 545-556.

Voller, V. R. (2004), ‘A Monte Carlo scheme for tracking filling fronts’, *Journal of Computational Physics*, vol. 200, pp. 399-411.

Voller, V. R. (2006) ‘A Similarity Solution for Solidification of an Under-Cooled Binary Alloy’, *Int. J. Heat and Mass Transfer*, vol. 49, pp. 1981-1985.

Voller, V. R. (2008a) ‘A Numerical Method for the Rubinstein Binary-alloy Problem in the Presence of an Under-Cooled Liquid’, *Int. J. Heat Mass Transfer*, vol. 51, pp. 696-706.

Voller V. R. (2008b) ‘An Enthalpy Method for Modeling Growth in a Binary Alloy’, *Int. J. Heat Mass Transfer*, vol. 51, pp. 823-834.

Voller, V. R. (2009) ‘Analytical Models of Solidification Phenomena’, *Int. J. Heat Mass Transfer*, vol. 62, pp. 279-283.

Werner, B. T. (1995), ‘Eolian dunes: computer simulations and attractor interpretation’, *Geology* 23, 1107–1110.

Wickert, A. D., J. M. Martin, M. Tal,W. Kim, B. Sheets, and C. Paola (2013) ‘River Channel Lateral Mobility:Metrics, Time Scales, and Controls’, *J. Geophys. Res. Earth Surf.*, vol. *118*, pp. 1-17.

Witten, T. A. Jr. and Sander, L. M. (1981) ‘Diffusion-limited aggregation, a kinetic critical phenomenon’, *Phys. Rev. Lett.*, vol. 47, pp. 1400-1403.

APPENDIX: ESTIMATING INTERFACE SPEED (for Chapter 6)

Using (6.17), the enthalpy formulation (6.18) can be written as

$$\frac{\partial T}{\partial t} - \frac{1}{r^2}\frac{\partial}{\partial r}\left(r^2 \frac{\partial T}{\partial r}\right) + \frac{\partial f}{\partial t} = 0, \quad f \in [0,1] \tag{A1}$$

On defining a "speed" function

$$V = \frac{\frac{\partial T}{\partial t} - \frac{1}{r^2}\frac{\partial}{\partial r}\left(r^2 \frac{\partial T}{\partial r}\right)}{|\nabla f|} = -\frac{\frac{\partial f}{\partial t}}{|\nabla f|} \tag{A2}$$

and a truncated "distance" function as

$$-0.5 \le \phi = f - 0.5 \le 0.5 \tag{A3}$$

equation (A1) can be written as

$$V|\nabla \phi| + \frac{\partial \phi}{\partial t} = 0 \tag{A4}$$

This equation matches the form of a level set equation Hence it is reasonable to classify the proposed enthalpy solution as a fast marching level set method with a truncated narrow band distance function $\phi \in [-.5,.5]$ (Sethian 1996). In this way, on recognizing that across the interface cell $|\nabla f| = 1/\Delta r$

The interface speed can be estimated as

$$V = \frac{-\frac{\partial f}{\partial t}}{|\nabla f|} \approx \frac{\Delta r}{\Delta t}(f_p^{old} - f_p) \tag{A5}$$